UNIVERSITY OF SOUTHAMPTON

FACULTY OF ENGINEERING, SCIENCE AND MATHEMATICS
School of Chemistry

Phase Cycling Methods and Spinning Sideband Manipulation in Solid-State NMR

by

Natala Ivchenko

The thesis is submitted for the degree
of Doctor of Philosophy

January 2005

UNIVERSITY OF SOUTHAMPTON
ABSTRACT
FACULTY OF ENGINEERING, SCIENCE AND MATHEMATICS
SCHOOL OF CHEMISTRY
Doctor of Philosophy
Phase Cycling Methods and Spinning Sideband Manipulation
in Solid-State NMR
by Natala Ivchenko

In solid-state nuclear magnetic resonance, phase cycling is used to compensate for experimental imperfections and to cancel out undesired signal components. This is achieved by adding together the signals from a number of single experiments, in which the experimental radiofrequency phases are varied and the NMR signals combined.

Magic angle spinning is a technique that averages out anisotropic interactions that cause line broadening. If the spinning frequency is not sufficiently high, spinning sidebands occur. They both complicate the spectrum and provide useful information. Methods exist for their suppression and separation, using pulse sequences of carefully-timed π-pulses.

In this thesis, multiplex phase cycling is proposed. In many cases, multiplex phase cycling allows selection of desired coherence pathways using a reduced number of signal acquisitions. By applying different phase factors to the signal in the processing stage, it is possible to obtain signals from different coherence pathways from the same data. The multiplex method is demonstrated experimentally in two-dimensional double-quantum NMR.

Cogwheel phase cycling is a new phase cycling strategy in which the phases of all the pulses are cycled simultaneously. An application of the cogwheel phase cycling to sideband suppression and sideband separation pulse sequences is demonstrated in the thesis. In the case of spin-1/2 nuclei, the cogwheel cycle provides a near seven-fold experimental time saving, while for quadrupolar nuclei, the time saving can be up to a factor of hundred.

The π-pulse duration is usually neglected when designing sequences for sideband suppression and separation. In this thesis, a method is described for taking into account the finite π-pulse duration. An improvement in pulse sequence performance is demonstrated experimentally.

A new pulse sequence for suppressing spinning sidebands in the magic-angle-spinning spectra of quadrupolar nuclei is also described.

"Scary-lookin' fing, inee?"
Stan Shunpike; on Sirius Black

J. K. Rowling, "Harry Potter
and the Prisoner of Azkaban"

Contents

0.1 Acknowledgements

Here, I would like to express my gratitude to all those people who helped and supported me during my Ph.D. years.

First of all, my thanks go to my supervisor Prof. Malcolm H. Levitt. Thank you dear Malcolm for the encouragement, trust, supervision and critisism (the latter one especially) I have received from you. A big thanks to you, Latha and Leela for welcoming me and my family into your home in Southampton for those few days when we didn't have anywhere to stay.

I am also very grateful to my adviser Prof. Geoffrey R. Luckhurst, for all the advice given to me on my quarterly reports and on other subjects.

I have had a great deal of support from people in Malcolm's group: Andreas and Jörn - for helping me in the beginning of my studies both with the NMR and computer; Colan - for so many things: helping me with English and the NMR, and teaching how to be less messy; Madhu - for great help with the NMR and for his course in solid-state NMR that I enjoyed; Ole - for help with computer-related issues, spectrometer and NMR in general; Marina - for teaching me Linux secrets; Jacco - for help with computer and spectrometer. Discussions with each and every person in the group have been very useful and educating for me on NMR - thank you!

I appreciate very much the help of all the people who proofread my thesis and gave me very useful responses: Prof. Malcolm H. Levitt, Dr. Colan .E. Hughes, Dr. Darren H. Brouwer, Dr. Marina Carravetta, Dr. Mattias Edén, Dr. Xin Zhao, Dr. Mykola Ivchenko. It must have been a big job, and was a great help. Also, I would like to thank Ildefonso Marin-Montesinos for help with binding the thesis.

Marina and Linda, it was very nice having you girls around me, to chat and to gossip with, have coffee with, and go shopping with - thanks for this, it was fun.

I am greatful to Mr. Colin Flowers for introducing me to teaching - I really miss this part of my Southampton University life.

Dear Jill and Nikki, you have made my (and, I'm sure, many other postgraduate students') stay and studies at the University of Southampton easier, helping me

0.2 Abbreviations

1D – One-Dimensional

2D – Two-Dimensional

ADC – Analog-to-Digital Converter

CP – Cross Polarization

CS – Chemical Shift

CSA – Chemical Shift Anisotropy

CTP – Coherence Transfer Pathway

CW – Continuous Wave

DREAM – Dipolar Recoupling Enhanced by Amplitude Modulation

DQ – Double Quantum

EM – Electromagnetic

FIREMAT – Five π Replicated Magic Angle Turning

FT – Fourier Transform

HORROR – Homonuclear Rotary Resonance

IRS – Isotropic Rotation Sequence

IRT – Irreducible Spherical Tensor

LS – Liquid State

MAS – Magic Angle Spinning

MRI – Magnetic Resonance Imaging

MQ – Multiple Quantum

NMR – Nuclear Magnetic Resonance

PAS – Principal Axes System

PASS – Phase-Altered Separation of Sidebands

PFG – Pulsed Field Gradient

$\mathbf{R}^2$ – Rotational Resonance

REDOR – Rotational Echo Double Resonance

RF – Radio-Frequency

RFDR – Radio-Frequency Driven Recoupling

QTOSS – Quadrupole TOSS

QPASS – Quadrupole PASS

SELTICS – Sideband Elimination by Temporary Interruption of the Chemical Shift

SHR – States-Habercorn-Ruben

SS – Solid State

TOSS – Total Suppression of Spinning Sidebands

TPPI – Time-Proportional Phase Incrementation

TPPM – Two Pulse Phase-Modulated

VIABLE – Variable-Low-Speed Sideband Suppression

WWII – World War II

XiX – X-inverse-X

Chapter 1

Introduction

1.1 Nuclear Magnetic Resonance

Nuclear Magnetic Resonance (NMR) is a phenomenon that is based on the property of some atomic nuclei in a magnetic field to absorb and emit electromagnetic radiation in the radio-frequency (RF) range. The absorption and emission is limited to narrow spectral lines, corresponding to the precession frequencies of the nuclei in the external magnetic field. Analysis of these lines is the subject of NMR spectroscopy, which provides information on the spatial configuration of the atoms and molecules.

In order for a nucleus to be NMR-active, it must possess a *spin*. Spin is a special kind of angular momentum; in contrast to a classical angular momentum that a macroscopic body possesses when in motion, spin is an intrinsic property of a particle that does not require motion. Most nuclear isotopes have spin and can therefore be used in NMR studies.

An important discovery was made by Max Planck in the very beginning of the XX century. He stated that the energy of an oscillator did not change continuously but rather in portions. The idea of discrete energy levels for an oscillator was later extended to a molecular level. The energy of vibrational and rotational molecular motion is also quantized. The transitions between discrete energy levels lead to absorption or emission of electromagnetic radiation of well defined frequency ν.

Various kinds of spectroscopy study different parts of the frequency spectrum, and thus different interactions (though there are no sharp boundaries between them):

- radiofrequency – $(3{\times}10^6\text{-}3{\times}10^{10})$ Hz. This region corresponds to the change in nuclear spin states in a magnetic field

- microwave – $(3{\times}10^{10}\text{-}3{\times}10^{12})$ Hz. This frequency range corresponds to rotational motion of molecules

- infra-red – $(3{\times}10^{12}\text{-}3{\times}10^{14})$ Hz. These frequencies correspond to the separation between the vibrational levels of molecules

- visible + ultra-violet (UV) – $(3{\times}10^{14}\text{-}3{\times}10^{16})$ Hz. This region corresponds to the separation of the energy states of the valence electrons

- X-ray – $(3{\times}10^{16}\text{-}3{\times}10^{18})$ Hz – corresponds to the energy separation of the electron levels in the inner electron shells

- γ-ray – $3{\times}10^{18}$ Hz and above. This frequency corresponds to the energy change due to intranuclear particle rearrangement

NMR spectroscopy uses the radio-frequency part of the spectrum. In fact, the frequency range determined the historical time point when NMR was discovered [1, 2]. World War II led to intensive development of radio-frequency generators and instruments, and after the war ended these techniques could be introduced into civilian and scientific use. In the mid-forties, two American groups: Edward Mills Purcell and his co-workers, from Harvard University, and Felix Bloch with co-workers from Stanford university performed experiments with nuclear magnetism and obtained the first NMR signal on protons: in solid paraffin and liquid water. The interest of both of these scientists in the NMR was stimulated by WWII, when both of them worked on radar developments, though Bloch had been working on the neutron magnetic moment since the mid-thirties.

For the first few decades after the discovery of NMR, the continuous wave (CW) method of data acquisition was used: the radiation was swept through a range of frequencies each of which was probed individually. Later on, Fourier Transform

NMR spectroscopy was introduced, which used short pulses of radiowaves to excite a broad range of transitions simultaneously, with their frequencies extracted from the signal by Fourier Transformation.

In 1952, F. Bloch and E. M. Purcell won the Nobel Prize in Physics "for their development of new methods for nuclear magnetic precision measurements and discoveries in connection therewith". Since then, there have been a number of scientists honoured with Nobel Prizes for their work connected with NMR: Richard R. Ernst (1991, "for his contributions to the development of the methodology of high resolution nuclear magnetic resonance (NMR) spectroscopy"), Kurt Wüthrich (2002, "for his development of nuclear magnetic resonance spectroscopy for determining the three-dimensional structure of biological macromolecules in solution"), Paul C. Lauterbur and Sir Peter Mansfield (2003, "for their discoveries concerning magnetic resonance imaging"), and many others in related disciplines [3]. Since the early 1950's, NMR spectrometers have become commercially available.

1.2   Solid-State NMR Spectroscopy

One of the major goals of NMR spectroscopy is the determination of the structure of matter, i.e. providing information on types of nuclei occuring in the sample, their separations and the environment created by surrounding molecular electrons. From this, molecular structures of single molecules and intermolecular arrangements can be derived.

There are two experimental techniques that can produce high-resolution structures of biological molecules, namely X-ray crystallography and NMR. In X-ray diffraction experiments, a monochromatic beam of a suitable wavelength is sent to either a single crystal (preferably) or a crystalline powder. The beam is scattered by the atomic electrons. The areas of high electron densities are arranged regularly in the crystal lattice. Similar to macroscopic diffraction, the scattered waves interfere with each other either cancelling each other or adding up. The diffraction pattern is analysed and the structure may be deduced. In the NMR spectroscopy, the sample (in any physical state) is placed in a strong static magnetic field and irradiated with

suitable frequencies. This causes transitions between the spin states of the atomic nuclei whose energies can be detected. The spectrum is then analysed. At present, the majority of protein structures in the Protein Database have been solved by X-ray crystallographers. However, as NMR hardware develops rapidly (in 2005, a 1 GHz magnet will be commercially available), the resolution of NMR spectra will improve, so that the number of NMR-solved structures is expected to increase.

As a tool for structure determination, NMR of liquid state samples is about 25 years younger than the X-ray method. Solid-state NMR is an even younger technique because many theoretical as well as experimental problems have only been solved during the last decade. Each of these three experimental techniques (X-ray crystallography, LS NMR and SS NMR) can often solve problems that the others cannot. For example, not all molecules form crystals big enough for the X-ray method to study, and the 3D structure of crystalline compounds may differ from the native structure. LS NMR has a much better spectral resolution than SS NMR. However, a huge amount of distance-dependent and orientation-dependent information is lost due to the molecular motion (although it can sometimes be reintroduced by adding liquid crystals, for example bicelles, into the system [4]). Still, most NMR experiments are performed in the liquid state. There are cases, for example with membrane proteins, semi-crystalline and amorphous materials, when SS NMR is the best (and only) choice [5].

1.3 Magic-Angle Spinning

Using NMR, it is possible to detect various kinds of internuclear interactions. Among these interactions, there are some that do not depend on the space orientation of molecules with respect to the external magnetic field, and others, that are orientation-dependent. The latter – anisotropic – interactions do not survive molecular motion that is present in a gas or liquid state, since their average over all orientations is zero. Because of this, in LS NMR the spectra show relatively well-resolved narrow lines. The important structural information contained in the anisotropic interactions is, however, lost.

In solid-state NMR, the situation is quite different. NMR samples, that usually are

in a powder form, consist of a huge number of crystallites. Each crystallite, with its own space orientation, will give a different spectral line. All these lines added together result in a broad pattern of low intensity. In order to deal with this problem, solid-state spectroscopists use a technique called "magic-angle spinning" (MAS) [6, 7]. A fine powder sample is placed in a cylindrical container (a rotor) that is spun about an axis tilted by the angle of 54.74° with respect to the magnetic field. As a result of this procedure, the spectral lines become narrow and liquid-like. However, if the spinning frequency at MAS is not large enough, spinning sidebands will arise. The frequencies of these lines differ from the isotropic frequency by an integer multiple of the spinning frequency. Together with the isotropic peak, they contain much structural information. On the other hand, having several peaks instead of one leads to a crowded spectrum. There are ways to suppress the spinning sidebands and to separate them by their order. Part of this thesis concerns the development of an improved method for this purpose.

In the periodic table, most isotopes have a spin, I. For some of them, $I = \frac{1}{2}$ and the nucleus has a spherical charge destribution. However, the absolute majority of nuclei are quadrupolar, i.e. their spin $I \geq 1$ so that their shape is not spherically-symmetrical. They are, for several reasons, generally more difficult to observe and manipulate. Nevertheless, interest in them is great because of their occurence in many industrial materials as well as in biological systems. For these nuclei, quadrupolar interaction exists that is anisotropic but has a different angular dependence from the other interactions. MAS does not average this interaction out completely, and even at a very high rotation frequency there is a line broadening due to this interaction. Part of this thesis describes an implementation of a method for the separation or suppression of the spinning sidebands of half-integer quadrupolar nuclei.

1.4 Phase Cycling

The NMR signal is a sum of several components. Often, only particular ones are of interest, but not the others. A procedure called "phase cycling" [8, 9] is used to filter out certain classes of NMR signal and suppress others. Phase cycling is

performed by repeating an NMR experiment a certain number of times changing the phase of the RF field that manipulates the spins, and adding the signals together.

1.5 Overview of the Thesis

In Chapters 2-5 of this thesis, an overview of modern NMR spectroscopy is given. In *Chapter 2*, the general principles of NMR spectroscopy are described, including the properties and behaviour of nuclear spins, the origin of the NMR signal, Fourier transformation and the NMR spectrum. The construction of a single-channel NMR spectrometer is described. In *Chapter 3*, some theoretical background is given. Wavefunctions and operators are introduced, as well as nuclear spin states. The construction of a density matrix is briefly described. Spin state populations, coherences, their orders and coherence pathways are introduced. *Chapter 4* is devoted to spin interactions. All the spin interactions of importance in solid-state NMR are described and the corresponding Hamiltonians are given. The coordinate frames and Euler angles that describe transformations between different reference frames are introduced. In *Chapter 5*, the experimental techniques, that are commonly used in solid-state NMR spectroscopy, are described, among them cross-polarization, magic-angle spinning, decoupling and recoupling techniques, and phase cycling methods. A program for computer simulation of the NMR experiments – SIMPSON [10] – is briefly described.

In *Chapter 6*, a new phase cycling procedure – multiplex phase cycling – is introduced. Experimental results are shown.

In *Chapter 7*, methods for spinning sideband manipulations are described. An improvment of TOSS and PASS sequences that are used for sideband suppression and separation is proposed and demonstrated experimentally.

In *Chapter 8*, a new QTOSS sequence for spinning sideband suppression in quadrupolar samples is described. It can be used at higher spinning frequencies than existing QTOSS sequences.

In *Chapter 9*, an application of the cogwheel phase cycling procedure to the TOSS and 2D PASS pulse sequences for spin-$\frac{1}{2}$ and quadrupolar nuclei, is demonstrated.

Chapter 10 contains a summary of results.

Chapter 2

General Principles of NMR

2.1   Nuclear Spin

Nuclear spin $\vec{I}$ is a special kind of angular momentum. Unlike classical angular momentum, it is not due to the rotational motion of the nucleus but is an intrinsic property.

Atomic nuclei are composed of protons and neutrons. Each of these nucleons consists of three elementary particles, called quarks, that have spin-$\frac{1}{2}$. An antiparallel spin configuration of three quarks leads to the proton and neutron having spin-$\frac{1}{2}$. In an atomic nucleus, the spins of protons and neutrons can be aligned in different ways. In some, the most energetically favored spin combination is when the total spin value is the minimal possible, but that is not always the case. The nuclei that are most commonly used in NMR (e.g. ^{13}C, ^{15}N, ^{1}H) all have spin-$\frac{1}{2}$. The majority of nuclei have spins $I > \frac{1}{2}$. Electrons also have spin-$\frac{1}{2}$. In diamagnetic materials, that are usually studied by NMR, there is, however, no net electronic magnetization. Therefore, electrons do not directly contribute to NMR signals. However, their presence around the nuclei strongly influences the NMR signals and is of great importance in NMR.

The magnetic moment of a nucleus $\vec{\mu}$ is proportional to the angular momentum, $\vec{I}$:

$$\vec{\mu} = \gamma_I \vec{I} \tag{2.1}$$

where the proportionality coefficient, γ_I, is the gyromagnetic ratio. Depending on the sign of γ_I, the spin angular momentum of the nucleus and its magnetic moment are either parallel or anti-parallel [11]. In the absence of any external fields, nuclear spins in the system have no preferred orientation. Consequently, the average polarization of the spin system is zero.

Application of an external field, $\vec{B}_0$, significantly influences the behaviour of the spins. First, they start precessing around the field vector with a frequency $\vec{\omega_0}$:

$$\vec{\omega_0} = -\gamma_I \vec{B}_0 \tag{2.2}$$

The precession frequency of a nucleus is called the *Larmor* frequency. In addition, in the presence of the field there is a dependence of the energy of the nucleus on the orientation of its magnetic moment:

$$E = -\vec{\mu} \cdot \vec{B}_0 \tag{2.3}$$

It is energetically favourable for the spins to have their magnetic moments oriented with field rather than against it; the average magnetization is no longer zero but is along $\vec{B}_0$ field (longitudinal magnetization). The partial alignment of the spins with the field makes NMR experiments possible.

2.2 The NMR spectrometer

A schematic picture of an NMR spectrometer is shown in Fig. 2.1. The most expensive part of an NMR spectrometer is the magnet (Fig. 2.1, 1). Today (December 2004), the most powerful commercially available superconducting magnet generates a field of 21.6 T, which corresponds to 920 MHz in ^{1}H precession frequency and is about 300,000 times larger than the Earth's magnetic field. In the magnet, there is a superconducting solenoid immersed in liquid helium which is surrounded in turn by liquid nitrogen. N_2 (with a boiling point of 77 K) is used as a relatively low-cost insulating layer protecting the more expensive He (that boils at 4 K).

The sample, either a liquid in an NMR tube or a solid – crystal or powder – in a rotor is placed into an NMR probe (Fig. 2.1, 2) that is inserted into the magnet. In order to make the magnetic field homogeneous, two sets of shimming coils are used: superconducting coils that are situated in the magnet itself and room-temperature ones that are positioned in the NMR probe. While the superconducting shimming is only made once when installing the magnet, the room-temperature shimming is ideally checked prior to every experimental session for each probe that is to be used.

In addition, each time a new probe or sample is inserted into the magnet, the probe should be tuned and matched. Good tuning means that, for all the observed nuclei, the resonant frequencies of the circuits coincide with the respective radio-frequencies. Good matching minimizes the RF power that is reflected by the probe.

The radiofrequency field is produced by an RF synthesizer (Fig. 2.1, 3). The frequency is set by the NMR machine user. From the RF synthesizer, the RF signal goes to the phase shifter unit (Fig. 2.1, 4), and thereafter in two directions: to the pulse gate (Fig. 2.1, 5) and to the receiver (Fig. 2.1, 11). The pulse gate is a switch that turns on and off to produce RF pulses of different duration (pulse width τ_p). The pulse programmer unit (Fig. 2.1, 6) controls both the phase shifter and the pulse gate, allowing one to obtain RF pulses of any duration and phase (within accuracy limits).

After the pulse gate, the RF signal reaches the RF amplifier (Fig. 2.1, 7) that increases the intensity of the RF pulses before sending them to the probe. From the amplifier, the RF signals comes to the duplexer (Fig. 2.1, 8), whose task is the following: to let the strong amplified RF pulses in to the probe (but not to the receiver) and to direct the small NMR signal coming from the probe to the sensitive signal receiver (Fig. 2.1, 11) via the signal amplifier (Fig. 2.1, 10).

When the RF signal comes to the probe (that is matched and tuned), electrical current in the RF coils (Fig. 2.1, 9) generates an oscillating field in the sample. After the RF pulse, the oscillating net magnetization of the spins in the sample, in turn, generates electric currents in the RF coil. A very weak NMR signal comes to the duplexer, is diverted to the signal amplifier (or preamplifier) that scales it up and then goes on to the quadrature receiver.

Figure 2.1: Schematic presentation of an NMR spectrometer with one channel. Adapted with permission from Ref. [11]

The quadrature receiver has two main tasks to perform. The first is to convert down the signal frequency. The frequency of NMR signals, ω_0, as well as the frequency of the RF pulses, ω_{RF}, is on the order of tens to hundreds of MHz. This is too fast for accurate conversion into digital form. Hence, the quadrature receiver combines the NMR signal with a reference signal of frequency ω_{RF} to generate a signal with relative frequency Ω_0:

$$\Omega_0 = \omega_0 - \omega_{RF} \tag{2.4}$$

The signal oscillating with the relative Larmor frequency can now be registered by the analog-to digital converter (Fig. 2.1, 12). The second problem that the quadrature receiver solves is the sign ambiguity in the relative frequency. The NMR signal is proportional to

$$s \propto \cos(\Omega_0 t) \tag{2.5}$$

Therefore it is not possible to distinguish between positive and negative frequencies. To get rid of the frequency sign ambiguity, an additional signal of the form

$$s \propto \sin(\Omega_0 t) \tag{2.6}$$

is needed. The quadrature receiver has two outputs: one for the down-converted NMR signal described above, and the other one for a down-converted NMR signal differing in phase by $\frac{\pi}{2}$:

$$s_1 \propto \cos(\Omega_0 t) \tag{2.7}$$

$$s_2 \propto \cos(\Omega_0 t - \frac{\pi}{2}) = \sin(\Omega_0 t) \tag{2.8}$$

These two signals are interpreted as the real and imaginary parts of a complex NMR signal and are combined to remove the sign ambiguity:

$$s_{complex} = s_1 + i s_2 \propto \exp(i \Omega_0 t) \tag{2.9}$$

If the radiofrequency reference signal is shifted in phase, this is transfered to the signal as follows:

$$s_{complex} \propto \exp(i\Omega_0 t)\exp(-i\varphi_{rec}) \tag{2.10}$$

After this, the two parts of the NMR signal reach the analog-to-digital converters (Fig. 2.1, 12). There they are converted into digital form. The dwell time is the time interval between two sampling points. The real and imaginary parts of the NMR signal, in digital form, then come to the post-digitizer phase-shifter unit (Fig. 2.1, 13) that shifts the phase of the signal by an additional factor of $\exp(-i\varphi_{dig})$. From here, the signal finally comes to the computer (Fig. 2.1, 14) to be saved, processed and analyzed by the spectrometer user.

On the Varian spectrometers, used for this thesis work, *Spinsight* software (version 4.3.2) was used for data acquisition and processing.

2.3 RF Pulse

During the NMR experiment, the spins experience a constant field $\vec{B}_0$. In addition, an RF field $\vec{B}_{RF}$ may be applied perpendicular to $\vec{B}_0$. The RF pulse is an oscillation of the RF field (Fig. 2.2, (a)) proportional to

$$B_{RF}\cos(\omega_{RF}t + \varphi) \qquad \text{during the RF pulse} \tag{2.11}$$
$$0 \qquad \text{otherwise}$$

where ω_{RF} is the frequency of the pulse and φ is the phase of the RF pulse. Usually, pulses are denoted by rectangles (Fig. 2.2, (b)) in diagrams representing the NMR experiment.

In order for the RF pulse to affect the spins, ω_{RF} (the frequency of the oscillating RF field) has to be resonant with the precessional motion of the spins. Short and strong RF pulses affect a relatively wide range of frequencies while long and weak ones are more frequency-selective. This field causes nutational motion of the spins with the frequency

$$\omega_{nut} = \mid \frac{1}{2}\gamma B_{RF} \mid \tag{2.12}$$

ω_{nut} is often used as a measure of "pulse strength", because it is proportional to $|\vec{B}_{RF}|$.

It is convenient to use a frame that rotates with the frequency of the RF pulse (rotating frame) so that the RF field appears to be static in this frame.

The pulse is characterized by a flip-angle β and a phase φ. The flip-angle is the
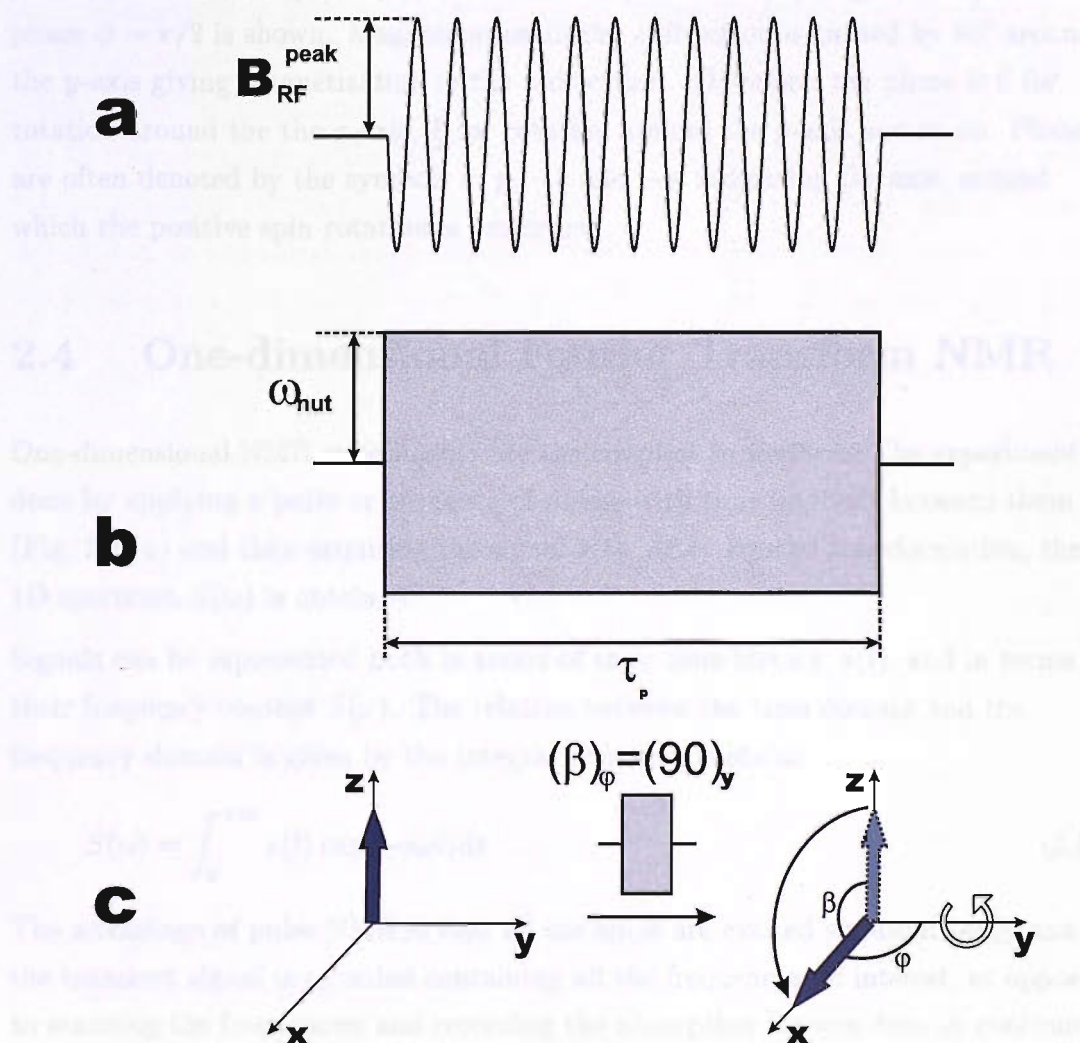
Figure 2.2: RF pulse. The oscillating RF field, *a*; schematic presentation of an RF pulse, *b*, and *c*, effect of an RF pulse β_y on a magnetization vector.

angle by which the spin polarization axis is rotated by the pulse and is given by

$$\beta = \omega_{nut}\tau_p \qquad (2.13)$$

where τ_p is the duration of the pulse. The phase indicates the angle between the x-axis and the axis around which the polarization is rotated, in the xy-plane of the rotating frame. In Fig. 2.2 (c), the effect of a pulse with flip-angle $\beta = \pi/2$ and phase $\varphi = \pi/2$ is shown. Magnetization in the z-direction is turned by 90° around the y-axis giving magnetization in the x-direction. Therefore, the phase is 0 for rotation around the the x-axis, $\frac{\pi}{2}$ for rotation around the y-axis and so on. Phases are often denoted by the symbols x, y, $-x$ and $-y$, indicating the axis, around which the positive spin rotation is performed.

2.4 One-dimensional Fourier Transform NMR

One-dimensional NMR experiments are the simplest to perform. The experiment is done by applying a pulse or sequence of pulses with time intervals between them (Fig. 2.3, a) and then acquiring the signal $s(t)$. After Fourier transformation, the 1D spectrum $S(\omega)$ is obtained.

Signals can be represented both in terms of their time history, $s(t)$, and in terms of their frequency content $S(\omega)$. The relation between the time domain and the frequency domain is given by the integral Fourier transform:

$$S(\omega) = \int_0^{+\infty} s(t)\exp\left(-i\omega t\right)\mathrm{d}t \qquad (2.14)$$

The advantage of pulse NMR is that all the spins are excited simultaneously and the transient signal is recorded containing all the frequencies of interest, as opposed to scanning the frequencies and recording the absorption (as was done in continuous wave NMR in the early days).

In practice the NMR signal is not a continuous function defined for all times, but is acquired over a limited time at finite sampling intervals. A discrete Fourier transform is therefore used in practice, instead of continuous Fourier transform (2.14).

2.5 Two-Dimensional NMR

Often, multidimensional (2D, 3D, 4D, etc) NMR experiments are performed in order to provide more information. They are used, for instance, for peak assignment in large molecules like proteins, for determination of line shapes in solid-state spectra, in particular for quadrupoles, for J and dipole-dipole coupling determination, *etc.* A 2D experiment is constructed by introducing an arrayed time interval t_1 into the 1D pulse sequence (Fig. 2.3, *b*). After the signal $s(t_1 = 0, t_2)$ is acquired a necessary number of times (for instance, in order reach a satisfactory signal-to-noise ratio), the t_1 interval is incremented by a chosen time Δt_1, and the experiment is repeated the same number of times and the signal $s(t_1 = \Delta t_1, t_2)$ is acquired again. These signals can be visualized as slices in a 2D space with different coordinates in t_1. A 2D FT is then applied to the data set in order to obtain a 2D spectrum (Fig. 2.3):

$$S(\omega_1, \omega_2) = \int_0^{+\infty} \int_0^{+\infty} s(t_1, t_2) \exp\left(-i\omega_1 t_1\right) \exp\left(-i\omega_2 t_2\right) \mathrm{d}t_1 \mathrm{d}t_2 \qquad (2.15)$$

In a similar manner, NMR experiments with higher dimensionality (3D, 4D, *etc*) are built by adding more incremented intervals into the pulse sequence. (One can also add another experimental dimension by arraying not the time interval but, for instance, the number of elements in a block of pulses, a pulse duration or a phase). After a multidimensional FT is applied to such a data set, a multidimensional spectrum is obtained. A 3D spectrum is represented as a cube or a surface in any two of three dimensions.

2.5.1 Pure Absorption NMR

A one-dimensional NMR quadrature-detected signal is a sum of many individual contributions and can be written as:

$$s(t) = \sum_{\ell=1}^{n} a_\ell \cdot \exp\left((i\Omega_\ell - \lambda_\ell)t\right) \qquad (2.16)$$

where n is the number of components, a_ℓ is the complex amplitude of the ℓth signal component that includes both its intensity $\mid a_\ell \mid$ and phase φ_ℓ:

$$a_\ell = \mid a_\ell \mid \exp(i\varphi_\ell) \qquad (2.17)$$

Ω_ℓ is the relative frequency, and λ_ℓ is the decay rate constant of this signal component. By performing a Fourier transform, a 1D spectrum can be obtained:

$$S(\Omega) = \int_0^\infty s(t)\exp(-i\Omega t)\mathrm{d}t = \sum_{\ell=1}^n a_\ell \cdot \mathcal{L}(\Omega;\Omega_\ell,\lambda_\ell) \qquad (2.18)$$

Here, $\mathcal{L}$ is a complex Lorentzian [11]:

$$\mathcal{L}(\Omega;\Omega_\ell,\lambda_\ell) = \mathcal{A}(\Omega;\Omega_\ell,\lambda_\ell) + i\mathcal{D}(\Omega;\Omega_\ell,\lambda_\ell). \qquad (2.19)$$

The real and imaginary parts of the complex Lorentzian, called absorption and dispersion Lorentzians, respectively, are given by the expressions:

$$\mathcal{A}(\Omega;\Omega_\ell,\lambda_\ell) = \frac{\lambda_\ell}{\lambda_\ell^2 + (\Omega - \Omega_\ell)^2} \qquad (2.20)$$

$$\mathcal{D}(\Omega;\Omega_\ell,\lambda_\ell) = -\frac{\Omega - \Omega_\ell}{\lambda_\ell^2 + (\Omega - \Omega_\ell)^2}$$

They give the absorption and dispersion line shapes (Fig. 2.4).
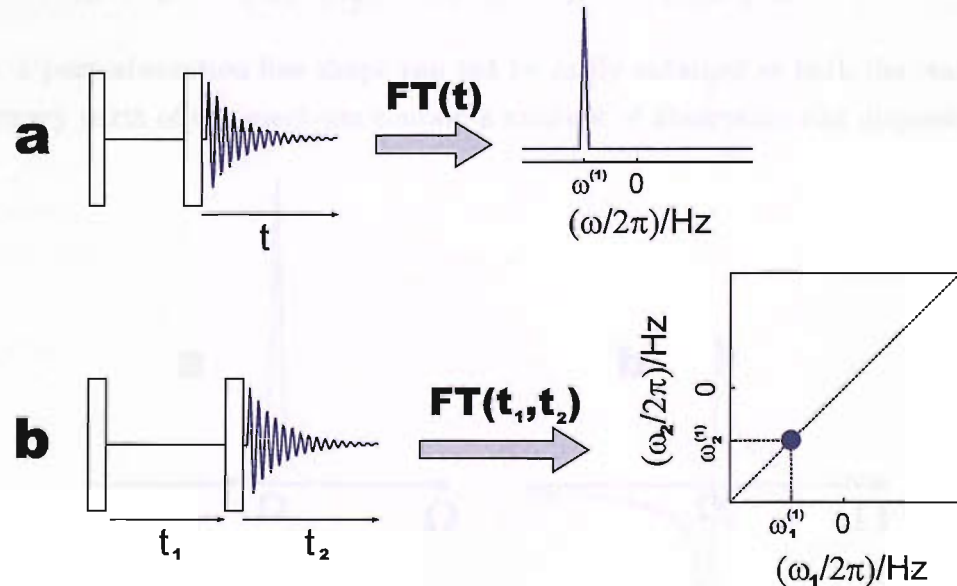
Figure 2.3: *a*, 1D and *b*, 2D NMR experiments and spectra.

Only the real part of the spectrum is usually displayed. Both parts contain equal amounts of frequency information, but the absorption part has a number of advantages compared to the dispersion part:

- it has a non-zero integral

- it is narrower, since its amplitude goes down as a function of $\frac{1}{(\Omega-\Omega_\ell)^2}$ while for the dispersion line shape the dependence is $\frac{1}{(\Omega-\Omega_\ell)}$

Therefore, in practice $Re(S(\Omega))$ is displayed on the monitor screen by default. A complex 2D signal is generally expressed as follows:

$$s(t_1,t_2) = \sum_\ell a_\ell \exp\left((i\Omega_\ell^{(1)} - \lambda_\ell^{(1)})t_1\right) \exp\left((i\Omega_\ell^{(2)} - \lambda_\ell^{(2)})t_2\right) \tag{2.21}$$

where the summation is over all the signal components. After complex 2D Fourier transformation, the signal $S(\Omega_1,\Omega_2)$ is obtained:

$$S(\Omega_1,\Omega_2) = (\mathcal{A}(\Omega_1) + i\mathcal{D}(\Omega_1))(\mathcal{A}(\Omega_2) + i\mathcal{D}(\Omega_2)) = \tag{2.22}$$
$$\mathcal{A}(\Omega_1)\mathcal{A}(\Omega_2) - \mathcal{D}(\Omega_1)\mathcal{D}(\Omega_2) + i\mathcal{A}(\Omega_1)\mathcal{D}(\Omega_2) + i\mathcal{D}(\Omega_1)\mathcal{A}(\Omega_2)$$

Here, a pure absorption line shape can not be easily obtained as both the real and imaginary parts of the spectrum contain a mixture of absorption and dispersion
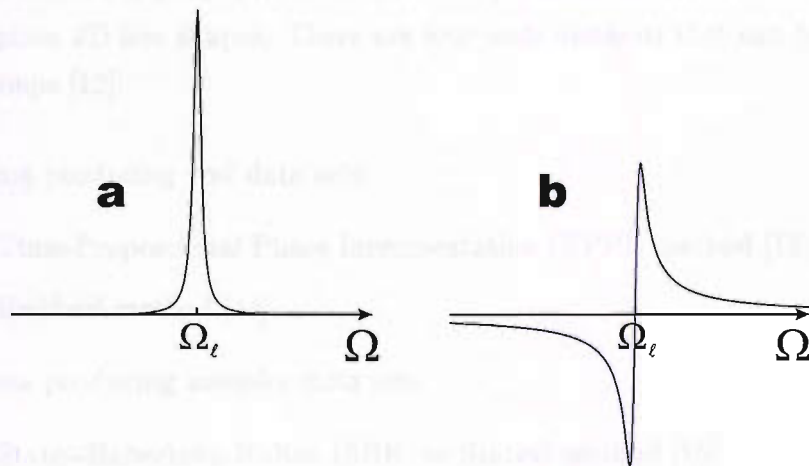
Figure 2.4: Absorption (a) and dispersion (b) Lorentzian line shapes.

Lorentzians. This results in so-called phase twist lineshapes, see Fig. 2.5. This line shape is highly undesirable, mainly because of its long dispersion tails [11].
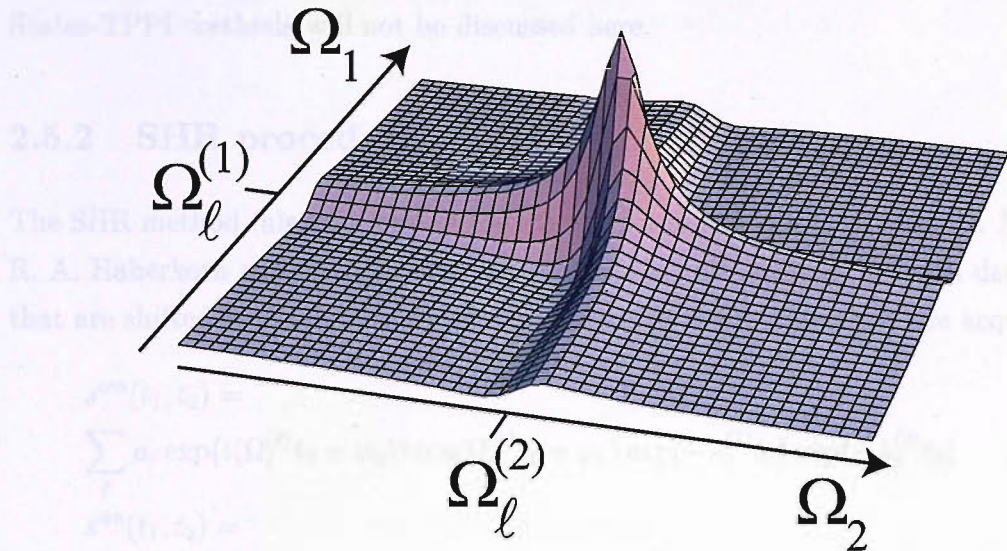
Figure 2.5: Example of a peak line shape with phase twists, with a mixture of absorption and dispersion mode one-dimensional Lorentzians. Figure is taken from [11], with permission.

A special procedure is needed in order solve the problem described above, i.e. to get pure absorption 2D line shapes. There are four such methods that can be combined into two groups [12]:

- schemes producing *real* data sets:

  - Time-Proportional Phase Incrementation (TPPI) method [13]
  - Redfield method [14]

- schemes producing *complex* data sets:

  - States-Haberkorn-Ruben (SHR, or States) method [15]
  - States-TPPI method [16]

Although the resulting NMR spectra that are produced by using any of these methods are equal in quality and required acquisition time, the TPPI and SHR methods are generally more popular then the other two. Therefore the Redfield and States-TPPI methods will not be discussed here.

2.5.2 SHR procedure

The SHR method (also referred as the States method) was proposed by D. J. States, R. A. Haberkorn and D. J. Ruben in 1982 [15]. In this method, two real data sets that are shifted by $\frac{\pi}{2}$ with respect to each other in the t_1 dimension are acquired:

$$s^{\cos}(t_1, t_2) = \tag{2.23}$$
$$\sum_{\ell} a_{\ell} \exp(i(\Omega_{\ell}^{(2)} t_2 + \varphi_2)) \cos(\Omega_{\ell}^{(1)} t_1 + \varphi_1) \exp(-\lambda_{\ell}^{(1)} t_1) \exp(-\lambda_{\ell}^{(2)} t_2)$$

$$s^{\sin}(t_1, t_2) = \tag{2.24}$$
$$\sum_{\ell} a_{\ell} \exp(i(\Omega_{\ell}^{(2)} t_2 + \varphi_2)) \cos(\Omega_{\ell}^{(1)} t_1 + \varphi_1 - \frac{\pi}{2}) \exp(-\lambda_{\ell}^{(1)} t_1) \exp(-\lambda_{\ell}^{(2)} t_2) =$$
$$\sum_{\ell} a_{\ell} \exp(i(\Omega_{\ell}^{(2)} t_2 + \varphi_2)) \sin(\Omega_{\ell}^{(1)} t_1 + \varphi_1) \exp(-\lambda_{\ell}^{(1)} t_1) \exp(-\lambda_{\ell}^{(2)} t_2)$$

In the direct dimension t_2, the problem of frequency discrimination is taken care of by quadrature detection. The signal processing is accomplished according to the following scheme:

1. 1D Fourier transformation of both the amplitude-modulated signals with respect to the t_2 dimension:

$$S^{\cos}(t_1, \Omega_2) = \int_0^{\infty} s^{\cos}(t_1, t_2) dt_2 \exp(-i\Omega_2 t_2) = \tag{2.25}$$
$$\sum_{\ell} a_{\ell} \exp(-\lambda_{\ell}^{(1)} t_1) \cos(\Omega_{\ell}^{(1)} t_1 + \varphi_1) \mathcal{L}(\Omega_2; \Omega_{\ell}^{(2)}, \lambda_{\ell}^{(2)})$$

$$S^{\sin}(t_1, \Omega_2) = \int_0^{\infty} s^{\sin}(t_1, t_2) dt_2 \exp(-i\Omega_2 t_2) = \tag{2.26}$$
$$\sum_{\ell} a_{\ell} \exp(-\lambda_{\ell}^{(1)} t_1) \sin(\Omega_{\ell}^{(1)} t_1 + \varphi_1) \mathcal{L}(\Omega_2; \Omega_{\ell}^{(2)}, \lambda_{\ell}^{(2)})$$

where $\mathcal{L}(\Omega_2; \Omega_{\ell}^{(2)}, \lambda_{\ell}^{(2)})$ is the complex Lorentzian.

2. The real part of the two signals is taken. In both cases, it contains only the absorption part of the Lorentzian:

$$Re(S^{\cos}(t_1, \Omega_2)) = \sum_\ell a_\ell \exp(-\lambda_\ell^{(1)} t_1) \cos(\Omega_\ell^{(1)} t_1 + \varphi_1) \mathcal{A}(\Omega_2; \Omega_\ell^{(2)}, \lambda_\ell^{(2)})$$

$$Re(S^{\sin}(t_1, \Omega_2)) = \sum_\ell a_\ell \exp(-\lambda_\ell^{(1)} t_1) \sin(\Omega_\ell^{(1)} t_1 + \varphi_1) \mathcal{A}(\Omega_2; \Omega_\ell^{(2)}, \lambda_\ell^{(2)})$$

3. The two data sets $Re(S^{\cos}(t_1, \Omega_2))$ and $Re(S^{\sin}(t_1, \Omega_2))$ are combined together into a hybrid complex signal:

$$S^{SHR}(t_1, \Omega_2) = Re(S^{\cos}(t_1, \Omega_2)) + iRe(S^{\sin}(t_1, \Omega_2)) = \qquad (2.27)$$

$$\sum_\ell a_\ell \exp(-\lambda_\ell^{(1)} t_1) \exp(i(\Omega_\ell^{(1)} t_1 + \varphi_1)) \mathcal{A}(\Omega_2; \Omega_\ell^{(2)}, \lambda_\ell^{(2)})$$

4. Finally, a 1D Fourier transform with respect to t_1 is taken:

$$S^{SHR}(\Omega_1, \Omega_2) = \int_0^\infty S^{SHR}(t_1, \Omega_2) dt_1 \exp(-i\Omega_1 t_1) = \qquad (2.28)$$

$$\mathcal{L}(\Omega_1; \Omega_\ell^{(1)}, \lambda_\ell^{(1)}) \mathcal{A}(\Omega_2; \Omega_\ell^{(2)}, \lambda_\ell^{(2)})$$

5. The real part of $S^{SHR}(\Omega_1, \Omega_2)$ is a pure-absorption 2D spectrum with frequency sign discrimination:

$$Re(S^{SHR}(\Omega_1, \Omega_2)) = \mathcal{A}(\Omega_1; \Omega_\ell^{(1)}, \lambda_\ell^{(1)}) \mathcal{A}(\Omega_2; \Omega_\ell^{(2)}, \lambda_\ell^{(2)}) \qquad (2.29)$$

The phase shift of the two signals is achieved by applying a different phase to the excitation block before t_1 (in the case of a double-quantum experiment the additional phase factor is $\frac{\pi}{4}$).

Graphically, this method can be illustrated in the following way (see Fig. 2.6, *c*). Sine and cosine functions $\cos(\Omega^{(1)} t_1)$ and $\sin(\Omega^{(1)} t_1)$, being, respectively, symmetric and antisymmetric with respect to the $t_2 = 0$ axis, result in two symmetrical peaks, with amplitude having either the same sign (for cos-modulated signal) or opposite signs (for the sin-modulated signal) for the two peaks. The result of their summation is a spectrum with frequency discrimination.

2.5.3   TPPI Method

In the TPPI method [13], the phase of the preparation pulse (or block of pulses), in addition to the pulse phase that is required by the phase cycle, experiences a phase
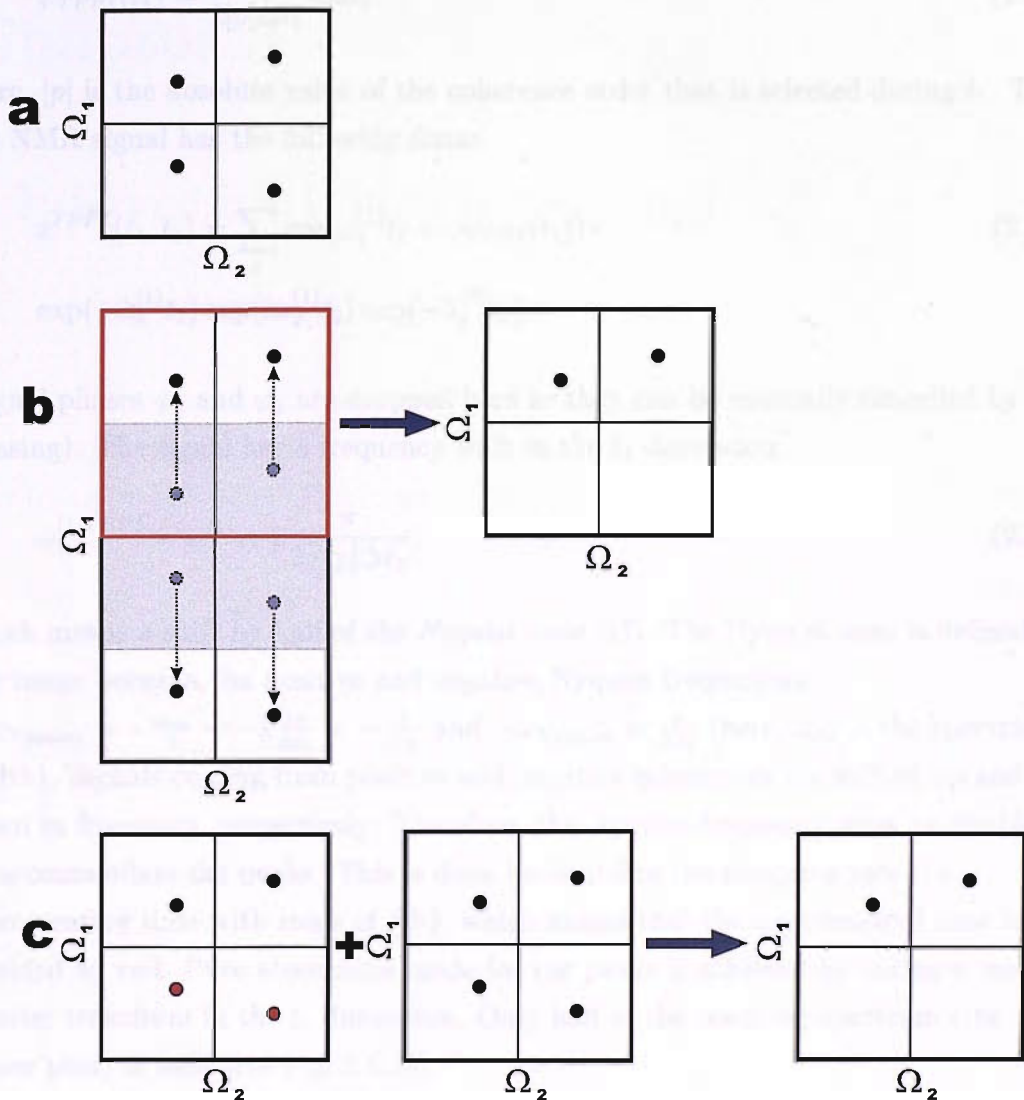

Figure 2.6: Graphical illustration of introduction of the frequency sign discrimination by the SHR and TPPI methods. A hypothetical 2D spectrum with no frequency discrimination is shown in (a). (b) and (c) illustrate the ideas behind the TPPI and SHR methods, respectively.

shift that is proportional to $n\Delta t_1$, where Δt_1 is the time step in the t_1 dimension and n is the number of completed increments. The additional phase, φ_{TPPI}, is calculated as:

$$\varphi_{TPPI}(t_1) = \frac{\pi}{2|p|\Delta t_1} n\Delta t_1 \tag{2.30}$$

Here, $|p|$ is the absolute value of the coherence order that is selected during t_1. The 2D NMR signal has the following form:

$$s^{TPPI}(t_1, t_2) = \sum_{\ell} \cos(\omega_1^{(1)} t_1 + \varphi_{TPPI}(t_1)) \times \tag{2.31}$$
$$\exp(-\lambda_\ell^{(1)} t_1) \exp(i\omega_2^{(1)} t_2) \exp(-\lambda_\ell^{(2)} t_2)$$

(signal phases φ_1 and φ_2 are dropped here as they can be manually cancelled by phasing). The signal has a frequency shift in the t_1 dimension:

$$\omega_1^{(1)TPPI} = \omega^{(1)} + p\frac{\pi}{2 \cdot |p|\Delta t_1} \tag{2.32}$$

which means a shift by half of the *Nyquist zone* [17]. The Nyquist zone is defined as the range between the positive and negative Nyquist frequencies $-\omega_{Nyquist} = -\frac{\omega_{sw}}{2} = -\frac{1}{2}\frac{2\pi}{\Delta t_1} = -\frac{\pi}{\Delta t_1}$ and $+\omega_{Nyquist} = \frac{\pi}{\Delta t_1}$ (here, ω_{sw} is the spectral width). Signals coming from positive and negative coherences are shifted up and down in frequency, respectively. Therefore, the Nyquist frequency must be doubled to accommodate the peaks. This is done by doubling the sampling rate (i.e. incrementing time with steps of $\frac{\Delta t_1}{2}$), which means that the experimental time is doubled as well. Pure absorption mode for the peaks is achieved by taking a real Fourier transform in the t_1 dimension. Only half of the resulting spectrum (the upper part) is used (see Fig. 2.6,*b*)).

Chapter 3

Theoretical Background

3.1 Wavefunctions and Operators

The quantum state of a system can be described by a wavefunction $\mid \psi_{full} >$. It is time dependent and contains all the information on the electrons and nuclei in the system (their coordinates, velocities, spin states, *etc*). In NMR, however, only the nuclear spin part of it is considered: $\mid \psi_{spin} >$.

An operator $\widehat{\mathcal{A}}$ is a general rule for producing a function g from a given function f. If the functions can be expanded on a full basis of N functions, operators are in general represented by a matrix of dimension of $N \times N$. If $g \propto f$, i.e. if

$$\widehat{\mathcal{A}} \mid f >= a \mid f > \tag{3.1}$$

then the function $\mid f >$ is an *eigenfunction* of the operator $\widehat{\mathcal{A}}$ with *eigenvalue a*. Two operators $\widehat{\mathcal{A}}$ and $\widehat{\mathcal{B}}$ are said to commute if

$$[\widehat{\mathcal{A}}, \widehat{\mathcal{B}}] = \widehat{\mathcal{A}}\widehat{\mathcal{B}} - \widehat{\mathcal{B}}\widehat{\mathcal{A}} = 0 \tag{3.2}$$

3.2 Spin States

In quantum mechanics the angular momentum operator is defined as

$$\widehat{\vec{L}} = -i\frac{1}{\hbar}(\vec{r} \times \widehat{\vec{\nabla}}). \tag{3.3}$$

and the operator of the square of the angular momentum is

$$\widehat{L^2} = \widehat{L_x}^2 + \widehat{L_y}^2 + \widehat{L_z}^2. \tag{3.4}$$

It can be shown that $\widehat{L^2}$ commutes with all the components $\widehat{L_x}$, $\widehat{L_y}$ and $\widehat{L_z}$, while the components do not commute between themselves:

$$[\widehat{L_x}, \widehat{L_y}] = i\hbar \widehat{L_z}. \tag{3.5}$$

This means that a common system of eigenfunctions can be chosen for the operator $\widehat{L^2}$ and any of the component operators, usually $\widehat{L_z}$ with z chosen along the external magnetic field. The system of eigenfunctions can be described with two eigenvalues, l and m, the orbital quantum number and the azimuthal quantum number, respectively:

$$\widehat{L_z}|lm> = \hbar m |lm> \tag{3.6}$$

and

$$\widehat{L^2}|lm> = \hbar l(l+1)|lm> . \tag{3.7}$$

Here $|lm>$ denotes the corresponding eigenfunction of both operators. The orbital quantum number l can take non-negative integral values: 0, 1, ..., and the azimuthal quantum number takes values between $-l$ and l with a spacing of 1. This means that the angular momentum is quantised, taking on a discrete set of values l and m.

From now on the unit $\hbar$ will be dropped, for simplicity.

For an isolated nucleus with spin I, there are $2I+1$ values for the azimuthal quantum number m, i.e. possible spin states: $m = -I, (-I+1), \ldots, +I$. For a single spin-$\frac{1}{2}$, there are only 2 possible values, $\pm\frac{1}{2}$:

$$\widehat{I_z}|\alpha> = +\frac{1}{2}|\alpha>$$
$$\widehat{I_z}|\beta> = -\frac{1}{2}|\beta> \tag{3.8}$$

where $\alpha = |\frac{1}{2}; +\frac{1}{2} >$ and $\beta = |\frac{1}{2}; -\frac{1}{2} >$. The states α and β are called the Zeeman eigenstates of the particle. The functions $| \alpha >$ and $| \beta >$ are the eigenstates of the operator $\widehat{I_z}$ (projection of I on the direction of the magnetic field), and eigenstates of the Zeeman Hamiltonian with determined energies (Fig. 3.1).

However, a spin is not restricted to these two states, it can be in any state that is a superposition of $| \alpha >$ and $| \beta >$:

$$| \psi >= c_\alpha | \alpha > + c_\beta | \beta > \tag{3.9}$$

where c_α and c_β are the superposition coefficients (complex numbers) that give the relative contributions of the Zeeman eigenstates $|\alpha >$ and $|\beta >$ to the function $|\psi >$. They must satisfy the normalization condition:

$$| c_\alpha |^2 + | c_\beta |^2 = 1 \tag{3.10}$$

The number of Zeeman energy levels depends on ℓ and is equal $2\ell + 1$. For a spin-$\frac{3}{2}$, there are four states: $| \frac{3}{2}; +\frac{3}{2} >$, $| \frac{3}{2}; +\frac{1}{2} >$, $| \frac{3}{2}; -\frac{1}{2} >$ and $| \frac{3}{2}; -\frac{3}{2} >$ (the corresponding energy diagram is shown in Fig. 3.2).

3.3   Density Matrix

A real sample consists of a large number of spins. Each of them is in a superposition state, with its own c_α and c_β, so that it is nearly impossible to
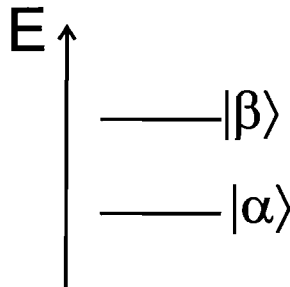
Figure 3.1: Energy level diagram for a spin-$\frac{1}{2}$ nucleus in a magnetic field, with positive γ.

describe the system in terms of the individual spin states. It is possible, however, to describe it using the *density matrix* method that describes the quantum state of the spin ensemble as a whole.

In quantum mechanics, an average result of many observations on an operator $\widehat{Q}$ – the expectation value – for a spin state $\mid \psi >$ is defined as:

$$< \widehat{Q} >=< \psi \mid \widehat{Q} \mid \psi >$$ (3.11)

It can be shown that this is equivalent to

$$< \widehat{Q} >= Tr\{\mid \psi >< \psi \mid \widehat{Q}\}$$ (3.12)

For a system of N spins that are in states $\mid\psi_1 >, \mid\psi_2 >, \ldots, \mid\psi_N >$, expression (3.11) transforms into:

$$< \widehat{Q} >=< \psi_1 \mid \widehat{Q} \mid \psi_1 > + < \psi_2 \mid \widehat{Q} \mid \psi_2 > + \ldots + < \psi_N \mid \widehat{Q} \mid \psi_N >$$
$$= Tr\{(\mid\psi_1 >< \psi_1\mid + \mid\psi_2 >< \psi_2\mid + \ldots + \mid\psi_N >< \psi_N\mid)\widehat{Q}\}$$ (3.13)

This expression may be rewritten as follows:

$$< \widehat{Q} >= Tr\{\widehat{\rho}\,\widehat{Q}\}$$ (3.14)
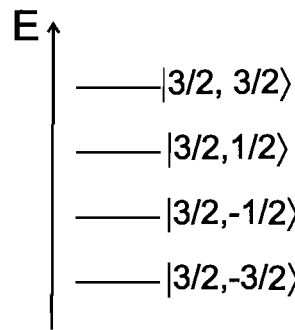
Figure 3.2: Energy level diagram for a spin-$\frac{3}{2}$ nucleus in a magnetic field, with negative γ.

where the density operator $\widehat{\rho}$ is defined as

$$\widehat{\rho} = \overline{|\,\psi><\psi\,|} \tag{3.15}$$

Here, the average is taken over the whole spin ensemble.

3.4 Populations and Coherences

For a system of non-interacting spins-$\frac{1}{2}$, the density matrix (matrix representation of the density operator) is written as

$$\widehat{\rho} = \begin{pmatrix} \rho_{\alpha\alpha} & \rho_{\alpha\beta} \\ \rho_{\beta\alpha} & \rho_{\beta\beta} \end{pmatrix} = \begin{pmatrix} \overline{c_\alpha c_\alpha^*} & \overline{c_\alpha c_\beta^*} \\ \overline{c_\beta c_\alpha^*} & \overline{c_\beta c_\beta^*} \end{pmatrix} \tag{3.16}$$

The diagonal components of the $\widehat{\rho}$ matrix, denoted as $\rho_{\alpha\alpha}$ and $\rho_{\beta\beta}$, are called the "populations" of the state α and β, respectively (Fig. 3.3).
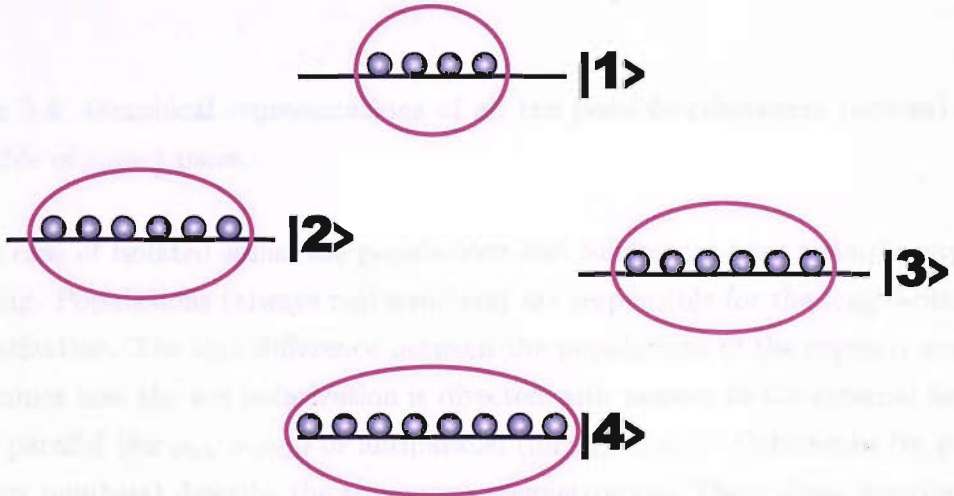
Figure 3.3: Graphical representations of all the four possible populations in a system of two spins-$\frac{1}{2}$.

The off-diagonal elements, denoted as $\rho_{\alpha\beta}$ and $\rho_{\beta\alpha}$, are the "coherences" between the states α and β. Coherences between the two states, in general $|\,r>$ and $|\,s>$,

are classified by their orders. The coherence order is defined as difference between their projections of angular momenta $M_r - M_s$. In the case of one spin-$\frac{1}{2}$, the coherence $\rho_{\alpha\beta}$ has an order of

$$p_{\alpha\beta} = +\frac{1}{2} - \left(-\frac{1}{2}\right) = 1 \qquad (3.17)$$

In a spin-state diagram (see Fig. 3.4), coherences between states are shown as arrows from one state to the other.
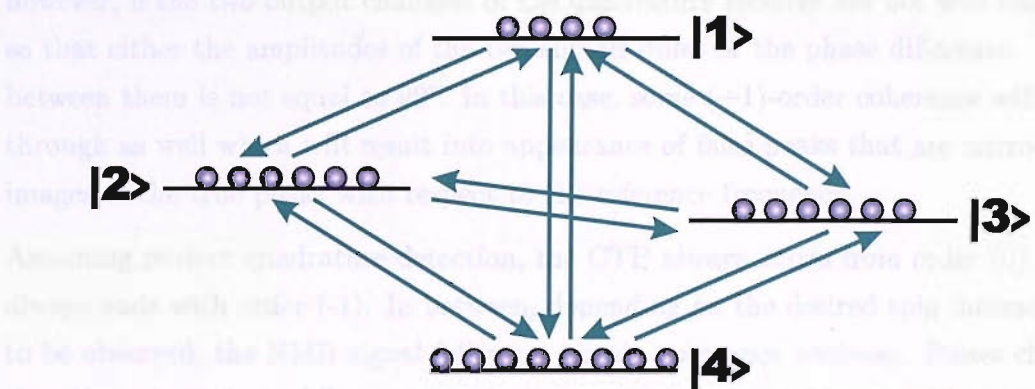
Figure 3.4: Graphical representations of all the possible coherences (arrows) in an ensemble of spin-$\frac{1}{2}$ pairs.

In the case of isolated spins, the populations and coherences have a simple physical meaning. Populations (always real numbers) are responsible for the longitudinal magnetization. The sign difference between the populations of the states α and β determines how the net polarization is directed with respect to the external field: either parallel (for $\rho_{\alpha\alpha} > \rho_{\beta\beta}$) or antiparallel (for $\rho_{\alpha\alpha} < \rho_{\beta\beta}$). Coherences (in general complex numbers) describe the transverse magnetization. Their phase describes the direction of the magnetization in the same manner as the pulse phase describes the magnetisation rotation axis, i.e. starting from the $+x$-axis, and their amplitude describes the amount of the coherence.

3.5 Coherence Transfer Pathways

Each NMR experiment can be characterized by a coherence transfer pathway (CTP). A CTP is defined as the history of coherence orders during the experiment, leading to the observable signal. Before the NMR experiment starts, the spin system is in a state of thermal equilibrium, with the net magnetization along the magnetic field. The corresponding coherence order is (0). It is possible to show [11] that the quadrature receiver only detects the (-1)-coherence order. This is not true, however, if the two output channels of the quadrature receiver are not well balanced so that either the amplitudes of the two signals differ or the phase difference between them is not equal to 90°. In this case, some (+1)-order coherence will go through as well which will result into appearance of false peaks that are mirror images of the true peaks with respect to the reference frequency.

Assuming perfect quadrature detection, the CTP always starts from order (0), and always ends with order (-1). In between, depending on the desired spin interaction to be observed, the NMR signal follows a certain coherence pathway. Pulses change the coherence order, while between the pulses the existing coherence orders are fixed. The history of the coherence order changes during the NMR experiment is called a total coherence pathway. For clarity, coherence transfer pathways are usually shown as bold lines in a coherence pathway diagram. In Fig. 3.5, an example of a coherence transfer diagram for an NMR experiment, that will be discussed later in this thesis, is shown.

Figure 3.5: Coherence pathway for the TOSS pulse sequence (that is discussed later in this thesis) consisting of a $\frac{\pi}{2}$-pulse followed by five π-pulses.

Chapter 4

Spin Interactions

4.1   Spin Hamiltonian

The Hamiltonian is a particularly important concept in NMR. It is the energy
operator and allows the calculation of the transition energy between different spin
states, giving an understanding of the NMR spectrum.

The state function $\mid \psi(t) >$ that describes the state of a spin system and the
Hamiltonian operator $\widehat{H}$ are connected by the equation

$$\frac{\mathrm{d}}{\mathrm{d}t}\psi(t) = -i\widehat{H}\psi(t) \tag{4.1}$$

which is called the time-dependent Schrödinger equation. For a spin ensemble
whose state is described by a density matrix $\widehat{\rho}$, equation (4.1) transforms into the
more general von Neumann equation [18]:

$$\frac{\mathrm{d}}{\mathrm{d}t}\widehat{\rho}(t) = -i[\widehat{H}, \widehat{\rho}(t)] \tag{4.2}$$

For a system of spins, the total Hamiltonian $\widehat{\mathcal{H}}^{total}$ can be represented as a sum of
interaction Hamiltonian terms:

$$\widehat{\mathcal{H}} = \widehat{\mathcal{H}}_Z + \widehat{\mathcal{H}}_{RF} + \widehat{\mathcal{H}}_{CS} + \widehat{\mathcal{H}}_Q + \widehat{\mathcal{H}}_J + \widehat{\mathcal{H}}_{DD} \tag{4.3}$$

The main interactions are [19, 20]:

- $\widehat{\mathcal{H}}_Z$, the Zeeman Hamiltonian that describes the interaction of the nuclear spins with the external static magnetic field, $\vec{B}_0$

- $\widehat{\mathcal{H}}_{RF}$, the RF Hamiltonian. This is a time-dependent Hamiltonian that describes the interaction of the spins with the external time-dependent field $\vec{B}_{RF}(t)$

- $\widehat{\mathcal{H}}_{CS}$, the chemical shift Hamiltonian that describes the effect of electron shielding of $\vec{B}_0$ on the nuclear spins

- $\widehat{\mathcal{H}}_J$, the J-coupling Hamiltonian, or scalar coupling Hamiltonian, that describes the spin-spin interaction that is mediated by the bonding electrons

- $\widehat{\mathcal{H}}_{DD}$, the dipole-dipole coupling Hamiltonian that describes the through-space spin-spin interaction

- $\widehat{\mathcal{H}}_Q$, the quadrupole coupling Hamiltonian that describes the interaction of nuclei having $I > \frac{1}{2}$ with the electric field gradient

4.1.1 Internal and External Spin Interactions

The nuclear spins in a sample interact with electromagnetic fields. These spin interactions can be classified in many different ways. First of all, there are external interactions – with fields generated by objects outside the sample, like magnetic fields generated by the NMR spectrometer (and other devices, e.g. mobile phones), and internal interactions – those generated by sources within the molecules: fellow nuclei that possess a spin, electrons *etc.* The total Hamiltonian for a nuclear spin is therefore a sum of two terms – external and internal:

$$\widehat{\mathcal{H}} = \widehat{\mathcal{H}}_{ext} + \widehat{\mathcal{H}}_{int} \tag{4.4}$$

The external part of the Hamiltonian, $\widehat{\mathcal{H}}_{ext}$, includes two terms that describe the interaction of each individual spin with two kinds of magnetic field that are generated by the spectrometer: the static field, $\vec{B}_0$, and the RF field, $\vec{B}_{RF}(t)$. Hence, $\widehat{\mathcal{H}}_{ext}$ consists of two terms:

$$\widehat{\mathcal{H}}_{ext} = \widehat{\mathcal{H}}_Z + \widehat{\mathcal{H}}_{RF} \tag{4.5}$$

Other random disturbing external fields, that are weak compared to these two, have their effect successfully removed (in most cases) or can be ignored because of their small scale.

The internal Hamiltonian, $\widehat{\mathcal{H}}_{int}$, describes interactions of the spin I with magnetic and electric fields that are generated within the molecular environment. The electric part of the internal Hamiltonian, $\widehat{\mathcal{H}}_{elec}$, exists only in the case of quadrupolar nuclei (those with spin $I > \frac{1}{2}$). The magnetic part of the internal Hamiltonian consists of terms describing interactions of individual spins with the fields in the sample and pairwise interactions between spins.

4.1.2 Single-Spin and Pairwise Interactions

The nuclear interactions described above can be divided into two groups, depending on the number of nuclear spins involved into each of them:

1. Single-spin interactions: Zeeman, RF, chemical shift and quadrupolar. If a spin system consists of different nuclear species I, S and so on, the Hamiltonian term describing an single-spin interaction, X, is:

$$\widehat{\mathcal{H}}_X = \sum_j^{Ispins} \widehat{\mathcal{H}}^j + \sum_k^{Sspins} \widehat{\mathcal{H}}^k + \dots \tag{4.6}$$

2. Pair-wise interactions: J-coupling and dipole-dipole couplings. For a spin system consisting of a number of I, S, *etc* spins, the respective Hamiltonian of a pairwise interaction, Y, is:

$$\widehat{\mathcal{H}}_Y = \sum_j^{Ispins} \sum_{k>j}^{Ispins} \widehat{\mathcal{H}}^{jk} + \sum_l^{Sspins} \sum_{m>l}^{Sspins} \widehat{\mathcal{H}}^{lm} + \frac{1}{2} \sum_j^{Ispins} \sum_l^{Sspins} \widehat{\mathcal{H}}^{jl} + \dots \tag{4.7}$$

Here, $\sum_j^{Ispins} \sum_{k>j}^{Ispins} \widehat{\mathcal{H}}^{jk}$ is a sum over the interactions between the spins of the same kind (I) that are called homonuclear interactions. The term $\frac{1}{2} \sum_j^{Ispins} \sum_l^{Sspins} \widehat{\mathcal{H}}^{jl}$ describes so called heteronuclear interactions, i.e. those between different spin species I and S.

4.2 Coordinate Frames

In total, there are four coordinate systems important for SS NMR:

- the principal axes system, or PAS (P). For each interaction tensor **A**, there is a PAS that is chosen in such a way that the tensor is diagonalised; the x^P, y^P and z^P axes are assigned in such a way that the principal values of the tensor **A** follow the rule: $A_{zz}^P \geq A_{xx}^P \geq A_{yy}^P$. In a molecule consisting of several spin sites, there is a set of P frames. In a powder sample consisting of many crystallites with different orientations, for each crystallite there is its own set of principal axie systems

- the molecular frame (M). This system is used to describe the molecular orientation and its choice is arbitrary

- the rotor-fixed frame R. Its z^R is the rotor axis (the one around which the NMR sample is rotated)

- the laboratory frame (L). It is chosen to have its z^L-axis parallel to the static magnetic field $\vec{B}_0$

Objects (vectors and tensors) that are expressed in these coordinate systems, are denoted with respective superscripts: L, P, R, M. The mutual relation of these coordinate frames is illustrated in Fig. 4.1.

4.3 Euler Angles

Three angles are needed to describe the relative orientation of two coordinate systems A into B. In SS NMR, it is customary to use the Euler angles $\Omega_{AB} = (\alpha_{AB}, \beta_{AB}, \gamma_{AB})$. There are several definitions of the Euler angles in the literature. The convention used in this thesis consists of the following steps [21]:

- rotation around the original z_A-axis, until y_A is perpendicular to both z_A and z_B (α_{AB})

- rotation around the original y_A-axis, until the two z-axes coincide (β_{AB})

- rotation around the original z_A-axis, until the two coordinate systems coincide (γ_{AB})

A vector $\vec{c}^A$ that is expressed in a frame A can be expressed in a frame B as follows:

$$\vec{c}^B = \mathbf{R}^{-1}(\alpha_{AB}, \beta_{AB}, \gamma_{AB})\vec{c}^A \tag{4.8}$$
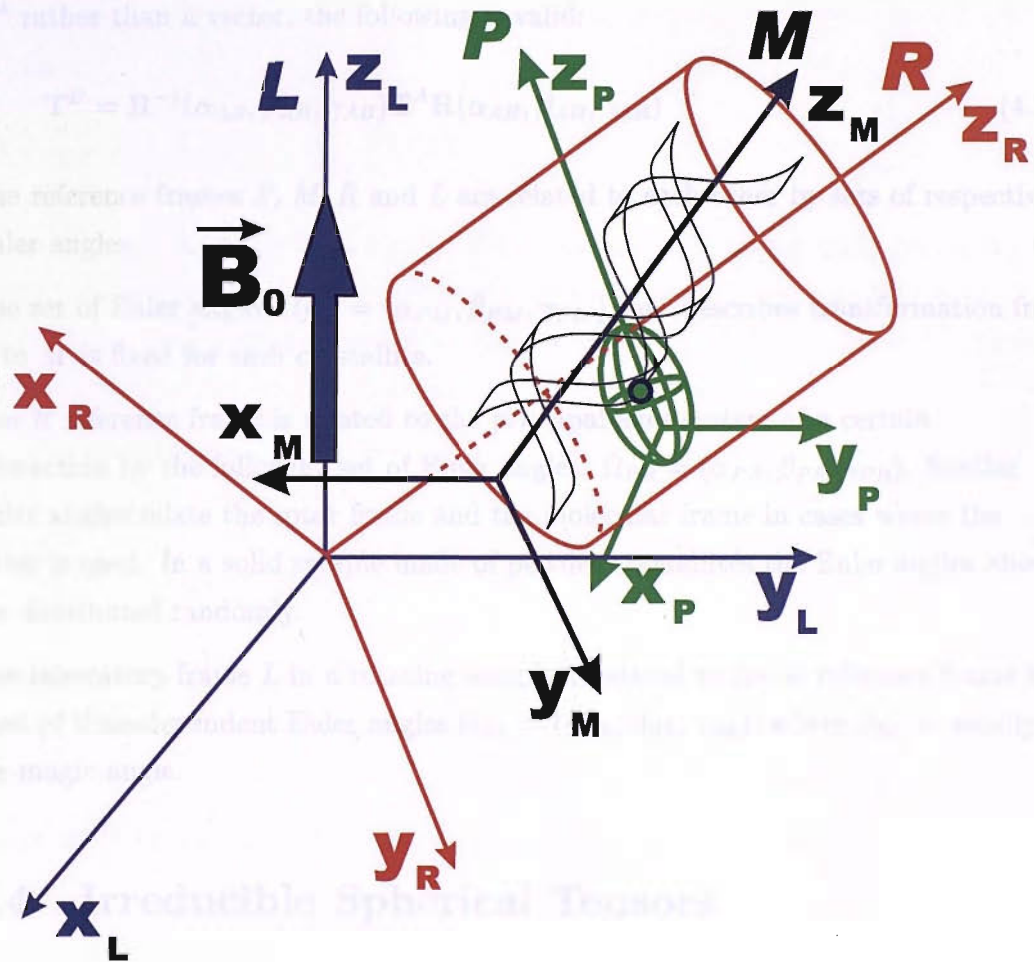
Figure 4.1: Reference frames used in solid-state NMR: laboratory (L), rotor (R), molecular (M) and PAS (P).

where $\widetilde{\mathbf{R}} = \mathbf{R}^{-1}(\alpha_{AB}, \beta_{AB}, \gamma_{AB})$ is the Euler rotational matrix:

$$\widetilde{\mathbf{R}} = \begin{pmatrix} c_\alpha c_\beta c_\gamma - s_\alpha s_\gamma & -c_\alpha c_\beta s_\gamma - s_\alpha c_\gamma & c_\alpha s_\beta \\ s_\alpha c_\beta c_\gamma + s_\alpha s_\gamma & -s_\alpha c_\beta s_\gamma + c_\alpha c_\gamma & s_\alpha s_\beta \\ -s_\beta c_\gamma & s_\beta s_\gamma & c_\beta \end{pmatrix} \tag{4.9}$$

The following abbreviations are used: $c_\alpha = \cos \alpha_{AB}$, $s_\alpha = \sin \alpha_{AB}$, *etc.*

If the object to be transformed between the coordinate frames A and B is a *tensor* $\mathbf{T}^A$ rather than a vector, the following is valid:

$$\mathbf{T}^B = \mathbf{R}^{-1}(\alpha_{AB}, \beta_{AB}, \gamma_{AB}) \mathbf{T}^A \mathbf{R}(\alpha_{AB}, \beta_{AB}, \gamma_{AB}) \tag{4.10}$$

The reference frames P, M, R and L are related to each other by sets of respective Euler angles.

The set of Euler angles $\Omega_{PM} = (\alpha_{PM}, \beta_{PM}, \gamma_{PM})$ that describes transformation from P to M is fixed for each crystallite.

The R reference frame is related to the principal axes system of a certain interaction by the following set of Euler angles: $\Omega_{PR} = (\alpha_{PR}, \beta_{PR}, \gamma_{PR})$. Similar Euler angles relate the rotor frame and the molecular frame in cases where the latter is used. In a solid sample made of powder crystallites the Euler angles above are distributed randomly.

The laboratory frame L in a rotating sample is related to the R reference frame by a set of time-dependent Euler angles $\Omega_{RL} = (\alpha_{RL}, \beta_{RL}, \gamma_{RL})$, where β_{RL} is usually the magic angle.

4.4 Irreducible Spherical Tensors

In general, any Hamiltonian operator in NMR can be presented in the following form [19]:

$$\widehat{\mathcal{H}} = C \widehat{\vec{I}} \cdot \mathbf{A} \cdot \widehat{\vec{J}} \tag{4.11}$$

where C is a constant, $\widehat{\vec{I}}$ and $\widehat{\vec{J}}$ are vector operators (the former one is a spin operator and the latter one depends on the particular spin interaction), and **A** is the second-rank tensor (a 3×3 matrix), specific for the interaction, that describes its strength and spatial orientation. Depending on whether the interaction is single-spin or two-spin, the interaction Hamiltonian can be presented in one of the following formats, respectively:

$$\widehat{\mathcal{H}} = C\widehat{\vec{I}} \cdot \mathbf{A} \cdot \vec{B} \qquad (4.12)$$

or

$$\widehat{\mathcal{H}} = C\widehat{\vec{I}} \cdot \mathbf{A} \cdot \widehat{\vec{S}} \qquad (4.13)$$

where $\vec{B}$ is the magnetic field vector. Here, everything is presented in terms of Cartesian operators and tensors. Sometimes, when several reference frames are involved and transformations between them are to be performed easily, it is more convenient to use the so-called *irreducible spherical tensors.*

Transformations of an irreducible spherical tensor **X** of a rank ℓ from a reference frame A into a frame B can be written as follows:

$$[\mathbf{X}^{(\ell)}]^B = [\mathbf{X}^{(\ell)}]^A D^{(\ell)}(\Omega_{AB}), \qquad (4.14)$$

where $\Omega_{AB} = (\alpha_{AB}, \beta_{AB}, \gamma_{AB})$ is the set of three Euler angles that describe rotation from one frame to the other, and $D^{(\ell)}(\Omega_{AB})$ is the Wigner rotation matrix [21, 22]. This expression serves as a definition of irreducible spherical tensors.

Equation (4.14) can be written in components:

$$[X_{\ell m}]^B = \sum_{m'=-\ell}^{+\ell} [X_{\ell m'}]^A D^{(\ell)}_{m'm}(\Omega_{AB}), \qquad (4.15)$$

where the components of the Wigner rotation matrix are defined as following:

$$D^{(\ell)}_{m'm}(\alpha, \beta, \gamma) = \exp(-im'\alpha)d^{(\ell)}_{m'm}(\beta)\exp(-im\gamma). \qquad (4.16)$$

Here, $d_{m'm}^{(\ell)}(\beta)$ are the reduced Wigner rotation elements and are found from a table (e.g. [23, 24]) or directly calculated from the following expression:

$$d_{m'm}^{(\ell)}(\beta) = \sum_p \frac{(-1)^p \sqrt{(\ell + m')!(\ell - m')!(\ell + m)!(\ell - m)!}}{p!(\ell + m' - p)!(\ell - m - p)!(p + m - m')!} \times \quad (4.17)$$

$$(\cos{(\beta/2)})^{2\ell-2p-m+m'} \left(-\sin{(\beta/2)}\right)^{2p+m-m'}$$

where the summation is over values of p for which the denominator is finite.

If the rotation between A and B occurs via an intermediate frame C the matrix elements $D_{mm'}^{(\ell)}(\Omega_{AB})$ are found from

$$D_{mm'}^{(\ell)}(\Omega_{AB}) = \sum_{m''} D_{mm''}^{(\ell)}(\Omega_{AC}) \cdot D_{m''m'}^{(\ell)}(\Omega_{CB}). \quad (4.18)$$

In general, it can be shown that the expression for the Hamiltonian (4.11) is equivalent to the following scalar product:

$$\widehat{\mathcal{H}} = \sum_{\ell=0}^{2} \sum_{m=-\ell}^{+\ell} (-1)^m \Lambda_{\ell-m} \widehat{T}_{\ell m} \quad (4.19)$$

where $\Lambda_{\ell-m}$ and $\widehat{T}_{\ell m}$ are the components of the spherical tensors Λ and $\widehat{T}$, respectively. They are called the *spin part* $\widehat{T}$ and the *space part* Λ of the Hamiltonian. ℓ here denotes the rank of the tensors. For all the interactions in spin-$\frac{1}{2}$ systems, $\ell = 0, 1, 2$.

4.5 High-field Approximation

It is possible to simplify the internal Hamiltonian terms by using the *secular* approximation (also referred to as the *high-field* approximation) that applies well in the majority of cases. For spins-$\frac{1}{2}$, the large interaction of the spins with the external field $\vec{B}_0$ masks some of the components of the internal Hamiltonian terms. Each of the internal interaction Hamiltonians $\widehat{\mathcal{H}}_i^{int}$ can be substituted by a simplified $\widehat{\mathcal{H}}_i^{int(0)}$ that only contains secular terms (those that commute with $\widehat{I}_z$). However, in some cases of nuclei with spins $I \geq 1$, the secular approximation is not justified.

Within the high-field approximation, equation (4.19) can be simplified by removing all those interaction contributions whose spin-parts do not commute with the $\widehat{I}_z$ operator. It is possible to show that $\widehat{T}_{00}, \widehat{T}_{10}$ and $\widehat{T}_{20}$ (for non-quadrupolar nuclei) are the only secular terms. Therefore, equation (4.19) can be rewritten as

$$\widehat{\mathcal{H}}^{sec} = \sum_{\ell=0}^{2} \Lambda_{\ell 0} \widehat{T}_{\ell 0} \tag{4.20}$$

Both irreducible spherical tensors Λ and $\widehat{T}$ have to be expressed in the same reference frame, of course. It should be noticed that equation (4.20) is not accurate for the quadrupolar case (see Section 4.11).

4.6 The Zeeman Interaction

Superconducting NMR magnets generate a strong static uniform magnetic field $\vec{B}_0$ that has components $(0,0,B_z^0)$ (in *Laboratory* reference frame). Interaction of the field with the isolated spins I_j is described by the Zeeman Hamiltonian:

$$\widehat{\mathcal{H}}_Z^j = -\vec{\mu} \cdot \vec{B}_0 = -\gamma_I \widehat{\vec{I}}_j \vec{B}_0 = -\gamma_I B_z \widehat{I}_{jz} = \omega_j \widehat{I}_{jz} \tag{4.21}$$

where ω_j is the Larmor frequency of precession for the I_j-spins. There are $(2I_j + 1)$ non-degenerate energy levels.

4.7 The RF Hamiltonian

The RF field $\vec{B}_{RF}$ is generated by the radiofrequency coils. It is directed parallel to the x^L-axis. This field is much weaker than the static magnetic field $\vec{B}_0$. However, it oscillates with such a frequency (denoted ω_{RF} for RF frequency) that it is resonant with the Larmor frequency of the spin-I_j-species. When the pulse gate is open, the RF field changes according to

$$\vec{B}_{RF}(t) = B_{RF} \cos(\omega_{RF} t + \varphi_p) \vec{e_x} \tag{4.22}$$

where B_{RF} is the amplitude of the RF field, φ_p is the phase of the pulse, and $\vec{e_x}$ is a vector with coordinates $(1,0,0)$. This oscillating field can be decomposed into a sum of two components rotating in opposite directions: $B_{res}^{RF}(t)$ and $B_{nonres}^{RF}(t)$. Only the resonant component (the one that rotates in the same sense as the spin precession) affects the spin motion. The other one can be neglected. Thus, the RF Hamiltonian term can be written as

$$\widehat{\mathcal{H}}_{RF}^{j}(t) = -\frac{1}{2}\gamma_I B_{RF}\Big(\cos(\omega_{RF}t + \varphi_p)\widehat{I}_{jx} + \sin(\omega_{RF}t + \varphi_p)\widehat{I}_{jy} \Big)$$
$$= \omega_{nut}^{j}\Big(\cos(\omega_{RF}t + \varphi_p)\widehat{I}_{jx} + \sin(\omega_{RF}t + \varphi_p)\widehat{I}_{jy} \Big) \tag{4.23}$$

where ω_{nut}^{j} is the nutation frequency of the I_j-spins.

For convenience, the coordinate frame that rotates at the frequency ω_{RF} is used. In this frame, the resonant component of the radio-frequency field appears static. The RF Hamiltonian term in this frame is expressed as

$$\widehat{\widetilde{\mathcal{H}}}_{RF} = \omega_{nut}\Big(\cos\varphi_p\widehat{I}_x + \sin\varphi_p\widehat{I}_y \Big) \tag{4.24}$$

This choice of reference frame is very convenient in NMR. The Larmor frequency ω_0 (in MHz) becomes a relative Larmor frequency $\Omega_0 = \omega_0 - \omega_{RF}$. As ω_{RF} is resonant with ω_0, their difference typically has the order of kHz. The spectrum of a spin I in the presence of the static field $\vec{B}_0$ with scaled down frequency is shown in Fig. 4.2.

4.8 Chemical Shift Hamiltonian

The chemical shift is probably the most important interaction in NMR. Being proportional to the gyromagnetic ratio, unique for every kind of nuclei, it helps determine different spin species. Because it is very sensitive to the local environment, it helps to distinguish spin sites within different chemical groups, for instance ^{13}C nuclei from aromatic rings, CH_3-, CH_2- and COOH-groups have chemical shifts that are different enough to be able to distinguish them.

Nuclei in the sample are surrounded by electrons. In the presence of the strong static magnetic field $\vec{B}_0$, electrons near the nuclei create an induced magnetic field,

$\vec{B}_{ind}$, that (in diamagnetic substances) opposes the external static field (see
Fig. 4.3). The nuclear spin experiences a local field, $\vec{B}_{loc}$, that is given by

$$\vec{B}_{loc} = \vec{B}_0 + \vec{B}_{ind} \tag{4.25}$$

The resulting field $\vec{B}_{loc} = \vec{B}_0 + \vec{B}_{ind}$ reflects the local environment of the site and is
different for nuclei within different groups – this is the origin of the chemical shift.
In general, in contrast to the static field $\vec{B}_0$ that has $B_{0x}^L = 0$ and $B_{0y}^L = 0$, the
induced field $\vec{B}_{ind}$ is not parallel to the z-axis in the laboratory frame L but also has
x- and y- components, because the electronic charge distribution around a nucleus
is not spherical. It is proportional to the static field:

$$\vec{B}_{ind}^j = \delta_j \vec{B}_0 \tag{4.26}$$

where δ_j is the chemical shift (or shielding) tensor of the spin site I_j. It is a rank 2
tensor, i.e. a 3×3 matrix. Therefore, the local field $\vec{B}_{loc}$ has three components. The
precession frequency of the I_j-spins is shifted by the electronic environment.
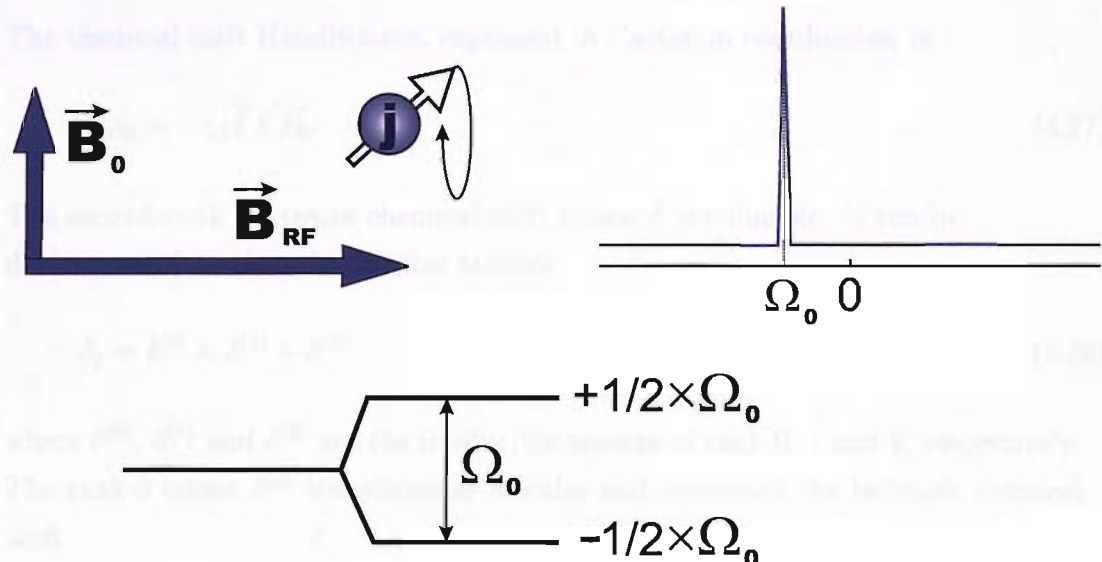
Figure 4.2: An isolated site j with $I = \frac{1}{2}$ gives a single spectral NMR line at relative
frequency Ω_0.

The chemical shift interaction can be quite large, up to several hundred kHz.

An imaginary spectrum for the case of liquids and (at high spinning frequency) powder solid samples is shown in Fig. 4.3. The spectral line is shifted because the Larmor frequency is proportional to the magnetic field that the spin feels ($\vec{B}_{loc}$ instead of $\vec{B}_0$).
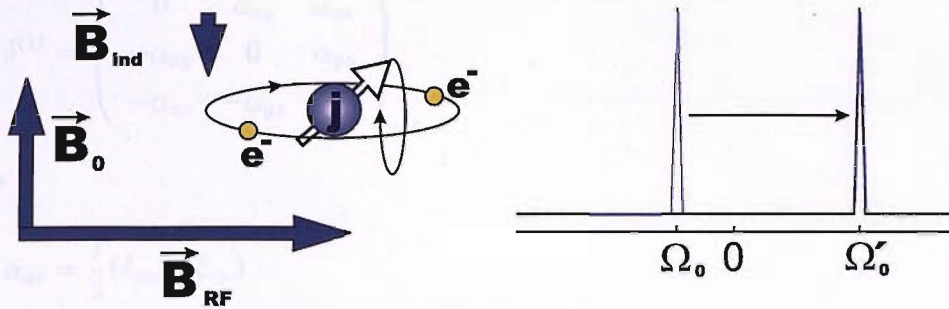
Figure 4.3: A spectrum of a site j with $I = \frac{1}{2}$ in the presence of electrons in an atomic orbital. The frequency of the spectral NMR line is shifted compared to the case of nuclei completely isolated from their surrounding spins.

The chemical shift Hamiltonian, expressed in Cartesian coordinates, is:

$$\widehat{\mathcal{H}}_{CS} = -\gamma_I \widehat{\vec{I}} \, \delta \, \vec{B}_0 \tag{4.27}$$

The second-rank Cartesian chemical shift tensor δ is reducible. It can be decomposed into three irreducible tensors:

$$\delta_j = \delta^{(0)} + \delta^{(1)} + \delta^{(2)} \tag{4.28}$$

where $\delta^{(0)}$, $\delta^{(1)}$ and $\delta^{(2)}$ are the irreducible tensors of rank 0, 1 and 2, respectively. The rank-0 tensor $\delta^{(0)}$ transforms as a scalar and represents the isotropic chemical shift:

$$\delta^{(0)} = \frac{1}{3}\delta_{iso} \begin{pmatrix} 1 & 0 & 0 \\ 0 & 1 & 0 \\ 0 & 0 & 1 \end{pmatrix} \tag{4.29}$$

where δ_{iso} is the trace of the δ tensor:

$$\delta_{iso} = \frac{1}{3}(\delta_{xx} + \delta_{yy} + \delta_{zz}) \tag{4.30}$$

The rank-1 tensor represents the antisymmetrical chemical shift.

$$\delta^{(1)} = \begin{pmatrix} 0 & \alpha_{xy} & \alpha_{xz} \\ -\alpha_{xy} & 0 & \alpha_{yz} \\ -\alpha_{xz} & -\alpha_{yz} & 0 \end{pmatrix} \tag{4.31}$$

where

$$\alpha_{uv} = \frac{1}{2}(\delta_{uv} - \delta_{vu}) \tag{4.32}$$

If the high-field approximation is valid, the rank-1 term can be neglected.

The last term, $\delta^{(2)}$, describes the chemical shift anisotropy. It is traceless and symmetric and equal to

$$\delta^{(2)} = \begin{pmatrix} \beta_{xx} & \beta_{xy} & \beta_{xz} \\ \beta_{yx} & \beta_{yy} & \beta_{yz} \\ \beta_{zx} & \beta_{zy} & \beta_{zz} \end{pmatrix} \tag{4.33}$$

where

$$\beta_{uv} = \frac{1}{2}(\delta_{uv} + \delta_{vu} - 2\delta_{iso}) \tag{4.34}$$

In its own *PAS*, the CSA tensor is diagonal:

$$\delta^P = \begin{pmatrix} \delta^P_{xx} & 0 & 0 \\ 0 & \delta^P_{yy} & 0 \\ 0 & 0 & \delta^P_{zz} \end{pmatrix} \tag{4.35}$$

The diagonal elements of the CSA tensor in the P reference frame, δ^P_{xx}, δ^P_{yy} and δ^P_{zz}, are its principal values. According to the convention of labelling the *PAS* axes [25]

$$\mid \delta^P_{zz} - \delta_{iso} \mid \geq \mid \delta^P_{xx} - \delta_{iso} \mid \geq \mid \delta^P_{yy} - \delta_{iso} \mid \tag{4.36}$$

There are two parameters that are used to describe the CSA: the anisotropy, ω_{aniso}, and the asymmetry, η:

$$\omega_{aniso} = \omega_0(\delta_{zz}^P - \delta_{iso}) \tag{4.37}$$

$$\eta = \frac{\delta_{yy}^P - \delta_{xx}^P}{\delta_{zz}^P - \delta_{iso}} \tag{4.38}$$

In terms of irreducible spherical tensors, the CS Hamiltonian is expressed as follows:

$$\widehat{\mathcal{H}}_{CS} = -\sum_{\ell=0}^{N} \sum_{m=-\ell}^{+\ell} (-1)^m \Lambda_{\ell-m} \widehat{T}_{\ell m} \tag{4.39}$$

In the high-field approximation, this reduces to:

$$\widehat{\mathcal{H}}_{CS} = -\sum_{\ell=0}^{2} \Lambda_{\ell 0} \widehat{T}_{\ell 0} \tag{4.40}$$

In the L reference frame, the spin-field part $\widehat{T}$ of the CS Hamiltonian has the following components:

$$\widehat{T}_{00}^{(L)} = \frac{1}{\sqrt{3}} \widehat{\vec{I}} \cdot \vec{B}_0 = \frac{1}{\sqrt{3}} \widehat{I}_z B_0 \tag{4.41}$$

$$\widehat{T}_{10}^{(L)} = 0$$

$$\widehat{T}_{20}^{(L)} = \frac{1}{\sqrt{6}} (3\widehat{I}_z B_z - \widehat{\vec{I}} \cdot \vec{B}_0) = \sqrt{\frac{2}{3}} \widehat{I}_z B_0$$

The components of the space part of the Hamiltonian Λ have simple form in P frame:

$$\Lambda_{00}^{(P)} = -\sqrt{3}\gamma\delta_{iso} \tag{4.42}$$

$$\Lambda_{20}^{(P)} = \sqrt{\frac{3}{2}}\gamma(\delta_{zz}^P - \delta_{iso})$$

$$\Lambda_{2\pm1}^{(P)} = 0$$

$$\Lambda_{2\pm2}^{(P)} = -\frac{\eta}{\sqrt{6}}\Lambda_{20}^{(P)}$$

$$\tag{4.43}$$

The $\widehat{T}$ part of the Hamiltonian includes information on the spin and the field, while Λ includes the CSA parameters. However, the constants within the terms $\widehat{T_{00}}^{(L)}\Lambda_{00}^{(L)}$ and $\widehat{T_{20}}^{(L)}\Lambda_{20}^{(L)}$ can be combined and moved into the spin part so that the components of both tensors are redefined to make the expressions simpler:

$$\widehat{T_{00}}^{(L)} = -\widehat{I_z}$$

$$\widehat{T_{10}}^{(L)} = 0 \tag{4.44}$$

$$\widehat{T_{20}}^{(L)} = \widehat{I_z}$$

and

$$\Lambda_{00}^{(P)} = -\omega_0\delta_{iso}$$

$$\Lambda_{20}^{(P)} = -\omega_0(\delta_{zz}^P - \delta_{iso}) \tag{4.45}$$

$$\Lambda_{2\pm1}^{(P)} = 0$$

$$\Lambda_{2\pm2}^{(P)} = \omega_{aniso}$$

Then, the CS Hamiltonian can be written as

$$\widehat{\mathcal{H}}_{CS} = -\omega_0\delta_{iso}\widehat{I_z} + \Lambda_{20}^{(L)}\widehat{I_z} \tag{4.46}$$

The space component $\Lambda_{20}^{(L)}$ can be expressed via components in the P-frame in the following way:

$$\Lambda_{20}^{(L)} = \sum_{\lambda=-2}^{+2} \Lambda_{2\lambda}^{(P)} D_{\lambda0}^{(2)}(\Omega_{PL}) \tag{4.47}$$

In a rotating solid, the transformation from P to L has to be accomplished via the intermediate reference frame R, therefore

$$\Lambda_{20}^{(L)} = \sum_{m=-2}^{+2} \sum_{m'=-2}^{+2} \Lambda_{2m'}^{(P)} D_{m'm}^{(2)}(\Omega_{PR}(t)) D_{m0}^{(2)}(\Omega_{RL}) \tag{4.48}$$

Finally, using expression (4.48), the CS Hamiltonian can be written as

$$\widehat{\mathcal{H}}_{CS} = -\omega_0\delta_{iso}\widehat{I_z} + \sum_{m=-2}^{+2} \sum_{m'=-2}^{+2} \Lambda_{2m'}^{(P)} D_{m'm}^{(2)}(\Omega_{PR}) D_{m0}^{(2)}(\Omega_{RL})\widehat{I_z} \tag{4.49}$$

The chemical shift can provide useful structural information on the spin's surroundings, for instance, for assignment purposes of molecular spin sites (see, for instance, [26]), for studying the mobility of molecular segments [27, 23], *etc.*

4.9 *J*-Coupling

The *J*-coupling is also called the indirect spin-spin coupling. In contrast to the three interactions described above (Zeeman, RF and chemical shift), this is a two-spin interaction. This interaction arises due to the fact that the electron density of bonding electrons is affected by the presence of the nuclear spins. Through this mechanism, the nuclei can feel the presence of each other over several bonds, including hydrogen bonds. The internal Hamiltonian term that describes the *J*-coupling between the sites I_j and I_k, is

$$\widehat{\mathcal{H}}_J^{jk} = 2\pi \widehat{\vec{I}}_j \mathbf{J}_{jk} \widehat{\vec{I}}_k \tag{4.50}$$

where $\mathbf{J}_{jk}$ is the *J*-coupling tensor. Similar to the CS term, the *J*-coupling interaction has isotropic and anisotropic parts. However, in contrast to the CS case, the latter part often is of almost no importance since, even if not averaged by molecular motion, it is often small and can usually be ignored, especially for light nuclei. For a pair of spins I_j and I_k with very different chemical shifts, the presence of *J*-coupling gives rise to two doublets, at (relative) frequencies $(\Omega_j \pm \frac{1}{2} 2\pi J_{jk})$ and $(\Omega_k \pm \frac{1}{2} 2\pi J_{jk})$ (see Fig. 4.4).

Until recently, this interaction was considered to be of little importance in solid-state NMR because of its small scale compared to the other, much stronger, interactions like the direct dipole-dipole and quadrupolar couplings (the typical size of the *J*-coupling is <100 Hz and it is not always noticeable due to the broad solid-state lineshape). However, in high-resolution NMR it provides valuable information on through-bond connectivity [28]. It can also provide information on hydrogen-bond strength [29].

4.10   Dipole-Dipole Coupling

The dipole-dipole coupling is also called the through-space dipole-dipole coupling, or the direct dipole-dipole coupling. It is a pairwise interaction. The magnetic spin I_j generates a magnetic field that interacts with a neighbouring spin site I_k, and *vice versa*. Unlike the J-coupling that is mediated by the bonding electrons (and therefore called indirect), the dipole-dipole coupling acts through space and exists between nuclei that are geometrically in close proximity. The respective internal Hamiltonian term is

$$\widehat{\mathcal{H}}_{DD}^{jk} = -\frac{\mu_0}{4\pi}\frac{\gamma_j\gamma_k\hbar}{r_{jk}^3}\left(3(\widehat{\vec{I}}_j \cdot \vec{e}_{jk})(\widehat{\vec{I}}_k \cdot \vec{e}_{jk}) - \widehat{\vec{I}}_j \cdot \widehat{\vec{I}}_k\right)$$

$$= b_{jk}\left(3(\widehat{\vec{I}}_j \cdot \vec{e}_{jk})(\widehat{\vec{I}}_k \cdot \vec{e}_{jk}) - \widehat{\vec{I}}_j \cdot \widehat{\vec{I}}_k\right) \qquad (4.51)$$

Here, μ_0 is the magnetic permeability in vacuum, r_{jk} and $\vec{e}_{jk}$ are the absolute value of the distance between two spins j and k and the unity vector indicating its direction, respectively, and b_{jk} is the dipole-dipole coupling constant:

$$b_{jk} = -\frac{\mu_0}{4\pi}\frac{\gamma_j\gamma_k\hbar}{r_{jk}^3} \qquad (4.52)$$
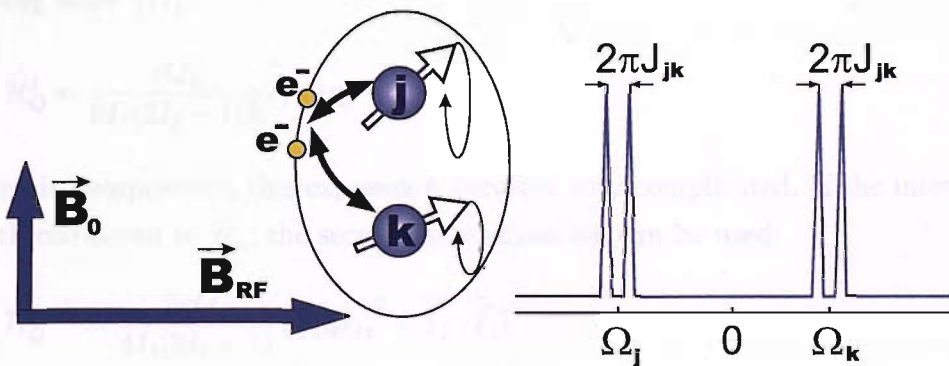
Figure 4.4: A spectrum of two spin-$\frac{1}{2}$ sites I_j and I_k with scalar coupling J_{jk} (the case of AX system, i.e. when the chemical shift frequencies of sites I_j and I_k are far apart).

The dipole-dipole coupling constant contains information on the internuclear distance. The term in brackets in Eq. (4.51) contains information on the $\vec{e}_{jk}$ orientation with respect to the static magnetic field $\vec{B}_0$.

This interaction term contains very useful information, for example, on the internuclear distances (both inter- and intramolecular), the degree of order in the system, *etc.* It can be very large (hundreds of kHz), especially for high γ values and short distances. Being angle-dependent, it survives only in anisotropic medias like liquid crystals and solids. However, in the solid-state NMR of powder samples it is often undesirable because the resulting lines are very broad, leading to poor spectral resolution. In this case it is removed by special experimental procedures (for example magic-angle spinning) [6, 7].

4.11 Quadrupolar Coupling

In contrast to spin-$\frac{1}{2}$ nuclei, the electric charge distribution of the nuclei with spins $I_j \geq 1$ is not spherically symmetric. Therefore, the interaction energy of these quadrupolar nuclei with electric field gradients from the surrounding electrons depends on the nuclear orientation. The quadrupolar Hamiltonian is written in the following form [17]:

$$\widehat{\mathcal{H}}_Q^j = \frac{eQ_j}{6I_j(2I_j-1)\hbar}\widehat{\vec{I}}_j \cdot e\mathbf{q}_j \cdot \widehat{\vec{I}}_j \tag{4.53}$$

Written in components, this expression becomes very complicated. If the interaction is small compared to $\widehat{\mathcal{H}}_z$, the secular approximation can be used:

$$\widehat{\mathcal{H}}_Q^{j\,sec} = \frac{3eQ_j}{4I_j(2I_j-1)}V_0^j(3\widehat{I}_{jz}^{~2} - \widehat{\vec{I}}_j \cdot \widehat{\vec{I}}_j) \tag{4.54}$$

Here, e is the proton charge, Q_j is the electric quadrupole moment of the nucleus j, $\mathbf{q}_j$ is the second-rank tensor that describes the electric field gradient, and V_0^j is the electric field gradient term that depends on the molecular orientation. However, in many cases (especially for solids, but also for isotropic liquids) equation (4.54) does not present a good approximation and more terms are necessary [30, 31].

Quadrupolar NMR is, both practically and theoretically, more complicated than the NMR of spins-$\frac{1}{2}$, but its importance is explained by the fact that the majority of nuclear species possesses a quadrupolar moment. Knowing the quadrupolar parameters of a site j is very useful (for instance, it allows one to determine the local symmetry [32]).

For quadrupolar nuclei with half-integer spins ($I = \frac{3}{2}, \frac{5}{2}, \ldots$), there are two kinds of possible transitions: symmetrical (between the levels ($m \leftrightarrow -m$) and satellite (between the levels $m \leftrightarrow (m \pm 1)$). The only symmetrical transition allowed by the selection rule ($\Delta m = \pm 1$) is $-\frac{1}{2} \leftrightarrow \frac{1}{2}$. It is called the central transition.

Similar to the CSA interaction, the quadrupolar interaction can be described by its anisotropy η:

$$\eta = \frac{q_{xx}^P - q_{yy}^P}{q_{zz}^P} \tag{4.55}$$

where q_{xx}^P, q_{yy}^P and q_{zz}^P are the diagonal elements of the electric field gradient tensor in its *PAS*. The quadrupolar frequency ω_Q is defined as

$$\omega_Q = \frac{2eqQ}{4I(2I-1)} \tag{4.56}$$

where eq is the magnitude of the electric field gradient and the definition of q is

$$q = q_{zz}^P \tag{4.57}$$

As already mentioned, expressed in the laboratory frame, the quadrupolar Hamiltonian looks very complicated. For nuclei with $I = \frac{1}{2}$, all the spin interactions are small compared to the Zeeman interaction. This allows one to use the high-field approximation and truncate the corresponding Hamiltonians to a first-order approximation, i.e., the secular spin interaction Hamiltonian can be written as

$$\widehat{\mathcal{H}} = \widehat{\mathcal{H}}^{(1)} \tag{4.58}$$

For quadrupolar nuclei, however, this is not always the case, because the quadrupolar interactions can be as large as several GHz (for example, for ^{127}I) [33].

For some cases, (4.58) is still valid, but if the quadrupolar interaction is strong, a second-order term in the Hamiltonian has to be taken into account as well. Then, the quadrupolar interaction Hamiltonian $\widehat{\mathcal{H}}_Q$ is written as:

$$\widehat{\mathcal{H}}_Q = \widehat{\mathcal{H}}^{(1)} + \widehat{\mathcal{H}}^{(2)} \tag{4.59}$$

where the first and second order terms are expressed in term of the irreducible spherical tensors in the L reference frame as follows [17]:

$$\widehat{\mathcal{H}}^{(1)} = \frac{e^2 qQ}{4I(2I-1)} \sqrt{6} \Lambda_{20} \widehat{T_{20}} \tag{4.60}$$

$$\widehat{\mathcal{H}}^{(2)} = (\frac{e^2 qQ}{2I(2I-1)})^2 \frac{1}{\omega_0} \frac{2}{5} \left(\left(3\sqrt{10}\widehat{T_{30}} - \widehat{T_{10}}(3 - 4I(I+1)) \right) \Lambda_{00} + \tag{4.61} \right.$$
$$\left(12\sqrt{10}\widehat{T_{30}} - \widehat{T_{10}}(3 - 4I(I+1)) \right) \Lambda_{20} - \left(34\sqrt{10}\widehat{T_{30}} - 3\widehat{T_{10}}(3 - 4I(I+1)) \right) \Lambda_{40} \right)$$

Here, ω_0 is the Larmor frequency. It can be seen from equation 4.61 that in the second-order quadrupolar Hamiltonian there is a term with $\ell = 4$.

The components of the spin spherical tensor in the laboratory frame are defined as:

$$\widehat{T_{10}} = \widehat{I_z} \tag{4.62}$$
$$\widehat{T_{20}} = \frac{1}{\sqrt{6}} (3\widehat{I_z}^2 - I(I+1))$$
$$\widehat{T_{30}} = \frac{1}{\sqrt{10}} (5I_z^2 - 3I(I+1) + 1)\widehat{I_z}$$

$$\tag{4.63}$$

The components of the space part, again in the laboratory reference frame, are:

$$\Lambda_{\ell 0} = \sum_{m=-\ell}^{\ell} D_{m0}^{(\ell)}(\Omega_{RL}) \sum_{n=-\ell}^{\ell} D_{mn}^{(\ell)}(\Omega_{PR}) A_{\ell n} \tag{4.64}$$

The elements $A_{\ell n}$ are expressed via components of the quadrupolar tensor in its PAS [17].

The frequency of the central transition is unaffected by the first-order quadrupolar Hamiltonian, while the satellite transition frequencies are determined by both the first- and second-order quadrupolar Hamiltonians. The second-order Hamiltonian $\widehat{\mathcal{H}}^{(2)}$ is relatively small compared to $\widehat{\mathcal{H}}^{(1)}$, therefore the spectral line corresponding to the central transition is relatively narrow and intense. From this peak, information on the quadrupolar coupling of the nuclear site, such as the quadrupolar coupling constant $\chi = \frac{e^2 qQ}{h}$ and the asymmetry parameter η can be obtained. For integer spins ($I = 1, 2, \ldots$), all the transition lines are substantially broadened.

Chapter 5

Basic Techniques

5.1 Magic-Angle Spinning

The difference between liquid-state (LS) and solid-state (SS) NMR is the degree of molecular motion.

In liquids, the molecules (or other particles) are free to perform isotropic rotational and translational motion. Rotation is particularly important because it averages out NMR interactions that have orientation dependence. For spin-$\frac{1}{2}$ nuclei, the Hamiltonians of such an interaction are proportional to $(3\cos^2\beta_{PL} - 1)$, where β_{PL} is the angle between the z-axes of the PAS of the given interaction and the z-axis of the laboratory frame. The isotropic average value of $\cos^2\beta_{PL}$ is $\frac{1}{3}$, therefore, $< 3\cos^2\beta_{PL} - 1 >= 0$. For quadrupolar nuclei, the angular dependence is different but it still gets averaged out by the motion. Thus, in liquids all the anisotropic interactions (dipole-dipole coupling, CSA, quadrupole coupling) are not directly observable. Spectral lines are narrow and relatively well-resolved.

In solid-state NMR, the situation is quite different. The rotational motions of the molecules are restricted, so most anisotropic interactions remain. Moreover, in the case of powder samples, that consist of a huge number of tiny crystals, each crystallite has its own angular orientation. This results into broad spectral lines (low resolution, low intensity).

In order to approach a liquid-like spectrum, a technique called magic-angle spinning

(MAS) is used [6, 7]. The powder sample is placed in a rotor that is rotated about an axis that is tilted by an angle of 54.7356° with respect to the z-axis of the laboratory frame and spun at a high rotation frequency. Again, the rank-2 anisotropic interactions get averaged out to zero. This is because the average over the rotation phase of the rotor may be shown to be [17]

$$< 3\cos^2\beta_{PL} - 1 > \propto < 3\cos^2\beta_{RL} - 1 >< 3\cos^2\beta_{PR} - 1 > \tag{5.1}$$

where β_{RL} and β_{PR} are the angle between the rotor and laboratory coordinate frames and the angle between the PAS and rotor frame, respectively. The angle β_{RL} is chosen to be equal to $\arctan\sqrt{2}$ in order to put the term $(3\cos^2\beta_{RL} - 1)$ to zero and cancel the anisotropic interactions. This angle is called "magic angle".

For the case of the quadrupole coupling, the quadrupolar frequency is proportional to a sum of terms (see Eq. (4.61)) that are, in turn, proportional to Legendre polynomials $P_2(\cos\beta_{RL})$ and $P_4(\cos\beta_{RL})$:

$$P_2(\cos\beta_{RL}) = \frac{1}{2}(3\cos^2\beta_{RL} - 1) \tag{5.2}$$
$$P_4(\cos\beta_{RL}) = \frac{1}{8}(35\cos^4\beta_{RL} - 30\cos^2\beta_{RL} + 3)$$

So, magic-angle spinning at 54.74° puts the first to zero but not the second. For the second polynomial, an angle of 30.12° is the magic angle. Both conditions $P_2(\cos\beta_{RL}) = 0$ and $P_4(\cos\beta_{RL}) = 0$ can not be satisfied simultaneously and special techniques are used in this case [34, 35, 36].

5.2 Cross-Polarization

Many nuclei that are the subject of NMR experiments have relatively low gyromagnetic ratios. The lower the gyromagnetic ratio is, the lower is the sensitivity of the nucleus (see Table 5.1).

Cross-polarization (CP) [37] transfers magnetization from nuclei with large γ (often ^{1}H) to nuclei with smaller γ (for example, ^{13}C, ^{15}N) and therefore provides enhanced sensitivity. The other problem connected to many nuclei with low

gyromagnetic ratios and low natural abundance is that they tend to have longitudinal relaxation times that are much longer than for the nuclei with high γ and high natural abundance. CP allows one to decrease the pulse delay (the interval between subsequent experiments or transients) by substituting the long relaxation times of the low-γ nuclei by that of the high-γ nuclei. In addition to these two main tasks, CP helps to reduce background signal (from the probe) and provides information about which spins are close in space.

A typical pulse sequence for cross polarization is shown in Fig. 5.1, *a*. First, transverse magnetization on I-nuclei (those with the higher gyromagnetic ratio) is created by applying a 90°-pulse. Then, RF fields are applied to the I and S nuclei with different RF powers in order to satisfy the so-called Hartmann-Hann condition [38]:

$$\omega_S^{nut} = \omega_I^{nut} \tag{5.3}$$

To make the exact match easier to achieve, RF field applied to one of the channels is usually ramped [39, 40, 41]. Contact time of the cross polarization is typically of the order of several ms. As a result of CP, the magnetization of the S-nuclei is ideally enhanced by a factor of around γ_I/γ_S (Fig. 5.1, *b*).

Table 5.1: Description of some of the most commonly used nuclei in NMR.

| Isotope	Spin in the ground state	Natural abundance, %	Gyromagnetic ratio, $\frac{rad}{sT}$
^{1}H	$\frac{1}{2}$	99.98	267.52×10^6
^{13}C	$\frac{1}{2}$	1.108	67.263×10^6
^{15}N	$\frac{1}{2}$	0.37	-27.116×10^6
^{2}H	1	1.5×10^{-2}	41.064×10^6
^{19}F	$\frac{1}{2}$	100	251.665×10^6
^{27}Al	$\frac{5}{2}$	100	69.704×10^6
^{17}O	$\frac{5}{2}$	3.7×10^{-2}	-36.264×10^6
^{31}P	$\frac{1}{2}$	100	108.289×10^6
^{23}Na	$\frac{3}{2}$	100	70.761×10^6
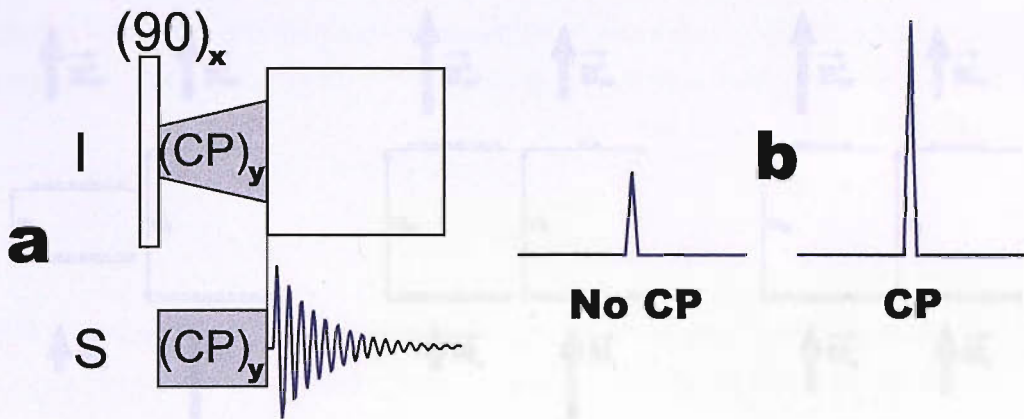
Figure 5.1: *a*, a typical CP pulse sequence; *b*, the result of applying the CP: signal gets stronger.

If CP is applied under MAS, the Hartmann-Hahn condition (5.3) is modified:

$$\omega_I^{nut} = \omega_S^{nut} \pm m\omega_r \qquad (5.4)$$

Here, ω_r is the rotation frequency and $m = \pm 1, \pm 2$ [17]. (For some systems, polarization transfer is also possible for other m, but it is much weaker).

A simple explanation of the CP experiment is presented graphically in Fig. 5.2. First, the same B_{RF} is applied to both nuclei species. As the nutation frequency depends on the value of the gyromagnetic ratios, $\omega^{nutI} \neq \omega^{nutS}$, magnetization transfer is inefficient. When the ratio between B_{RF}^I and B_{RF}^S is such that the Hartmann-Hahn condition is satisfied, magnetization transfer occurs between coupled spins, mediated by the dipolar coupling.

5.3 Heteronuclear Decoupling

MAS helps to remove the effects of anisotropic interactions. However, interaction of S-spins with protons is usually very strong and cannot be completely removed by MAS at any realistic rotation frequency. Residual dipolar couplings make spectral lines broad. Therefore, heteronuclear decoupling should be used during
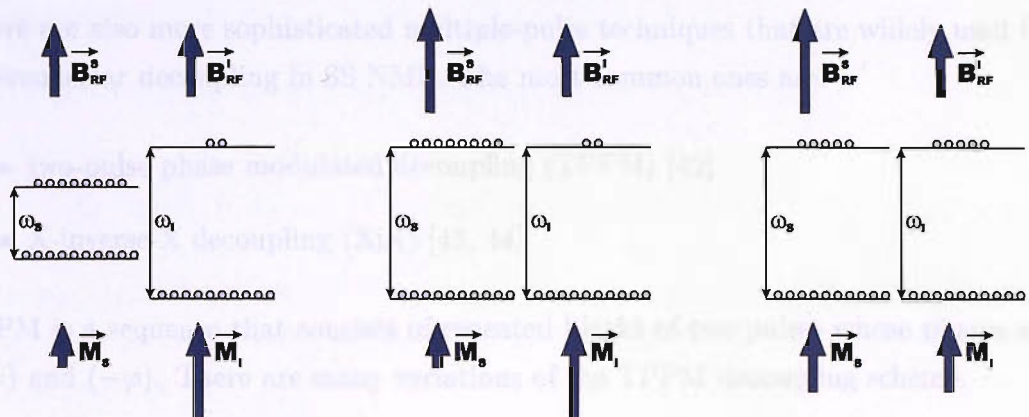
Figure 5.2: When equal RF fields $\vec{B}_{RF}^I = \vec{B}_{RF}^S$ are applied to two nuclei species with the spins I and S, respectively, magnetization exchange is inefficient because their nutation frequencies do not match. If, however, the RF field are adjusted so that the Hartmann-Hahn condition is met, magnetization can "leak" from I to S species.

experiments. The simplest example of decoupling - continuous wave (CW) decoupling - is shown in Fig. 5.3. While the signal is acquired on the S-channel, the
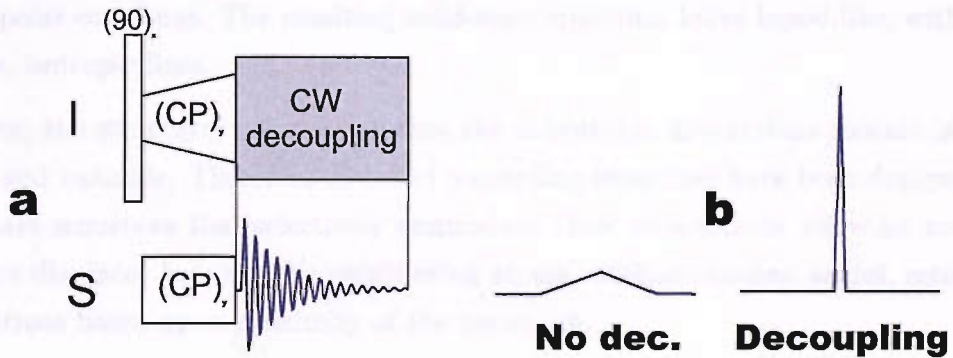
Figure 5.3: a A CP pulse sequence with CW decoupling. b The result of applying the decoupling: spectral lines become narrower.

I-channel (proton channel) is irradiated by a strong RF field in order to decouple the two spin species. With decoupling, the spectral lines get considerably narrower. The RF field applied to the I-channel causes the polarization of I-spins to flip rapidly so that the time-average of the ^{1}H-^{13}C spin-spin interaction cancels out.

There are also more sophisticated multiple-pulse techniques that are widely used for heteronuclear decoupling in SS NMR. The most common ones are:

- two-pulse phase modulated decoupling (TPPM) [42]

- X-inverse-X decoupling (XiX) [43, 44]

TPPM is a sequence that consists of repeated blocks of two pulses whose phases are $(+\varphi)$ and $(-\varphi)$. There are many variations of the TPPM decoupling scheme.

XiX is similar to TPPM. It consists of repeated blocks of two pulses with phases of 0 and π. It has some advantages compared to the TPPM but both give comparable performance [12].

5.4 Recoupling Techniques

Fast MAS and high-power heteronuclear decoupling help to remove the undesirable effects of many interactions in the solid-state NMR of spin-$\frac{1}{2}$ systems, such as CSAs and dipolar couplings. The resulting solid-state spectrum looks liquid-like, with narrow, isotropic lines.

However, the structural information that the anisotropic interactions contain is very useful and valuable. Therefore so-called recoupling sequences have been designed. These are sequences that selectively reintroduce these interactions, allowing one to measure distances between the neighboring atoms, estimate torsion angles, establish correlations based upon proximity of the nuclei, *etc.*

Today, a great number of recoupling techniques exist. They are based on different principles. Some of the most popular recoupling methods are:

- rotational resonance (R^2) [45]

- HORROR (Homonuclear Rotary Resonance) [46] and DREAM (Dipolar Recoupling Enhanced by Amplitude Modulation)

- REDOR [47]

- RFDR [48]

- symmetry-based C-type and R-type sequences [49, 50, 51]

5.4.1 C- and R-type Recoupling Sequences

Both the C- and R-type sequences are based on RF irradiation with phase shifted pulses, with an integer number N of pulse elements fitted into integer number n of rotor revolutions.

The difference between these two types is as follows:

- a CN_n^ν sequence consists of a number of so-called C-elements. N C-elements fit into n full rotor revolutions. In the absence of other interactions, each C-element returns the spins into their initial state.

  The phases of the neighbouring C-elements differ by $\frac{2\pi\nu}{N}$. So, the space part of the Hamiltonian rotates n times as the spin part rotates ν times. The meaning of the numbers in a CN_n^ν sequence is illustrated in Fig. 5.4.
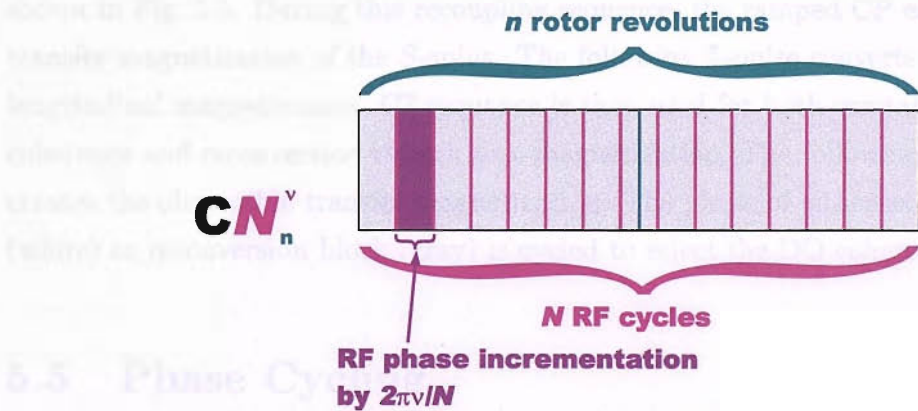

Figure 5.4: Meaning of the numbers in a CN_n^ν sequence.

- an RN_n^ν sequence consists of N/2 R-blocks. Each R-block consists of two R-elements $R_\phi R_{-\phi}$ where the phase ϕ of an R-element is $\phi = \frac{\pi\nu}{N}$. Each R-element is, in general, a composite pulse that rotates the spin through 180°

about the x-axis. N R-elements occupy the same time interval as n sample revolutions.

C-type symmetry implies the following selection rules for the components of the Hamiltonian [49, 50, 51]:

$$\bar{\mathcal{H}}_{\ell m \lambda \mu} = 0, \text{ if } mn - \mu\nu \neq NZ \tag{5.5}$$

where Z is an arbitrary integer. Similarly the selection rules for the R-type sequences are formulated [49]:

$$\bar{\mathcal{H}}_{\ell m \lambda \mu} = 0, \text{ if } mn - \mu\nu \neq \frac{N}{2} Z_\lambda \tag{5.6}$$

where Z_λ is an integer that has the same parity as λ (i.e. Z_λ is odd if λ is odd and Z_λ is even if λ is even). The selection rules allow one to easily predict which interactions are allowed or forbidden by a C- or R-type sequence with certain N, n and ν numbers.

A typical pulse scheme using the C7 double-quantum filtered recoupling sequence is shown in Fig. 5.5. During this recoupling sequence, the ramped CP enhances transfer magnetization of the S-spins. The following $\frac{\pi}{2}$-pulse converts it into longitudinal magnetization. C7 sequence is then used for both excitation of the DQ coherence and reconversion it back to z-magnetization. The following $\frac{\pi}{2}$-pulse creates the observable transfer magnetization. The phase of either excitation block (white) or reconversion block (gray) is cycled to select the DQ coherence.

5.5 Phase Cycling

The desired NMR signals are often polluted by undesirable signals from spin systems of no interest in the experiment, as well as classes of signals from the spin system under study which are of no direct interest. The most common causes of this are hardware and software spectrometer imperfections.

Some of the spectrometer imperfections are relatively easy to deal with. For example, the fact that the accuracy of setting of the spectrometer phases is limited
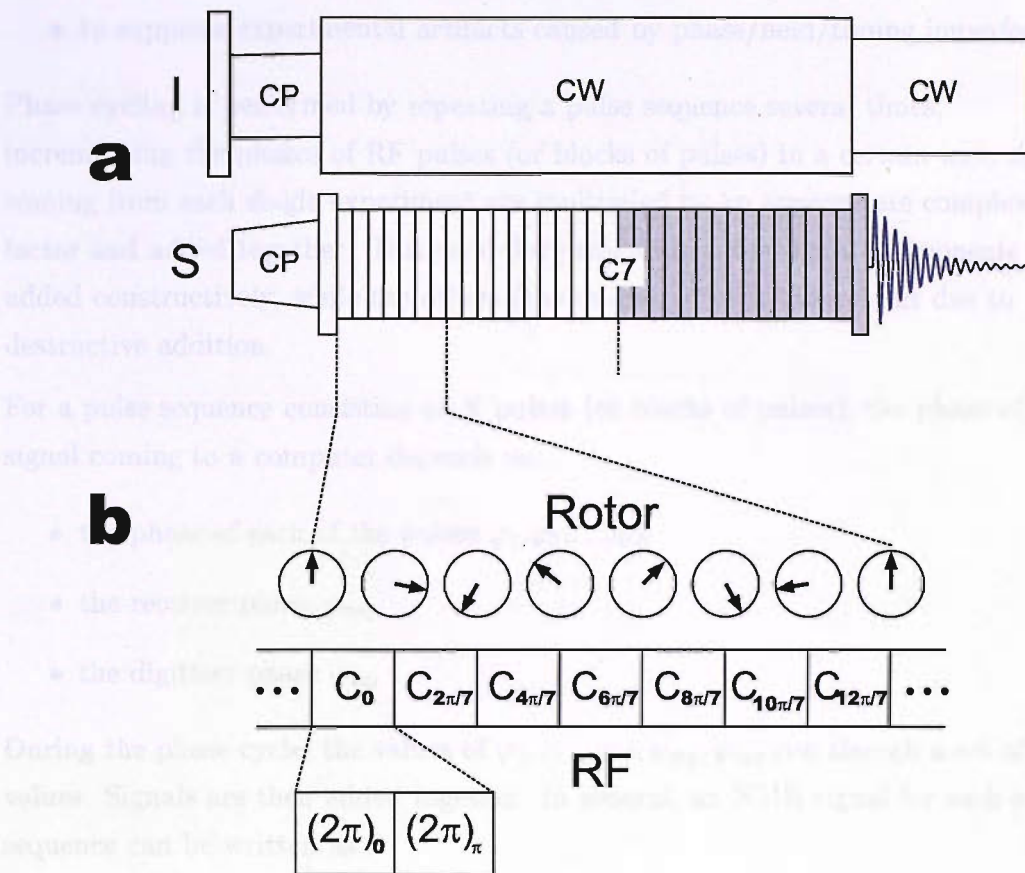
Figure 5.5: *a* - radiofrequency pulse scheme for $C7$ RF pulse sequence. *b* - the structure of a $C7$ cycle in more detail. Adapted from [52].

can be dealt with by choosing such phases that are multiples of a minimal phase changing step. However, some of them cause a problem: imperfections in RF power, imperfections of the quadrature receiver (i.e. such that not only a pure (-1) coherence order is acquired). Often, one may be interested in particular NMR signals, for example, only that coming from ^{13}C nuclei in proximity of ^{1}H nuclei, or to only observe signals of spin pairs or clusters. In all the cases above, applied phase cycles [8, 9] will help to solve the problem.

The main goals of the phase cycling are:

- to select signals having certain properties while canceling out the others;

- to suppress experimental artifacts caused by phase/field/timing imperfections.

Phase cycling is performed by repeating a pulse sequence several times, incrementing the phases of RF pulses (or blocks of pulses) in a certain way; signals coming from each single experiment are multiplied by an appropriate complex factor and added together. This procedure results in some signal components being added constructively, while the others (the undesired ones) cancel out due to destructive addition.

For a pulse sequence consisting of N pulses (or blocks of pulses), the phase of the signal coming to a computer depends on:

- the phase of each of the pulses $\varphi_1, \varphi_2, \ldots, \varphi_N$

- the receiver phase φ_{rec}

- the digitizer phase φ_{dig}

During the phase cycle, the values of $\varphi_1, \ldots, \varphi_N, \varphi_{dig}, \varphi_{rec}$ run though a set of values. Signals are then added together. In general, an NMR signal for such a sequence can be written as

$$s_{total}(t, \varphi_1, \ldots, \varphi_N, \varphi_{dig}, \varphi_{rec}) = \sum_{m=1}^{\mathcal{M}} s_m(t, \varphi_1^m, \ldots, \varphi_N^m, \varphi_{dig}^m, \varphi_{rec}^m) \tag{5.7}$$

where $\mathcal{M}$ is the total number of steps in the complete phase cycle. $s_{total}(t, \varphi_1, \ldots, \varphi_N, \varphi_{dig}, \varphi_{rec})$ can also be expressed as follows:

$$s_{total}(t, \varphi_1, \ldots, \varphi_N, \varphi_{dig}, \varphi_{rec}) = \tag{5.8}$$
$$\sum_{m=1}^{\mathcal{M}} s_m(t, \varphi_1^m = 0, \ldots, \varphi_N^m = 0, \varphi_{dig}^m = 0, \varphi_{rec}^m = 0) \cdot \exp(-i\Phi_{path}^m)$$

where $s_m(t, \varphi_1^m = 0, \ldots, \varphi_N^m = 0, \varphi_{dig}^m = 0, \varphi_{rec}^m = 0)$ is a signal that would result from this pulse sequence if all the phases $\varphi_1, \ldots, \varphi_N, \varphi_{dig}, \varphi_{rec}$ were set to zero, and Φ_{path}^m is the total coherence pathway phase. For the mth cycle step, the total coherence pathway phase is defined as:

$$\Phi_{path}^m = \sum_{n=1}^{N} \Delta p_n \varphi_n^m + \varphi_{rec}^m + \varphi_{dig}^m \tag{5.9}$$

where Δp_n is the change of coherence order caused by the nth pulse.

In order for the NMR signal to add constructively (Fig. 5.6, a), the total coherence pathway phase for the desired pathways $p_{desired}$ should be kept constant (e.g. 0) through out the phase cycle. On the other hand, all the unwanted signal components coming from $p_{undesired}$ should add destructively (Fig. 5.6, b) in order to vanish. The following selection rule applies:

$$\frac{1}{\mathcal{M}} \sum_{m=0}^{\mathcal{M}-1} \exp(-i\Phi(p)_{path}^m) = \begin{cases} 1 & \text{if } p \in \{p_{desired}\} \\ 0 & \text{otherwise} \end{cases} \tag{5.10}$$
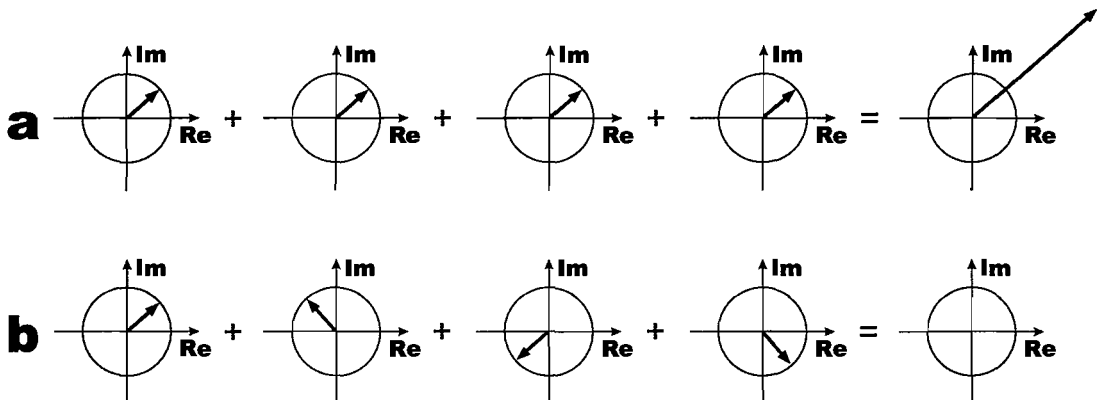
Figure 5.6: Behaviour of NMR signals during a phase cycle. a, for the desired signal components, the total pathway phase is kept constant and signal adds up, b, for other signal components, the signal cancels out.

For the pulse sequence shown in Fig. 5.7, the coherence pathway phase is

$$\Phi_{path} = \Delta p_A \varphi_A + \Delta p_B \varphi_B + \Delta p_C \varphi_C + \varphi_{rec} + \varphi_{dig} = \tag{5.11}$$
$$(-1)\varphi_A + 2\varphi_B + (-2)\varphi_C + \varphi_{rec} + \varphi_{dig}$$

where Δp_A, Δp_B and Δp_C are the changes in the coherence order caused by the respective pulses. Usually, either φ_{rec} or φ_{dig} is cycled.

A simple, realistic two-step phase cycle is shown in Fig. 5.8. Here, the CP block on the ^{1}H channel is cycled with phase according to the list: 0, π. The receiver phase φ_{rec} is adjusted so that to keep Φ_{total} constant, while the digitizer phase φ_{dig} is kept

unchanged. Such pulse phases cause the part of the ^{13}C magnetization, that is cross-polarized from protons, to change sign. The receiver phase cycle lets this signal add up constructively. On the other hand, for the carbon signals arising from the nuclei situated far from protons, the two signals cancel.

5.5.1 Nested Phase Cycling

In *conventional*, or nested, phase cycles, the phases of the pulses (or blocks of pulses in more advanced pulse sequences) are chosen according to:

$$\varphi_n^l = \frac{2\pi}{\mathcal{L}_n} l, \ n = 1, \ldots, \mathcal{N} \tag{5.12}$$

Here, l is the cycle counter for the phase cycle of the nth pulse, $l = 0, \ldots, (\mathcal{L}_n - 1)$, and $\mathcal{L}_n$ is the number of steps of the cycle for this pulse or block. The number of cycle steps for each RF pulse is determined by the desired coherence order change and may be chosen by the spectroscopist. In Fig. 5.9, RF pulses A and B cause the coherence order to change by (+1), each. Pulse A, being cycled in 3 steps, selects not exclusively the (+1)-order but $(+1 \pm 3 \times k)$, where k is a positive integer: $k = 1, 2, 3, \ldots$. Therefore, coherences of (-2) and (+4)-order will survive this cycle
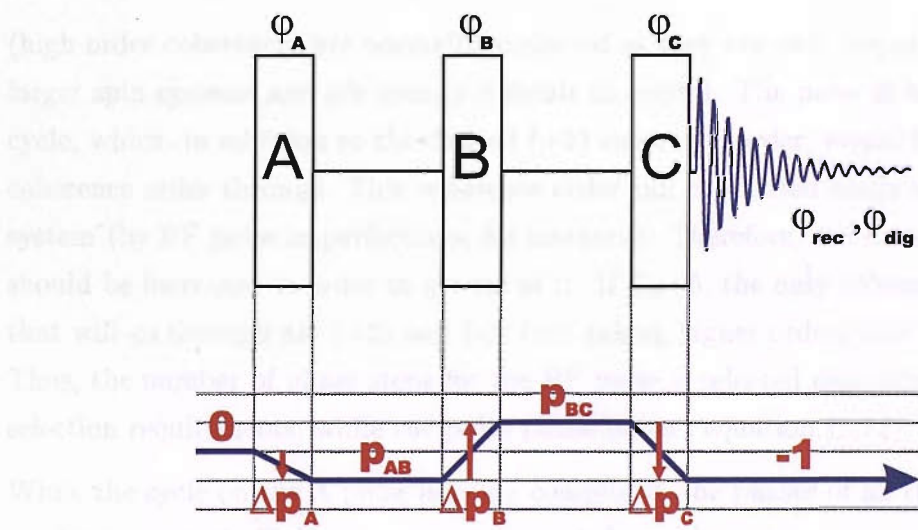

Figure 5.7: A pulse sequence consisting of three pulses.
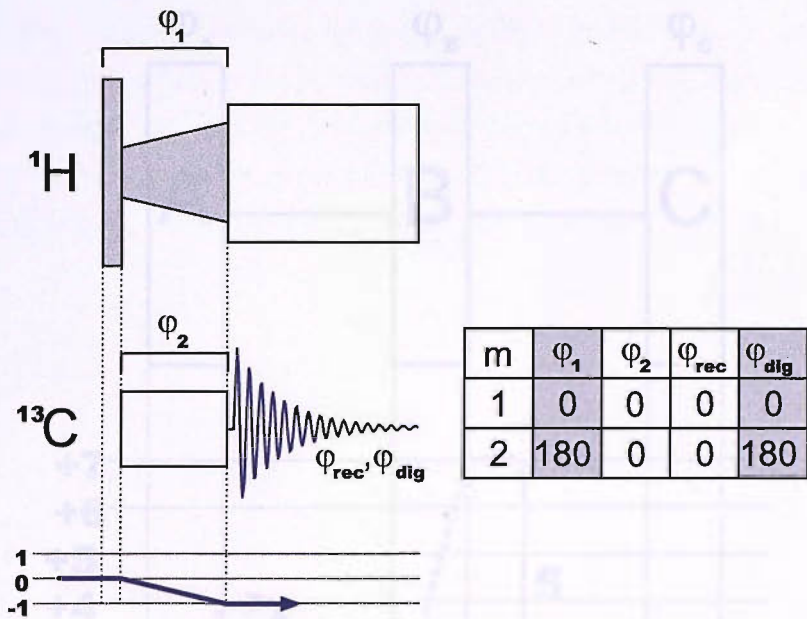
Figure 5.8: CP pulse sequence and the appropriate phase cycle to cancel out the ^{13}C signal from carbons that are not in close proximity to ^{1}H nuclei. The table shows phase values required to perform the phase cycle. (In fact, two coherence pathways $\{0 \to \pm 1\}$ are selected).

(high order coherences are normally neglected as they are only important in case of larger spin systems and are usually difficult to excite). The pulse B has a 3-step cycle, which, in addition to the desired (+2) coherence order, would let the (-1) coherence order through. This coherence order can be excited easily in any spin system (by RF pulse imperfections, for instance). Therefore, the number of steps should be increased in order to get rid of it. If $\mathcal{L}_B = 5$, the only coherence orders that will go through are (+2) and (-3) (not taking higher orders into account). Thus, the number of phase steps for the RF pulse is selected depending on the selection requirements, while the pulse phase follows equation (5.12).

While the cycle on the A pulse is being completed, the phases of all the other pulses are kept constant. Either φ_{dig} or φ_{rec} is cycled together with φ_A to maintain a

adjusted in order to keep the total coherence pathway phase, Φ_{total}, constant. When the phase cycle on the first pulse is completed, the phase of the next one is incremented by one step, and the first one goes through its cycle again, and so on. For a sequence of N pulses, or pulse blocks, with the number of steps of the pulse phase cycle of the nth pulse being called L_n, the total number of phase cycle steps is

$$M = \prod_{n=1}^{N} L_n \tag{5.11}$$

Therefore, one usually tries to keep the number of steps on each phase as low as possible.

5.5.2   Cogwheel Phase Cycling

In cogwheel phase cycling, all the phases of the pulses are incremented simultaneously, each with their own phase increment ν_n. The phase of the nth pulse φ_n is incremented according to

$$\varphi_n = \varphi_n^0 + \frac{2\pi l}{M} \nu_n \qquad l = 0, 1 \dots (M-1) \tag{5.12}$$

The number of steps in the phase cycle, M, is now the same for all the pulses.

Figure 5.9: A pulse sequence needed to select the coherence pathway $0 \rightarrow +1 \rightarrow +2 \rightarrow -1$.

constant value for Φ_{total}:

$$\varphi_{dig/rec} = -\Delta p_A \varphi_A = -\varphi_A \tag{5.13}$$

The phase scheme during the cycling of the pulse A phase is summarized in Table 5.2.

In the conventional (nested) phase cycles [8, 9], the phases of the RF pulses are incremented one at a time. While one pulse phase is cycled, the phases of all the other pulses are kept constant. The receiver and digitiser phases, φ_{rec} and φ_{dig}, are

adjusted in order to keep the total coherence pathway phase Φ_{path} constant. When the phase cycle on the first pulse is completed, the phase of the next one is incremented by one step, and the first one goes through its cycle again, and so on. For a sequence of N pulses (or pulse blocks), with the number of steps of the pulse phase cycle of the nth pulse being equal to $\mathcal{L}_n$, the total number of phase cycle steps is

$$\mathcal{M} = \prod_{n=1}^{N} \mathcal{L}_n \tag{5.14}$$

Therefore, one usually tries to keep the number of steps for each pulse as low as possible.

5.5.2 Cogwheel Phase Cycling

In cogwheel phase cycling [53], the phases of all the pulses are incremented simultaneously, each with its own phase increment ν_n. The phase of the nth pulse φ_n is incremented according to:

$$\varphi_n = \frac{2\pi\nu_n}{\mathcal{M}} m, \qquad m = 0, \dots, (\mathcal{M} - 1) \tag{5.15}$$

The number of steps in the phase cycle, $\mathcal{M}$, is now *common* for all the pulses. When the phase cycle is completed, the phase of the nth pulse will have turned by an angle equal to $\frac{2\pi\nu_n}{\mathcal{M}}\mathcal{M} = 2\pi\nu_n$, i.e. it will have accomplished ν_n full rotations. These numbers ν_n are known as winding numbers.

Table 5.2: Pulse and spectrometer phases while cycling the A pulse in Fig. 5.9.

Step number	Counter m_A	φ_A $= \frac{2\pi}{\mathcal{M}_A} m_a$	φ_{rec}	φ_B	φ_C	φ_{dig}
1	0	0	0	constant	constant	constant
2	1	$\frac{2\pi}{3}$	$-\frac{2\pi}{3}$	constant	constant	constant
3	2	$2 \cdot \frac{2\pi}{3}$	$-2 \cdot \frac{2\pi}{3}$	constant	constant	constant

If a pulse sequence consists of three pulses: A, B and C (Fig. 5.10), and the coherence pathway, as usual, starts with z-magnetization (i.e. (0)-coherence order) and ends with (-1)-order, in the case of ideal quadrature signal acquisition, then the desired coherence pathway is:

$$\mathbf{p}_{desired} = \{0 \to p_{AB} \to p_{BC} \to -1\} \tag{5.16}$$

Here, p_{AB} and p_{BC} denote the coherence orders between the corresponding pulses. In the cogwheel method, the *absolute* coherence order, rather then the *change* in the coherence order as in conventional procedure, is used.
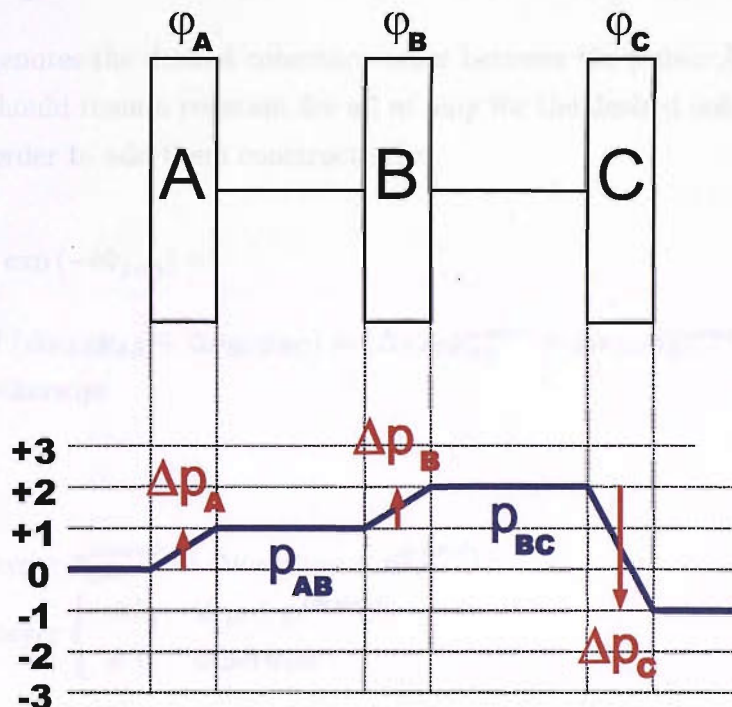

Figure 5.10: A pulse sequence needed to select the coherence pathway $0 \to +1 \to +2 \to -1$.

The total pathway phase is expressed as follows:

$$\Phi_{path}^{(m)} = \Delta p_A \varphi_A^{(m)} + \Delta p_B \varphi_B^{(m)} + \Delta p_C \varphi_C^{(m)} + \varphi_{rec}^{(m)} + \varphi_{dig}^{(m)} = \tag{5.17}$$
$$\frac{2\pi m}{\mathcal{M}} (\nu_A \Delta p_A + \nu_B \Delta p_B + \nu_C \Delta p_C) + \varphi_{rec}^{(m)} + \varphi_{dig}^{(m)}$$

Here, Δp_A, Δp_B and Δp_C are the changes in coherence order caused by pulse A, B or C respectively. It is convenient to introduce quantities $\Delta \nu_{AB}$ and $\Delta \nu_{BC}$, the differences between the corresponding winding numbers:

$$
\Delta \nu_{AB} = \nu_B - \nu_A
$$
$$
\Delta \nu_{BC} = \nu_C - \nu_B \tag{5.18}
$$

Using these notations, equation (5.17) may be written as

$$
\Phi_{path}^{(m)} = \frac{2\pi m}{N}(-\Delta \nu_{AB}(p_{AB} - p_{AB}^{desired}) - \Delta \nu_{BC}(p_{BC} - p_{BC}^{desired})). \tag{5.19}
$$

$p_{XY}^{desired}$ here denotes the desired coherence order between the pulses X and Y. As usual, $\Phi_{path}^{(m)}$ should remain constant for all m only for the desired coherence pathways in order to add them constructively:

$$
\frac{1}{\mathcal{M}} \sum_{m=0}^{\mathcal{M}-1} \exp\left(-i\Phi_{path}\right) = \tag{5.20}
$$
$$
\begin{cases} 1, & \text{if } (\Delta\nu_{AB}p_{AB} + \Delta\nu_{BC}p_{BC}) = (\Delta\nu_{AB}p_{AB}^{desired} + \Delta\nu_{BC}p_{BC}^{desired}) + \mathcal{M} \times \text{integer} \\ 0, & \text{otherwise} \end{cases}
$$

The equation

$$
\Delta\nu_{AB}(p_{AB} - p_{AB}^{desired}) + \Delta\nu_{BC}(p_{BC} - p_{BC}^{desired}) + \tag{5.21}
$$
$$
\mathcal{M} \times \text{integer} \begin{cases} = 0, & \text{if } \mathbf{p} \in \mathbf{p}^{\{desired\}} \\ \neq 0, & \text{otherwise} \end{cases}
$$

is the object for numerical search. Solutions can also be proved graphically [53].

A cogwheel phase cycle is specified by the value of $\mathcal{M}$ and the combination of the winding numbers which satisfy (5.21) for all significant coherence transfer pathways. For a sequence of N pulses, a cogwheel phase cycle consisting of $\mathcal{M}$ steps and winding numbers $\nu_1, \ldots, \nu_N$ can be denoted as $\text{COG}\mathcal{M}$ $(\nu_1, \ldots, \nu_N; \nu_{rec}, \nu_{dig})$.

5.5.3   CTP Selection By Field Gradients

Another method of suppressing experimental artifacts and selecting a desired coherence pathway is by using pulsed field gradients (PFGs) [54, 55]. Normally, the static magnetic field B_0 is made as homogeneous as possible by adjusting the two sets of shims. Gradients make the field inhomogeneous. A gradient along z-axis has the following linear dependence:

$$B_0(z) = B_0 + G_z z \tag{5.22}$$

where G_z is the strength of the gradient and z is the position in the field along the z-axis. Because the precession frequency of the nuclei is directly proportional to the magnetic field applied, the frequency will vary between the top and the bottom of the sample: magnetization vectors in the upper part will rotate faster, and in the lower – slower than they would at constant B_0. Therefore, the magnetization vectors at each time point form a helix. The number of magnetization vector revolutions per unit length depends on the strength of the field gradient, G_z. By later applying the same magnitude of gradient, but with the opposite sign:

$$B_0(z) = B_0 - G_z z \tag{5.23}$$

one unwinds the magnetization vectors and signal can be recorded. The degree of twisting depends not only on the gradient strength but also on the coherence order $\mathcal{Q}$. Coherences precess at a frequency $\omega(\mathcal{Q}) \propto \mathcal{Q} G_z z$, i.e. double-quantum coherences (with $\mathcal{Q}=\pm 2$) rotate twice as fast as single-quantum coherences (with $\mathcal{Q}=\pm 1$), and zero-quantum coherences ($p=0$) do not twist at all. In order to select a certain coherence pathway $\{0 \rightarrow \mathcal{Q}_A \rightarrow \mathcal{Q}_B \rightarrow \mathcal{Q}_C\}$ by this method, the strength of gradients applied after pulses A, B and C should satisfy the following condition:

$$\mathcal{Q}_A G_z^A + \mathcal{Q}_B G_z^B + \mathcal{Q}_C G_z^C = 0 \tag{5.24}$$

where G_z^A, G_z^B and G_z^C are the strength of the respective field gradients.

This method is popular with liquid-state NMR spectroscopists but is usually not used in SS NMR.

5.6 Simulation of NMR Experiments

There are several computer programs available for numerical simulation of an NMR spectrum, for instance ANTIOPE [56], GAMMA [57], STARS [58, 59], SIMPSON [10], *etc.*

The SIMPSON program that is used for the numerical simulations in this thesis, is specially designed for solid-state NMR experiments [10].

All the information that is necessary for the computer simulation of an NMR experiment, such as description of the spin system (i.e. atomic species, parameters describing their chemical shifts and spin-spin interactions between them), experimental parameters (static and RF magnetic field strength, spinning frequency, angle between the rotor axis and the static field direction, sampling rate, *etc*), description of the pulse sequence (positions, durations and phases of the RF pulses, phase values for the phase cycle and so on), acquisition and procession parameters, are included in the input file that is written in the *Tcl* computing language.

All the spin dynamics calculations are performed inside the SIMPSON environment. The program returns an FID that can be processed either within the SIMPSON environment or with the help of any other convenient program.

A scheme of a SIMPSON simulation is shown in Fig. 5.11.
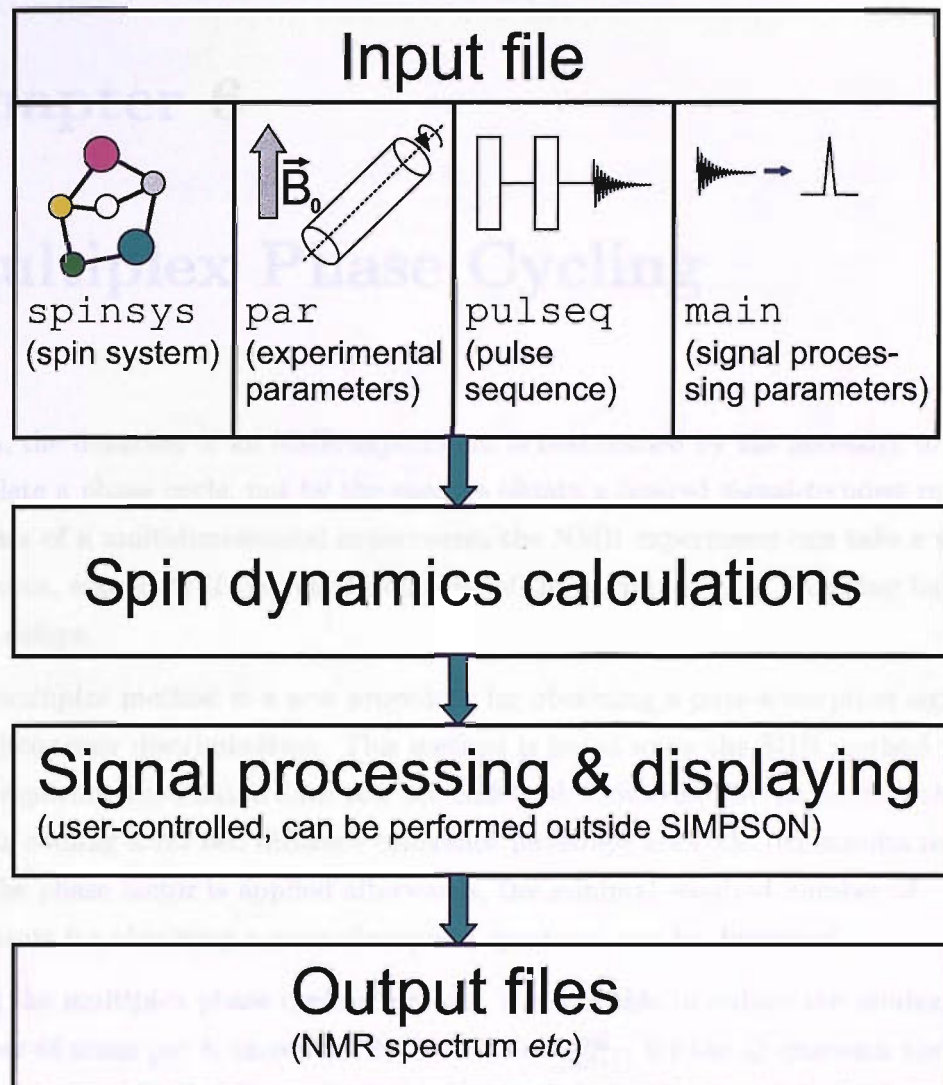
Figure 5.11: A scheme illustrating the process of computer simulation of an NMR spectrum using the SIMPSON program.

Chapter 6

Multiplex Phase Cycling

Often, the duration of an NMR experiment is determined by the necessity to complete a phase cycle, not by the need to obtain a desired signal-to noise ratio. In the case of a multidimensional experiment, the NMR experiment can take a very long time, especially if the relaxation time of the sample is long, requiring long pulse delays.

The *multiplex* method is a new procedure for obtaining a pure-absorption signal, with frequency discrimination. This method is based upon the SHR method where two amplitude-modulated data sets are collected. However, due to the fact that signals coming from two different coherence pathways are collected simultaneously and the phase factor is applied afterwards, the minimal required number of transients for obtaining a pure-absorption spectrum can be decreased.

Using the multiplex phase cycling method, it is possible to reduce the minimal total number of scans per t_1 increment by a factor of $\frac{4Q}{(2Q+1)}$ for the Q-quantum spectrum, which is especially significant for large values of Q, leading to substantial savings in experimental time.

6.1 Theoretical Description

During a multidimensional experiment, a conventional phase cycle is combined with a method for obtaining a pure-absorption spectrum with frequency discrimination.

81

If the SHR procedure is used to obtain a clear absorption peak line shape, cosine-
and sine-modulated signals should be acquired. For each, a full phase cycle has to
be completed. (This takes the same total time as using the TPPI method, for which
only one data set is acquired but the size of the t_1 incrementing step is halved and
their number doubled, see Fig. 6.1).
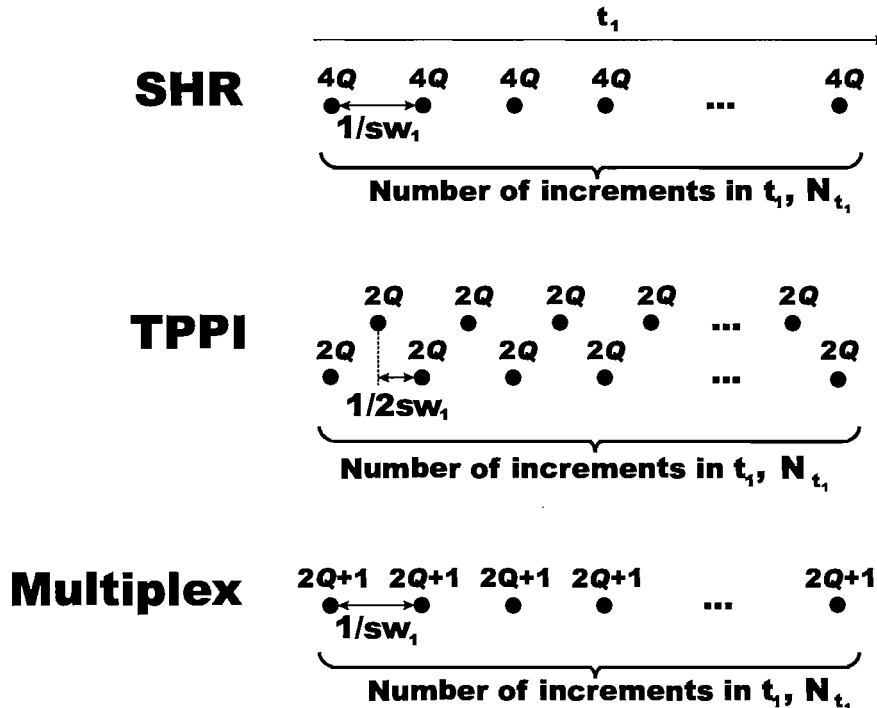
Figure 6.1: Minimum number of transients in the t_1 dimension necessary to obtain
a Q-quantum, pure-absorption spectrum with frequency discrimination for the SHR,
TPPI and multiplex methods is $4Q$, $2 \times 2Q = 4Q$ and $(2Q + 1)$, respectively.

Cosine- and sine-modulated signals are added as the phase cycle is completed:

$$s^{\cos}(t_1, t_2; \varphi_1, \ldots, \varphi_{\mathcal{N}}, \varphi_{rec}, \varphi_{dig}) = \sum_{m=0}^{\mathcal{M}-1} s_m^{\cos}(t_1, t_2; \varphi_1^m, \ldots, \varphi_{\mathcal{N}}^m, \varphi_{rec}^m, \varphi_{dig}^m) \quad (6.1)$$

$$s^{\sin}(t_1, t_2; \varphi_1, \ldots, \varphi_{\mathcal{N}}\varphi_{rec}, \varphi_{dig}) = \sum_{m=0}^{\mathcal{M}-1} s_m^{\sin}(t_1, t_2; \varphi_1^m, \ldots, \varphi_{\mathcal{N}}^m, \varphi_{rec}^m, \varphi_{dig}^m)$$

where $\mathcal{N}$ is the number of pulses, and $\mathcal{M}$ is the total number of steps in the phase
cycle. The signal is then processed and combined according to the SHR method.

Both $(+\mathcal{Q})$ and $(-\mathcal{Q})$ coherence orders are needed in order to obtain the cosine- and sine-modulated $\mathcal{Q}$-quantum signal. This is performed by using an $\mathcal{L}$-step phase cycle in the conventional phase cycling procedure (here, $\mathcal{L}$ is the number of steps in the phase cycle for the pulse that selects the $\mathcal{Q}$-quantum coherence, $\mathcal{L} = 2\mathcal{Q}$).

Alternatively, one can obtain cosine- and sine-modulated $(-\mathcal{Q})$ and $(+\mathcal{Q})$ coherence orders separately and then add them together by applying a minimum $(2\mathcal{Q}+1)$-step phase cycle. In this case, the coherence order of $-(\mathcal{Q}+1)$ will accompany the $\mathcal{Q}$-quantum coherence, and the $(\mathcal{Q}+1)$-quantum coherence will come through together with the $(-\mathcal{Q})$ coherence order. If this is undesirable, the presence of the unwanted coherence orders can be avoided by increasing the number of steps in the phase cycle.

This is, of course, not a good idea as it more than doubles the number of scans needed to complete the phase cycle. However, *one set* of experimental data can be used for obtaining *both the sine- and cosine-modulated signals*, using the multiplex phase cycling method. The basic principle of multiplex phase cycling is shown in Fig. 6.2.

For the $\mathcal{Q}$-quantum experiment in Fig. 6.2, *a*, a conventional phase cycle is used. Both coherence pathways are selected using a $2\mathcal{Q}$ step phase cycle, cycling either the pulse or block of pulses that excites the $(\pm\mathcal{Q})$-quantum coherence (excitation block) or the pulse or block that converts it down to the observable (-1) coherence order (reconversion block).

In Fig. 6.2, *b*, the multiplex procedure is used, with the phase cycle consisting of $\mathcal{L} = (2\mathcal{Q}+1)$. In this case, the two desired coherence pathways are $\mathbf{p}^A = \sum_i \mathbf{p}_i^A$, where $\mathbf{p}_i^A = \{0 \rightarrow \mathcal{Q} + k\mathcal{L} \rightarrow -1\}$ and $\mathbf{p}^B = \sum_i \mathbf{p}_i^B$, where $\mathbf{p}_i^B = \{0 \rightarrow -\mathcal{Q} + k\mathcal{L} \rightarrow -1\}$, where k is an integer. Here, instead of applying the φ_{rec} and φ_{dig} to the NMR signals *during* acquisition while incrementing pulse phase and then adding up the obtained signals, both φ_{dig} and φ_{rec} are kept constant (zero). Individual signals are not immediately combined together but rather stored individually in the computer memory. After the experiment is completed, an appropriate post-acquisition numerical factor φ_{num} is applied. It is calculated

according to either

$$\Phi_{path} + \varphi_{num} = \Delta p_{excit}\varphi_{excit} + \varphi_{rec} + \varphi_{dig} = Const \tag{6.2}$$
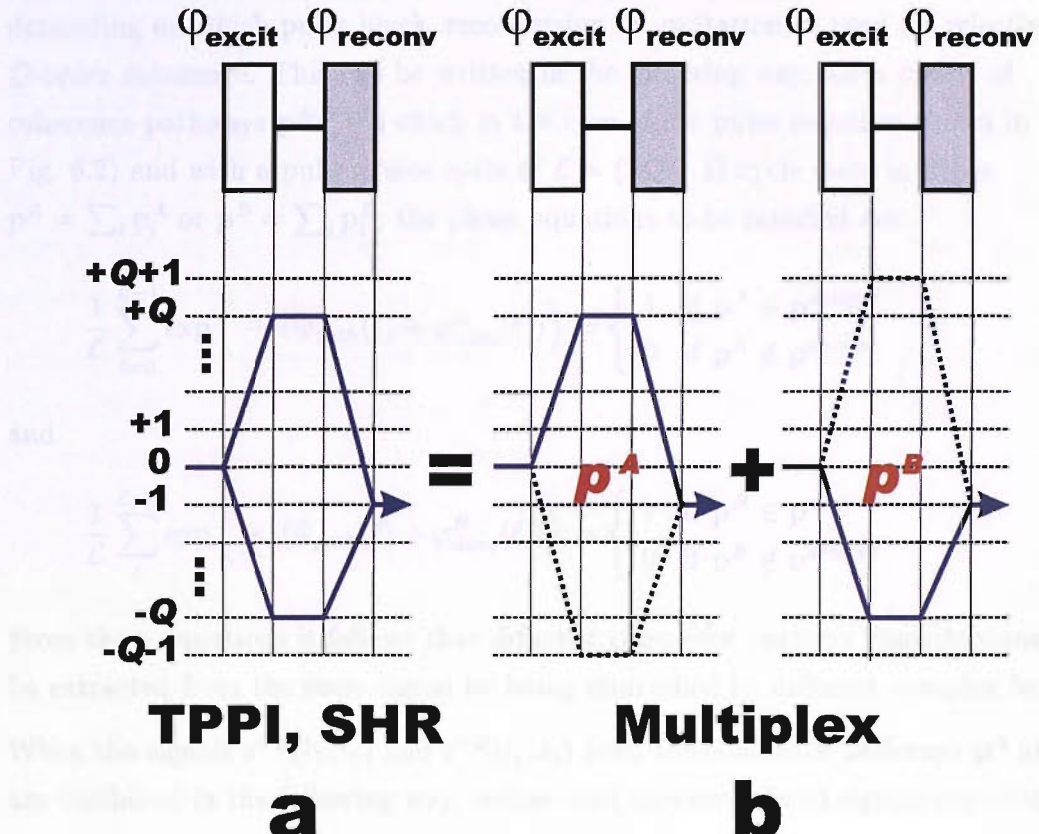

Figure 6.2: Two ways to select coherence pathways $\mathbf{p}^{(+\mathcal{Q})} = \{0 \to +\mathcal{Q} \to -1\}$ and $\mathbf{p}^{(-\mathcal{Q})} = \{0 \to -\mathcal{Q} \to -1\}$ while suppressing all the lower-order coherence pathways $\mathbf{p}^{(0)} = \{0 \to 0 \to -1\}$, $\mathbf{p}^{(\pm 1)} = \{0 \to \pm 1 \to -1\}$, ..., $\mathbf{p}^{(\pm(\mathcal{Q}-1))} = \{0 \to \pm(\mathcal{Q}-1) \to -1\}$ inbetween. *a*, in conventional phase cycling (combined with either TPPI or SHR methods for pure-absorption spectrum) the two pathways $\mathbf{p}^{(+\mathcal{Q})}$ and $\mathbf{p}^{(-\mathcal{Q})}$ are selected simultaneously. *b*, using the multiplex phase cycling procedure, one selects $\mathbf{p}^{(+\mathcal{Q})}$ and $\mathbf{p}^{(-\mathcal{Q})}$ coherence pathways separately; the $\mathbf{p}^{(+\mathcal{Q}+1)}$ and $\mathbf{p}^{(-\mathcal{Q}-1)}$ (dashed lines) pathways come though as well.

or

$$\Phi_{path} + \varphi_{num} = \Delta p_{reconv}\varphi_{reconv} + \varphi_{rec} + \varphi_{dig} = Const \tag{6.3}$$

depending on which pulse block, reconversion or excitation, is used for selecting the $\mathcal{Q}$-order coherence. This can be written in the following way: for a family of coherence pathways $\mathbf{p}^{desired}$ (which in the case of the pulse sequence shown in Fig. 6.2) and with a pulse phase cycle of $\mathcal{L} = (2\mathcal{Q}+1)$ cycle steps is either $\mathbf{p}^A = \sum_i \mathbf{p}_i^A$ or $\mathbf{p}^B = \sum_i \mathbf{p}_i^B$, the phase equations to be satisfied are:

$$\frac{1}{\mathcal{L}}\sum_{\ell=0}^{\mathcal{L}-1} \exp\Big(-i(\Phi_{path}(\ell) + \varphi_{num}^A(\ell))\Big) = \begin{cases} 1 & \text{if } \mathbf{p}^A \in \mathbf{p}^{desired} \\ 0 & \text{if } \mathbf{p}^A \notin \mathbf{p}^{desired} \end{cases} \tag{6.4}$$

and

$$\frac{1}{\mathcal{L}}\sum_{\ell}^{\mathcal{L}-1} \exp\Big(-i(\Phi_{path}(\ell) + \varphi_{num}^B(\ell))\Big) = \begin{cases} 1 & \text{if } \mathbf{p}^B \in \mathbf{p}^{desired} \\ 0 & \text{if } \mathbf{p}^B \notin \mathbf{p}^{desired} \end{cases} \tag{6.5}$$

From these equations it follows that different coherence pathway contributions may be extracted from the same signal by being multiplied by different complex factors.

When the signals $s^{+\mathcal{Q}}(t_1, t_2)$ and $s^{-\mathcal{Q}}(t_1, t_2)$ from the coherence pathways $\mathbf{p}^A$ and $\mathbf{p}^B$ are combined in the following way, cosine- and sine-modulated signals are obtained:

$$s^{\cos}(t_1, t_2) = \frac{1}{2}(s^{-\mathcal{Q}}(t_1, t_2) + s^{+\mathcal{Q}}(t_1, t_2)) \tag{6.6}$$

$$s^{\sin}(t_1, t_2) = \frac{1}{2i}(s^{-\mathcal{Q}}(t_1, t_2) - s^{+\mathcal{Q}}(t_1, t_2))$$

that are then treated according to the SHR procedure in order to obtain the pure-absorption two-dimensional spectrum.

The multiplex procedure can also be used to obtain more then two coherence pathways in a MQ experiment [60]. By applying appropriate digital phase factors it is possible to select pathways $\{0 \to \pm 3 \to +1 \to -1\}$, $\{0 \to \pm 3 \to -1 \to -1\}$ and $\{0 \to \pm 3 \to 0 \to -1\}$ from the same experimental data that leads to a gain of 3 in experiment time.

6.2   Advantages and Disadvantages

Multiplex phase cycling has both advantages and disadvantages compared to conventional phase cycling procedures in the context of pure-absorption two-dimensional spectroscopy.

The reduction in the minimum experiment duration is a very important advantage. The factor of $\frac{4Q}{2Q+1}$ less spectrometer time for the Q-quantum experiment corresponds to a 37.5% time saving for $2Q$, 41.7% for $3Q$, approaching 50% for large coherence orders. This is especially valuable for multi-dimensional NMR experiments with long pulse delays that may take days to acquire.

Another big advantage of the multiplex procedure is that there are cases when the conventional phase cycle simply would not work, but the multiplex method does. An example of such a case is an experiment, where, in a cluster of 3 spins, a set of coherence pathways $\{0 \to \pm 1 \to -1\}$ is to be selected while suppressing $\{0 \to 0 \to -1\}$, $\{0 \to \pm 2 \to 1\}$, and $\{0 \to \pm 3 \to -1\}$ (see Fig. 6.3). There is no way to do this by a conventional phase cycle but it is straightforward to perform using the multiplex phase cycling procedure. The pathway $\{0 \to \pm 3 \to (\pm 1, 0) \to -1\}$ is another example of a case that is not possible to deal with using the conventional phase cycling procedure. (To do either of these experiments, each single pathway should be selected separately and then all of them should be added together to obtain the desired result).

However, there are some disadvantages of these method that should be mentioned. First of all, the computer memory occupied by the NMR data obtained using the multiplex phase cycling procedure is larger by a factor of $\frac{2Q+1}{2}$ compared to that occupied by data acquired using traditional methods (SHR or TPPI). This is due to the fact that the signals are stored individually, while incrementing the pulse phase. This is not a major problem since memory is becoming less expensive.

The second disadvantage is that multiplex signal processing is somewhat more complicated compared to the traditional methods.

6.3   Experimental Demonstration

The multiplex phase cycling procedure is demonstrated on a two-dimensional experiment using the double-quantum recoupling pulse sequence C7. The pulse sequence is shown in Fig. 6.4. It consists of two blocks: excitation and reconversion. The first one excites the double-quantum coherence, and the second one converts it down to the observable (-1)-coherence.

The resulting signal comes from two coherence pathways: $\mathbf{p}^{(+2)} = \{0 \to +2 \to -1\}$ and $\mathbf{p}^{(-2)} = \{0 \to -2 \to -1\}$. The signals coming from the pathways $\mathbf{p}^{(0)} = \{0 \to 0 \to -1\}$ and $\mathbf{p}^{(\pm 1)} = \{0 \to \pm 1 \to -1\}$ are to be suppressed by the phase cycling procedure. Pathways $\mathbf{p}^{(\pm 3)}$, $\mathbf{p}^{(\pm 4)}$ and so on, that involve coherence orders (± 3), (± 4) and higher, are not taken into account as they are usually difficult to excite in systems of spins-$\frac{1}{2}$. In the case of triply-labeled U-^{13}C-*L*-alanine (Fig. 6.6), the highest coherence order present in the system is (± 3) if intermolecular interactions are neglected.
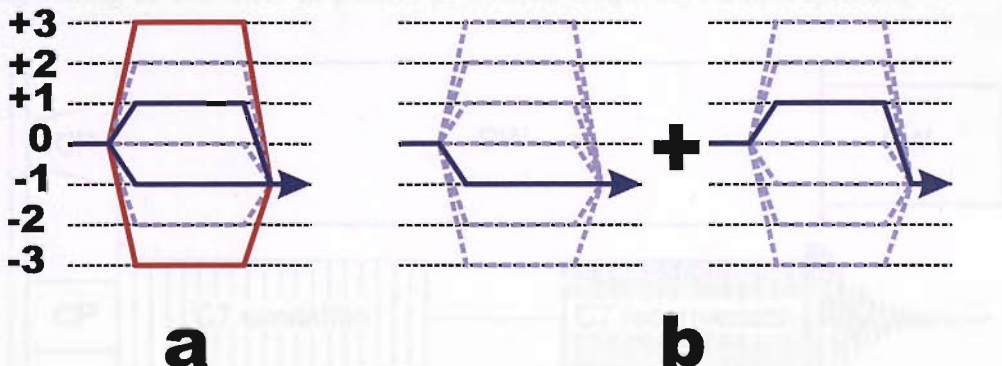

Figure 6.3: An example of a coherence pathway that cannot be selected by the conventional phase cycling procedure but can be by the multiplex phase cycling method. The set of coherence pathways $\mathbf{p}^{(\pm 1)} = (0 \to \pm 1 \to -1)$ (bold blue line) can not be selected by the conventional phase cycle if the triple-quantum coherence is present and important (*a*). If the multiplex phase cycling procedure is used instead, the pathways $\mathbf{p}^{(-p)} = (0 \to +1 \to -1)$ and $\mathbf{p}^{(-p)} = (0 \to -1 \to -1)$ can be selected separately, and all the other coherence pathways ($\mathbf{p}^{(0)}$, $\mathbf{p}^{(\pm 2)}$ and $\mathbf{p}^{(\pm 3)}$) can be suppressed (*b*).

Both pathways $\{0 \to \pm 2 \to -1\}$ are necessary to obtain a pure-absorption 2D spectrum. The set of desired coherence pathways $\mathbf{p}^{desired} = \{\mathbf{p}^{(+2)}, \mathbf{p}^{(-2)}\}$ may be selected by a 4-step phase cycle, according to Table. 6.1. The minimal number of transients per t_1 increment required for completing the phase cycle was 4, which, with the necessity to acquire both sine- and cosine-modulated signals, gives 8 cycle steps.

Using multiplex phase cycling with the phase values listed in Table. 6.2, five different signals, $s_1(t_1, t_2)$, $s_2(t_1, t_2)$, $s_3(t_1, t_2)$, $s_4(t_1, t_2)$ and $s_5(t_1, t_2)$, were acquired and stored separately. The further procedures are illustrated in Fig. 6.5. The numerical phase factors $\varphi_{num}^{(+2)}$ and $\varphi_{num}^{(-2)}$ by which these signals should be multiplied to select $(+2)$- and (-2)-coherence orders, are summarized in Table 6.3. Then the signals $s^{(+2)}(t_1, t_2)$ and $s^{(-2)}(t_1, t_2)$ were combined into cosine- and sine-modulated signals and treated according to the SHR method.

NMR spectra of 98% triply-labeled U-L-^{13}C-alanine (Fig. 6.6) were acquired on a Chemagnetics Infinity-200 NMR spectrometer at a static magnetic field $B_0 = 4.7$ T (corresponding to 200 MHz in proton precession frequency) and a spinning
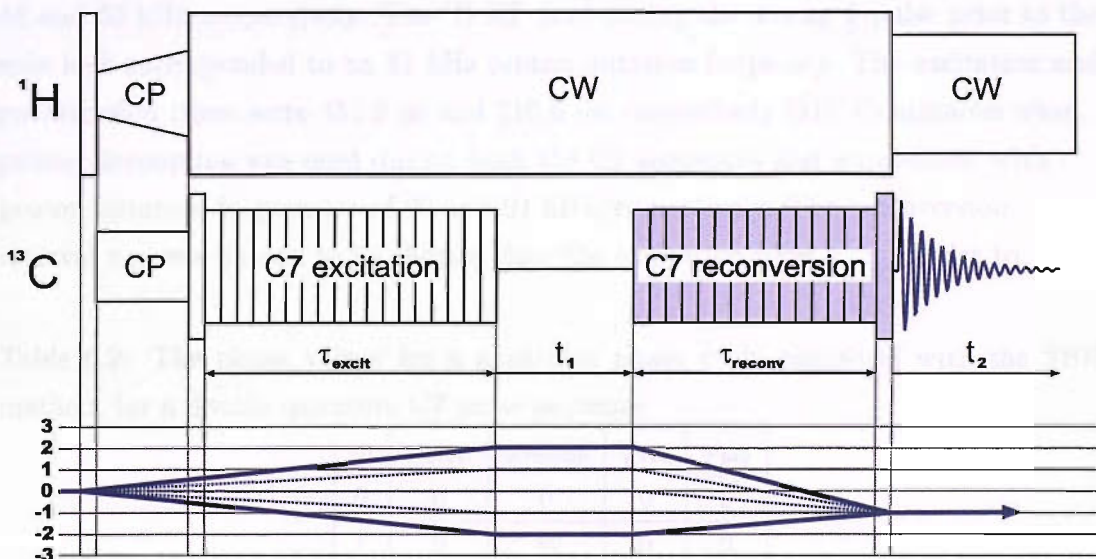

Figure 6.4: Pulse sequence for the double quantum 2D $C7$ recoupling pulse sequence. Both coherence pathways $\mathbf{p}^{(+2)}$ and $\mathbf{p}^{(+2)}$ have to be selected.

Table 6.1: The phase values for the conventional phase cycle combined with the SHR method, for a double-quantum C7 pulse sequence.

	m	φ_{excit}	φ_{reconv}	φ_{rec}	φ_{dig}
cos	0	0	0	0	0
cos	1	0	$\frac{2\pi}{4}$	0	$-\frac{2\pi}{4}$
cos	2	0	$2\frac{2\pi}{4}$	0	$-2\frac{2\pi}{4}$
cos	3	0	$3\frac{2\pi}{4}$	0	$-3\frac{2\pi}{4}$
sin	0	$-\frac{\pi}{4}$	0	0	0
sin	1	$-\frac{\pi}{4}$	$\frac{2\pi}{4}$	0	$-\frac{2\pi}{4}$
sin	2	$-\frac{\pi}{4}$	$2\frac{2\pi}{4}$	0	$-2\frac{2\pi}{4}$
sin	3	$-\frac{\pi}{4}$	$3\frac{2\pi}{4}$	0	$-3\frac{2\pi}{4}$

frequency of 9.5 kHz, using a 4 mm zircon rotor. The spectra were acquired using the pulse sequence in Fig. 6.4, using the C7 sequence for both excitation and reconversion of the double-quantum coherence. The contact time during cross-polarization was 850 μs, and ^{1}H and ^{13}C nutation frequencies during CP were 48 and 53 kHz, respectively. The ^{1}H RF field during the strong $\frac{\pi}{2}$-pulse prior to the spin lock corresponded to an 81 kHz proton nutation frequency. The excitation and reconversion times were 451.2 μs and 210.6 μs, respectively [51]. Continuous wave proton decoupling was used during both the C7 sequences and acquisition, with proton nutation frequencies of 99 and 91 kHz, respectively. The reconversion interval τ_{rec} was chosen to be shorter then the excitation time τ_{exc} in order to

Table 6.2: The phase values for a multiplex phase cycle combined with the SHR method, for a double-quantum C7 pulse sequence.

| m	φ_{excit}	φ_{reconv}	φ_{rec}	φ_{dig}
0	0	0	0	0
1	0	$\frac{2\pi}{5}$	0	0
2	0	$2\frac{2\pi}{5}$	0	0
3	0	$3\frac{2\pi}{5}$	0	0
4	0	$4\frac{2\pi}{5}$	0	0
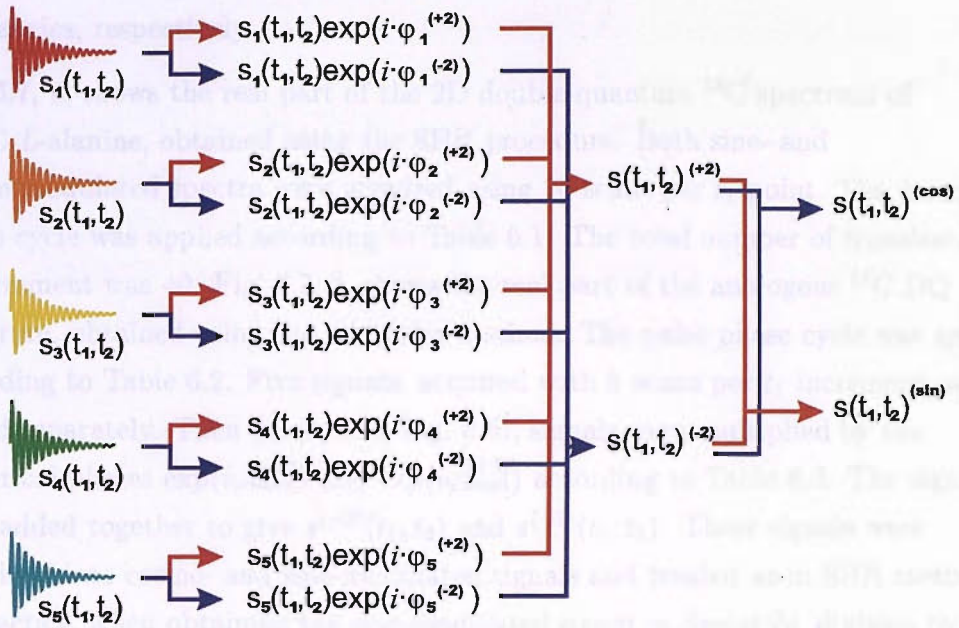
Figure 6.5: Schematic presentation of the DQ experiment using the multiplex phase cycling procedure. Five signals $s_1(t_1, t_2)$ - $s_5(t_1, t_2)$ are acquired and stored separately. Then, after the required phase factors have been applied to the signals, they are combined to generate amplitude-modulated signals.

eliminate indirect peaks [51]. The evolution interval t_1 was incremented in 128 steps with a duration of 83.3 μs each. The ^{13}C RF strength during the strong $\frac{\pi}{2}$ pulses and during the C7 sequences corresponded to 69.5 and 66.5 kHz ^{13}C nutation

Table 6.3: Numerical phase factors $\varphi_{num}^{(+2)}$ and $\varphi_{num}^{(-2)}$ that must be applied in order to select the $\mathbf{p}^{(+2)}$ and $\mathbf{p}^{(-2)}$ coherence pathway, respectively.

Signal	$\varphi_{num}^{(+2)}$	$\varphi_{num}^{(-2)}$
$s_1(t_1, t_2)$	0	0
$s_2(t_1, t_2)$	$3\frac{2\pi}{5}$	$-\frac{2\pi}{5}$
$s_3(t_1, t_2)$	$6\frac{2\pi}{5}$	$-2\frac{2\pi}{5}$
$s_4(t_1, t_2)$	$9\frac{2\pi}{5}$	$-3\frac{2\pi}{5}$
$s_5(t_1, t_2)$	$12\frac{2\pi}{5}$	$-4\frac{2\pi}{5}$

frequencies, respectively.

Fig. 6.7, a, shows the real part of the 2D double-quantum ^{13}C spectrum of
U-^{13}C-L-alanine, obtained using the SHR procedure. Both sine- and
cosine-modulated spectra were acquired using 20 scans per t_1 point. The 4-step
phase cycle was applied according to Table 6.1. The total number of transients per
t_1 increment was 40. Fig. 6.7, b, shows the real part of the analogous ^{13}C DQ
spectrum, obtained using the multiplex method. The pulse phase cycle was applied
according to Table 6.2. Five signals, acquired with 8 scans per t_1 increment, were
stored separately. Then (as seen in Fig. 6.5), signals were multiplied by the
numerical phases $\exp(i\varphi_{num}^{(-2)})$ and $\exp(i\varphi_{num}^{(+2)})$ according to Table 6.3. The signals
were added together to give $s^{(-2)}(t_1, t_2)$ and $s^{(+2)}(t_1, t_2)$. These signals were
combined into cosine- and sine-modulated signals and treated as in SHR method.
In practice, when obtaining the sine-modulated signal in *Spinsight*, division by i was
performed by phasing the respective signal by $\frac{\pi}{2}$.

Both spectra were acquired during an equal amount of time (11.4 h) and an equal
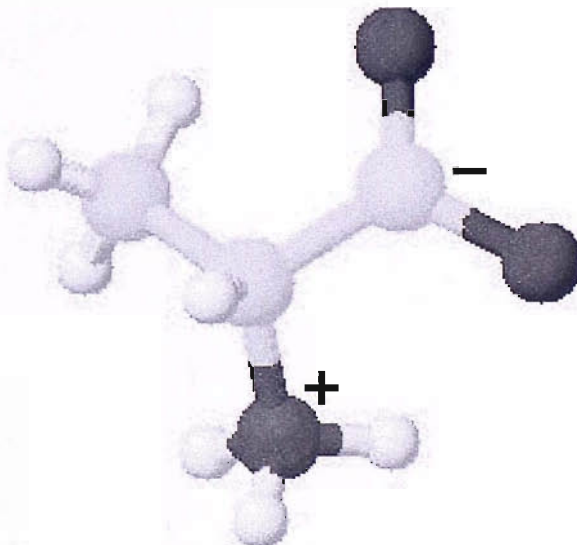
Figure 6.6: The chemical structure of a single molecule of the amino acid L-alanine.
In the crystalline form there is one molecule per unit cell. Color notation: blue –
nitrogen, green – carbon, white – hydrogen, red – oxygen.

number of scans per step in t_1 (40).The spectra show the equivalence of the results given by the two different methods. The signal-to-noise ratio is equal, and all the peak intensities are the same for the two spectra. The minimum number of transients per increment in the t_1 dimension is equal to 8 (2 h. 20 min.) in the case of the SHR method, while for the multiplex procedure it is 5 transients (1 h. 25 min). These are sufficient for selecting the desired coherence pathway and for obtaining spectra in pure-absorption mode.
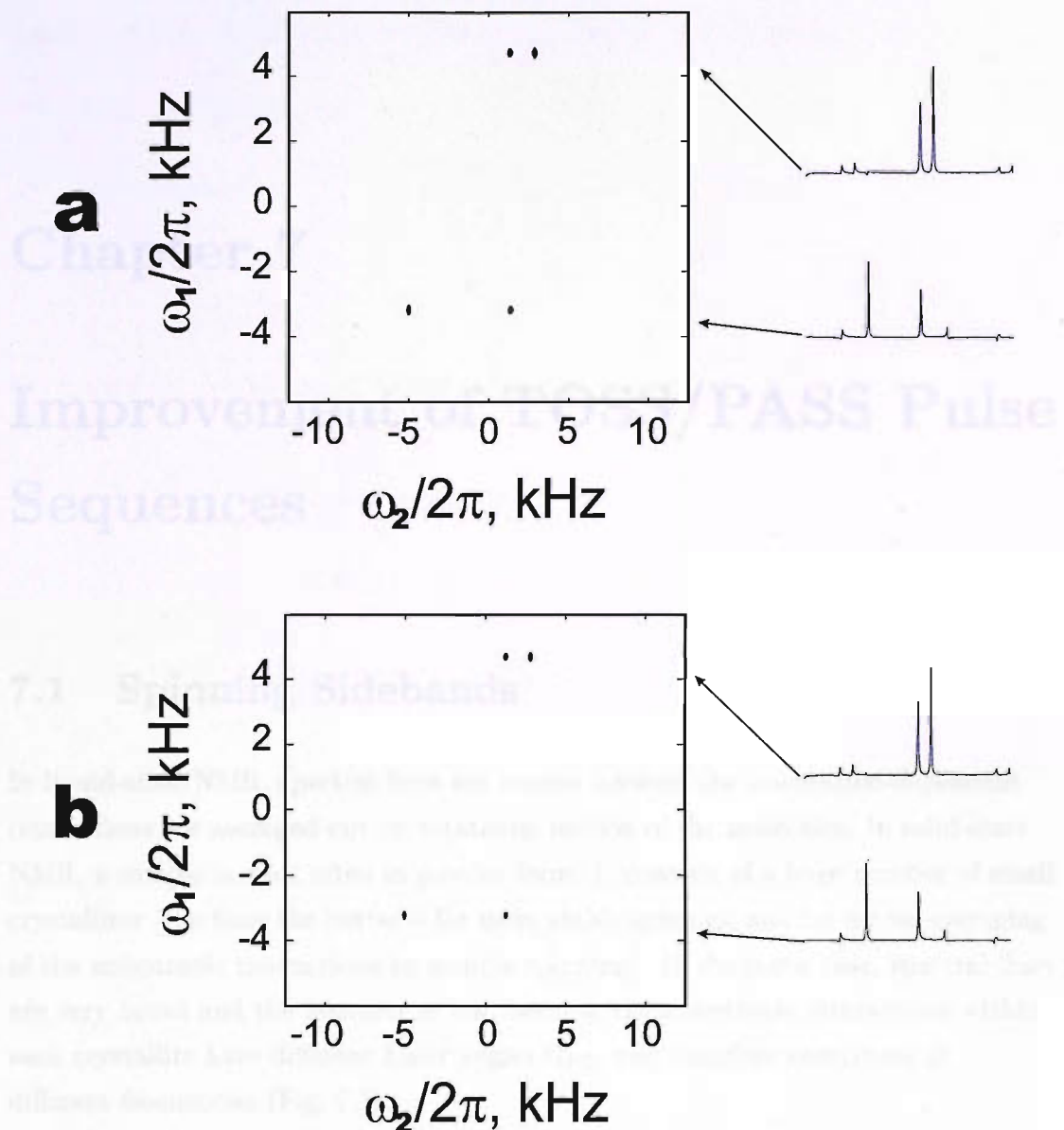
Figure 6.7: Pure absorption DQ spectra of polycrystalline U-^{13}C-L-alanine. Experiments were performed in a magnetic field of 4.7 T, at a spinning frequency of 9500 Hz. a, ^{13}C spectrum obtained using the SHR method. Sine- and cosine-modulated signals were obtained using the phase cycle shown in Table 6.1 with 20 transients per t_1 increment. b, ^{13}C spectrum was obtained using the multiplex procedure, with a 5-step phase cycle according to Table 6.2. Each signal was acquired with 8 transients per t_1 increment. The phase factors in Table 6.3 were applied to the signals and then treated as described above. As can be seen from the spectra, the signal-to-noise ratios are comparable.

Chapter 7

Improvement of TOSS/PASS Pulse Sequences

7.1 Spinning Sidebands

In liquid-state NMR, spectral lines are narrow because the orientation-dependent interactions are averaged out by rotational motion of the molecules. In solid-state NMR, a sample is most often in powder form. It consists of a huge number of small crystallites (the finer the better – for more stable spinning and for better averaging of the anisotropic interactions by sample spinning). In the static case, spectral lines are very broad and the intensity is low, because the anisotropic interactions within each crystallite have different Euler angles Ω_{PL}, and therefore contribute at different frequencies (Fig. 7.1).

Magic-angle spinning can average out the anisotropic interactions (except the second-order quadrupolar interaction) if the spinning speed is larger than the powder linewidth, (Fig. 7.2, a). Otherwise, so-called spinning sidebands appear in the spectrum at frequency $(\omega_{iso} + k\omega_r)$, where k is the order of a sideband ($k = 0$ for the centreband) (Fig. 7.2, b).

The presence of spinning sidebands can be explained as follows. For an isolated

94

spin-$\frac{1}{2}$, the spin Hamiltonian consists of the Zeeman and CS parts:

$$\widehat{\mathcal{H}}_{spin} = \widehat{\mathcal{H}}_Z + \widehat{\mathcal{H}}_{CS} = \tag{7.1}$$

$$\omega_0 \widehat{I}_z - \omega_0 \delta_{iso} \widehat{I}_z + \sum_{m=-2}^{+2} \sum_{m'=-2}^{+2} \Lambda_{2m'}^{(P)} D_{m'm}^{(2)}(\Omega_{PR}) D_{m0}^{(2)}(\Omega_{RL}(t)) \widehat{I}_z =$$

$$\left(\omega_{iso} + \sum_{m=-2}^{+2} \sum_{m'=-2}^{+2} \Lambda_{2m'}^{(P)} D_{m'm}^{(2)}(\Omega_{PR}) D_{m0}^{(2)}(\Omega_{RL}(t)) \right) \widehat{I}_z = \omega(\Omega_{PL}(t)) \widehat{I}_z$$

Here, the following notation is introduced:

$$\omega(\Omega_{PL}(t)) = \omega_{iso} + \sum_{m=-2}^{+2} \sum_{m'=-2}^{+2} \Lambda_{2m'}^{(P)} D_{m'm}^{(2)}(\Omega_{PR}) D_{m0}^{(2)}(\Omega_{RL}(t)) \tag{7.2}$$

$\omega(\Omega_{PL}(t))$ can also be written as the following sum

$$\omega(\Omega_{PL}(t)) = \sum_{m=-2}^{2} \omega^{(m)}(\Omega_{PR}) \exp(im\omega_r) \tag{7.3}$$

where the Fourier components $\omega^{(m)}(\Omega_{PR})$ are expressed as

$$\omega^{(m)}(\Omega_{PR}) = \sum_{m'=-2}^{2} A_{2m'}^{P} D_{m'm}^{(2)}(\Omega_{PR}) d_{m0}^{(2)}(\beta_{RL}) \exp(-im\alpha_{RL}^0) + \delta_{m0}\omega_{iso} \tag{7.4}$$

Here, δ_{m0} is the Kronecker symbol. The Fourier components have the following symmetry properties:
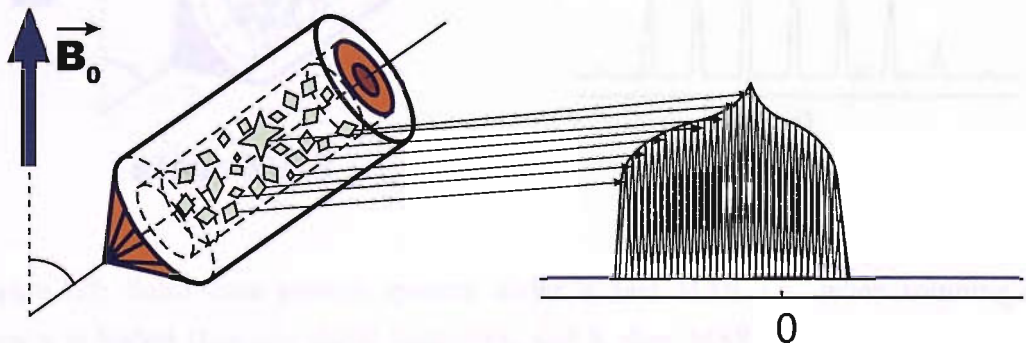

Figure 7.1: A broad spectral line produced by a static powder sample.

- $\omega^{(m)}(\Omega_{PR}) = (\omega^{(-m)}(\Omega_{PR})^*)$

- $\omega^{(m)}(\Omega_{PR}) = \omega^{(m)}(\alpha_{PR}, \beta_{PR}, 0) \exp(im\gamma_{PR})$

As can be seen from Eq. (7.3), CS frequency is modulated by the factor $\exp(im\omega_r)$ that explains the presence of the spinning sidebands.
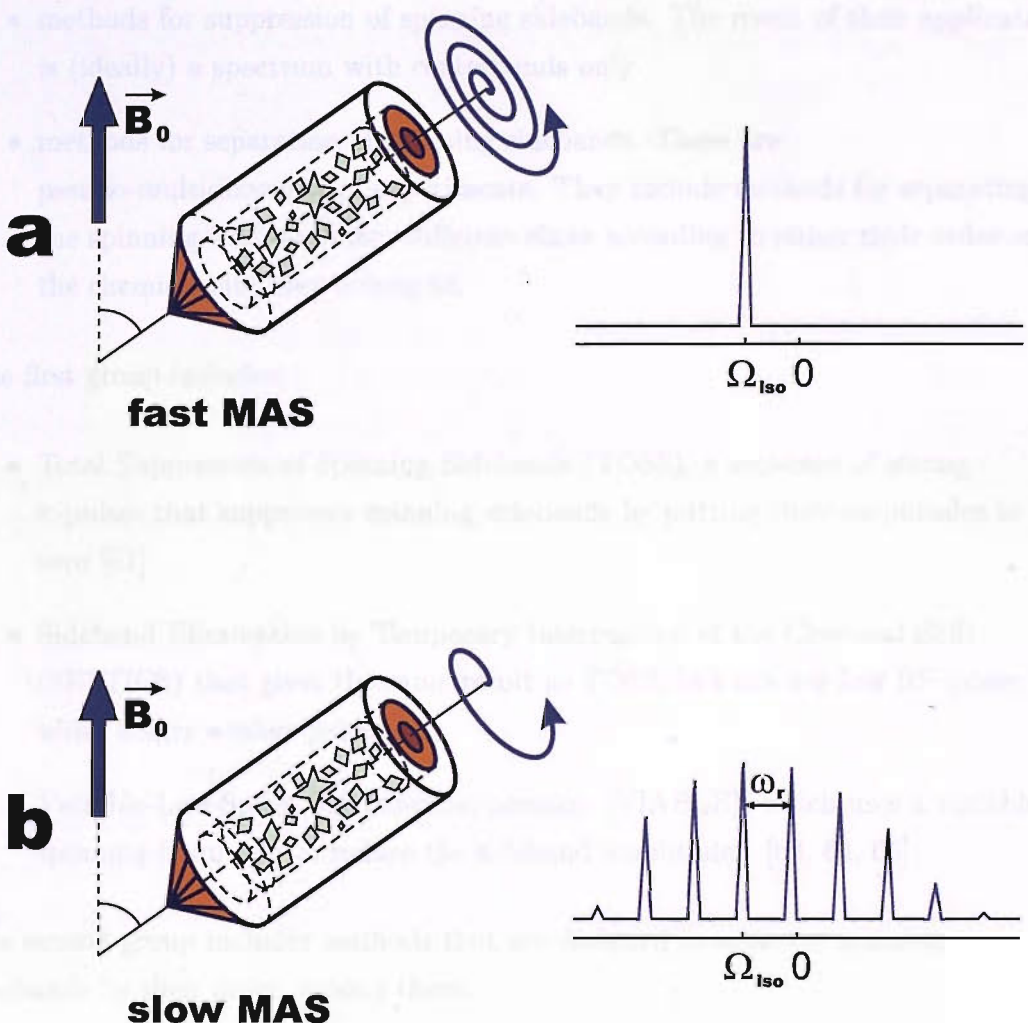

Figure 7.2: Solid-state powder spectra under a, fast MAS, i.e. when spinning frequency is higher then the static linewidth, and b, slow MAS.

7.2 Methods for Sideband Manipulation

There are a number of methods that have been designed for the manipulation of spinning sidebands. They can be divided into two groups, according to their effect on the sideband pattern:

- methods for suppression of spinning sidebands. The result of their application is (ideally) a spectrum with centerbands only

- methods for separation of spinning sidebands. These are pseudo-multidimensional experiments. They include methods for separating the spinning sidebands into different slices according to either their order or the chemical site they belong to.

The first group includes:

- Total Suppression of Spinning Sidebands (TOSS), a sequence of strong π-pulses that suppresses spinning sidebands by putting their amplitudes to zero [61]

- Sideband Elimination by Temporary Interruption of the Chemical Shift (SELTICS) that gives the same result as TOSS, but can use less RF power by using longer weaker pulses [62]

- Variable-Low-Speed Sideband Suppression (VIABLE), which uses a variable spinning frequency to reduce the sideband amplitudes [63, 64, 65]

The second group includes methods that are designed to separate spinning sidebands by their order, among them:

- Phase-Altered Separation of Sidebands (PASS) [66],

- Five π Replicated Magic Angle Turning (FIREMAT) [67, 68]

- Isotropic Rotation Sequence (IRS) [69]

7.3   Sideband Suppression

Often the presence of spinning sidebands is not desirable because they greatly complicate the peak assignment. If there are many sites present, the spinning .sidebands make the NMR spectrum very crowded. Therefore, there is a need for methods for sideband suppression.

TOSS was invented by Dixon [61]. Originally, it was a sequence of four π-pulses that occupied two rotation periods, applied after the CP sequence. Due to carefully designed timing of the pulses, the magnetization components are prepared in such a way that sidebands are suppressed. There have been many modifications of TOSS. Today, there are TOSS sequences with a number of pulses from four up to nine, with sequence durations between 0.72 and 4 rotation periods [70, 71, 72, 73, 74]. All of them can be designed using available theory and give more or less comparable results. One disadvantage of TOSS is that the centreband intensity does not correspond to the one obtained without TOSS at the same spinning frequency and may even be negative. In Fig. 7.3, the ^{13}C CP MAS spectra of 1-^{13}C-Glycine are presented, with and without TOSS (a and b, respectively).

7.3.1   Theory of TOSS

TOSS and PASS sequences consist of N π-pulses with carefully chosen timings [74] (Fig. 7.4). The duration of the TOSS/PASS sequence is denoted as T. If the start of acquisition is time point $t = 0$, then the TOSS/PASS sequence starts at $t = -T$. The π-pulses are situated at time-points $(-T + t_n)$. The beginning and the end of the nth pulse coincide at the time point $(-T + t_n)$, as the π-pulses are considered to be infinitely short. The TOSS/PASS sequence is applied to the spin system after the excitation of the transverse magnetization, prior to acquisition.

Using a traditional carousel picture [74] for describing TOSS, a rotating powder sample can be imagined to consist of a large number of carousels. Each carousel is a set of sites that have the same isotropic chemical shift and the same angles $(\alpha_{PR}, \beta_{PR})$. They have different angles $\gamma_{PR}(t)$ but pass though all of them during rotation.
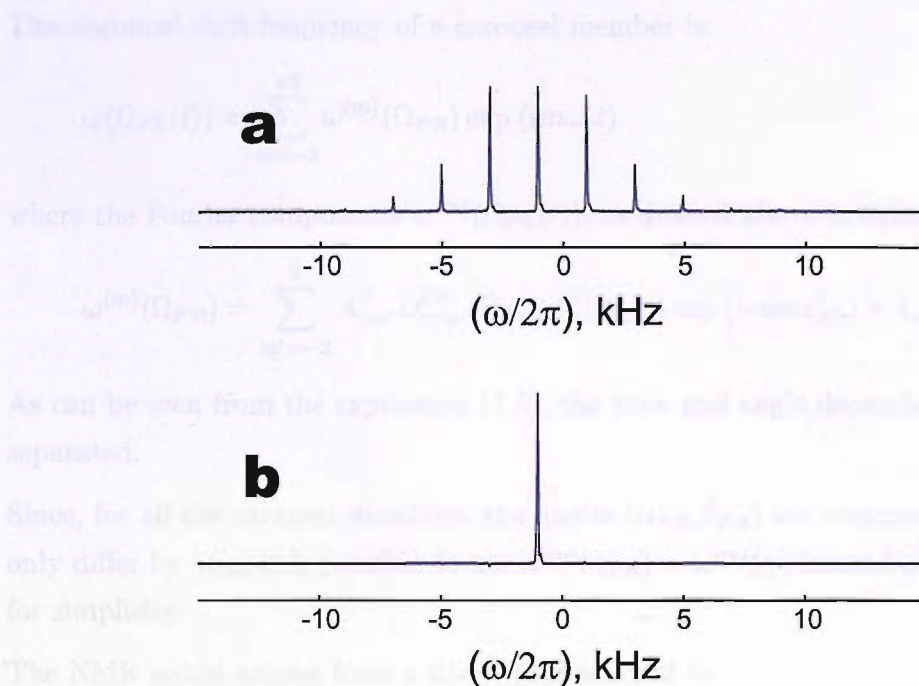
Figure 7.3: ^{13}C spectra of 1-^{13}C-Glycine (99%) at a spinning speed of 2 kHz; a, simple CP MAS and b, CP MAS followed by a TOSS sequence [72].
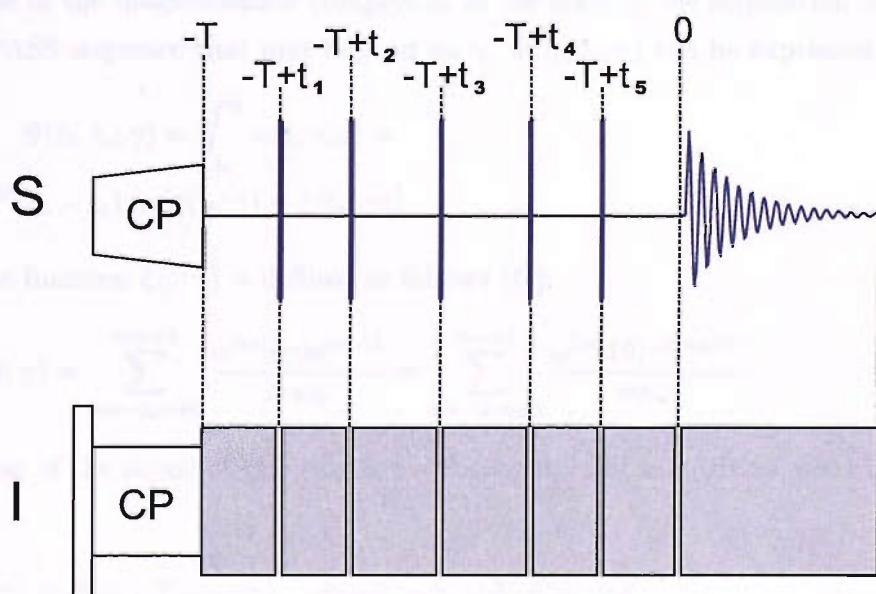

Figure 7.4: A TOSS pulse sequence consisting of $N = 5$ π-pulses.

The chemical shift frequency of a carousel member is:

$$\omega(\Omega_{PL}(t)) = \sum_{m=-2}^{+2} \omega^{(m)}(\Omega_{PR}) \exp\left(im\omega_r t\right) \tag{7.5}$$

where the Fourier components $\omega^{(m)}(\Omega_{PL}(t))$, as defined above in equation (7.4), are

$$\omega^{(m)}(\Omega_{PR}) = \sum_{m'=-2}^{2} A_{2m'}^P D_{m'm}^{(2)}(\Omega_{PR}) d_{m0}^{(2)}(\beta_{RL}) \exp\left(-im\alpha_{RL}^0\right) + \delta_{m0}\omega_{iso} \tag{7.6}$$

As can be seen from the expression (7.5), the time and angle dependences are separated.

Since, for all the carousel members, the angles $(\alpha_{PR}, \beta_{PR})$ are common and they only differ by γ_{PR}, it is possible to use $\omega^{(m)}(\gamma_{PR}) = \omega^{(m)}(\gamma)$ instead of $\omega^{(m)}(\Omega_{PR})$ for simplicity.

The NMR signal arising from a site is proportional to

$$s(t; \gamma) \propto \exp\left(i\Phi(t, 0; \gamma)\right) \exp\left(i\psi\right) \tag{7.7}$$

where $\Phi(t_b, t_a; \gamma)$ is a phase that is acquired during a period $\tau_{ba} = (t_b - t_a)$ and ψ is the phase of the magnetization component at the start of the acquisition in TOSS/PASS sequence that may depend on γ. $\Phi(t_b, t_a; \gamma)$ can be expressed as

$$\Phi(t_b, t_a; \gamma) = \int_{t_a}^{t_b} \omega(t; \gamma) dt = \tag{7.8}$$
$$\omega^{(0)}(t_b - t_a) + (\xi(t_b; \gamma) - \xi(t_a; \gamma))$$

Here, the function $\xi(t; \gamma)$ is defined as follows [74]:

$$\xi(t; \gamma) = \sum_{m=-2, m\neq 0}^{m=+2} \frac{\omega^{(m)}(\gamma) e^{im\omega_r t}}{im\omega_r} = \sum_{m=-2, m\neq 0}^{m=+2} \frac{\omega^{(m)}(0) e^{im\omega_r t + \gamma}}{im\omega_r} \tag{7.9}$$

The phase of the signal of this site at $t = 0$ (the start of acquisition, see Fig. 7.4) is equal to

$$\psi(\gamma) = \Phi(0, -T + t_5; \gamma) - \Phi(-T + t_5, -T + t_4; \gamma) + \tag{7.10}$$
$$\Phi(-T + t_4, -T + t_3; \gamma) - \Phi(-T + t_3, -T + t_2; \gamma) +$$
$$\Phi(-T + t_2, -T + t_1; \gamma) - \Phi(-T + t_1, -T; \gamma)$$

If the phase $\psi(\gamma)$ obeys the following condition:

$$\psi(\gamma) = \xi(0; \gamma) + \omega^{(0)}\tau_{seq} \tag{7.11}$$

$$\tau_{seq} = T + \sum_{n=1}^{5} t_n(-1)^n = 0$$

the intensity of all the sidebands except the centreband will be zero.

This can be shown in the following way. A function f is defined:

$$f(\gamma + \omega_r t) = \exp(i\xi(t; \gamma)) \tag{7.12}$$

Then, the signal of the site can be written as:

$$s(\gamma, t) = f(\gamma + \omega_r t)f^*(\gamma)\exp(i\psi)\exp(i\omega^{(0)}t) \tag{7.13}$$

It will now be shown that if the signal was just

$$s(\gamma + \omega_r t) = f(\gamma + \omega_r t)\exp(i\omega^{(0)}t) \tag{7.14}$$

i.e. if the following would be valid

$$f^*(\alpha, \beta, \gamma)\exp(i\psi) = 1 \tag{7.15}$$

all the sidebands would be suppressed.

The intensity of the sideband at $\omega^{(0)} + k\omega_r$ is given by Fourier transformation of the signal $s(t)$:

$$I_k(\gamma) = \int_0^{\tau_r} \frac{dt}{\tau_r}\exp(-ik\omega_r t)f(\alpha, \beta, \gamma + \omega_r t)\exp(i\psi(\gamma))f^*(\alpha, \beta, \gamma) =$$

$$f^*(\alpha, \beta, \gamma)\exp(i\psi(\gamma))\int_0^{2\pi} \frac{d\gamma'}{2\pi}f(\alpha, \beta, \gamma')\exp(-ik(\gamma' - \gamma)) =$$

$$f^*(\alpha, \beta, \gamma)\exp(i\psi(\gamma))\exp(ik\gamma)\int_0^{2\pi} \frac{d\gamma'}{2\pi}f(\alpha, \beta, \gamma')\exp(-ik\gamma') \tag{7.16}$$

The following notation has been introduced:

$$\gamma' \equiv \gamma + \omega_r t \tag{7.17}$$

Now, let us use notation:

$$F_k(\alpha, \beta) \equiv \int_0^{2\pi} \frac{d\gamma'}{2\pi} f(\alpha, \beta, \gamma') \exp(-ik\gamma') \tag{7.18}$$

Then,

$$I_k = f^*(\alpha, \beta, \gamma) \exp(i\psi(\gamma)) \exp(ik\gamma) F_k(\alpha, \beta) \tag{7.19}$$

For a powder sample, integration over the angles γ should be performed:

$$I_k = \int_0^{2\pi} \frac{d\gamma}{2\pi} f^*(\alpha, \beta, \gamma) \exp(i\psi(\gamma)) \exp(ik\gamma) F_k(\alpha, \beta) \tag{7.20}$$

When

$$f^*(\alpha, \beta, \gamma) \exp(i\psi(\gamma)) = 1 \tag{7.21}$$

the intensity of the kth sideband for a powder sample would be

$$I_k(\alpha, \beta) = \begin{cases} \int_0^{2\pi} \frac{d\gamma}{2\pi} F_k(\alpha, \beta) = F_k(\alpha, \beta)\frac{2\pi}{2\pi} = F_k(\alpha, \beta) & \text{if } k = 0 \\ = F_k(\alpha, \beta)\frac{1}{2\pi}(e^{ik2\pi} - e^{ik\cdot 0})\frac{1}{k} = 0 & \text{if } k \neq 0, \end{cases} \tag{7.22}$$

so that there is only one peak that corresponds to the isotropic frequency.

From expressions (7.11), five TOSS equations are derived:

$$F = 2\sum_{n=1}^5 e^{im\theta_n}(-1)^n + 1 = 0 \tag{7.23}$$

$$\theta_T + 2\sum_{n=1}^5 \theta_n(-1)^n = 0 \tag{7.24}$$

Here $\theta_n = \omega_r t_n$ and $\theta_T = \omega_r T$. In equation (7.23), four equations are comprised: this has to be true for real and imaginary parts for both $m = 1$ and $m = 2$. Solved simultaneously, the five equations above give the positions of the π-pulses, $\vec{\theta} = (\bar{\theta}_1, \bar{\theta}_2, \bar{\theta}_3, \bar{\theta}_4, \bar{\theta}_5)$, that obey the TOSS equations.

7.4 Methods for Sideband Separation

2D PASS (Phase-Altered Separation of Sidebands) [61] is, as well as TOSS, a sequence of strong π-pulses that is applied after the main sequence; the timings of the pulses are carefully chosen and vary with each t_1 step (see Fig. 7.5) so that the PASS equations (described later in this chapter) are satisfied, making a 2D experiment with sidebands that are separated by their order (see Fig. 7.6); after 2D-Fourier transformation all the central bands come to the same slice while the sidebands of order (± 1) appear in the two neighbouring slices and so on. In Fig. 7.6, a ^{13}C 2D PASS spectrum is shown, with spinning sidebands separated by order.

The FIREMAT (five π replicated magic angle turning) sequence [67, 68] is similar to PASS in the sense that the spinning sidebands are separated, but instead of separating sidebands by order, this method allows one to obtain spectra with the sideband pattern for each site separated by its isotropic chemical shift. The ^{13}C 2D FIREMAT spectrum of erythromycin-A, a molecule containing 36 carbon sites, is shown in Fig. 7.7 (adapted from [68]). In one dimension, peaks appear at their isotropic frequencies, in the other, the sideband pattern for each of the nuclear sites is produced.

There is one more method, called IRS (Isotropic Rotation Sequence) [69] that allows one to identify the sideband pattern coming from a particular site, by turning out-of-phase all the peaks coming from other sites.

7.4.1 Theory of PASS

In a similar way to the TOSS equations derivation, the following PASS equations are obtained:

$$F = 2 \sum_{n=1}^{5} e^{im\theta_n}(-1)^n + 1 + e^{im(\Theta + \theta_T)} = 0 \tag{7.25}$$

$$\theta_T + 2 \sum_{n=1}^{5} \theta_n (-1)^n = 0 \tag{7.26}$$

where Θ is the pitch of the PASS sequence, an additional phase that is acquired by the sidebands. The positions of the π-pulses depends on the pitch Θ. For the PASS
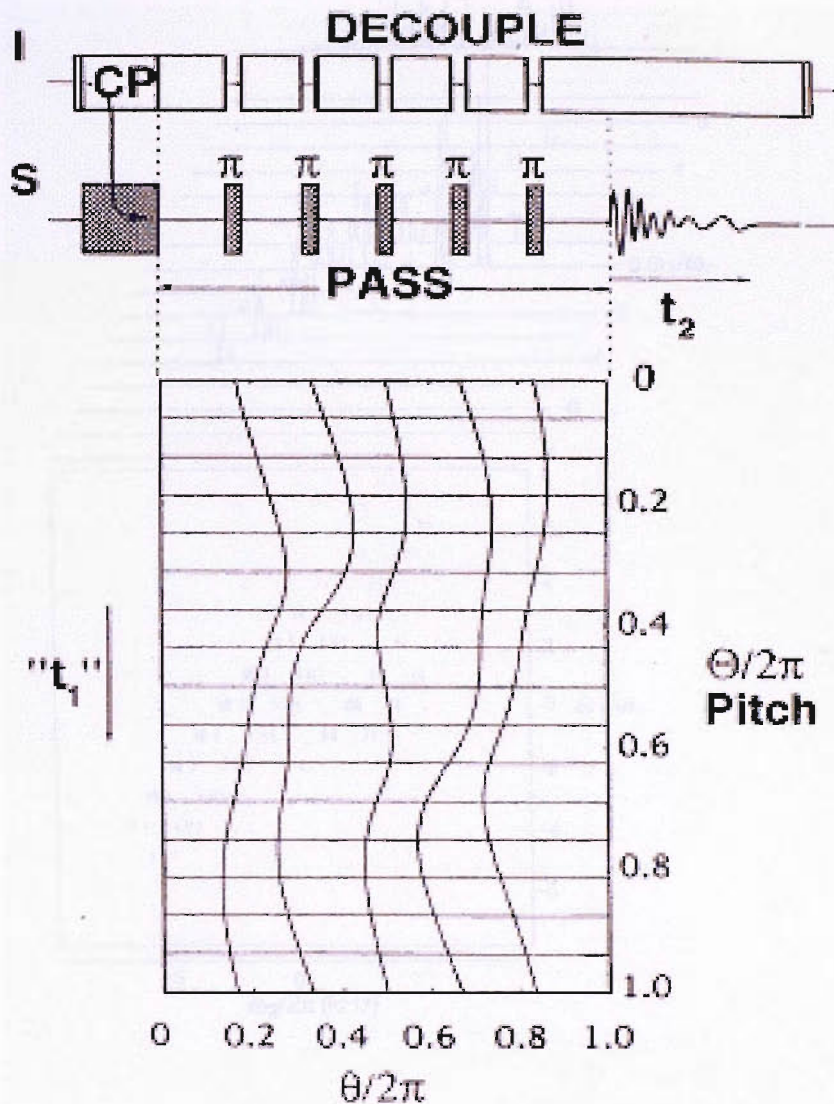

Figure 7.5: 2D PASS sequence for spinning sideband separation (from ref. [74]). Variation of the π-pulse timings along the trajectories shown creates the t_1-dimension.
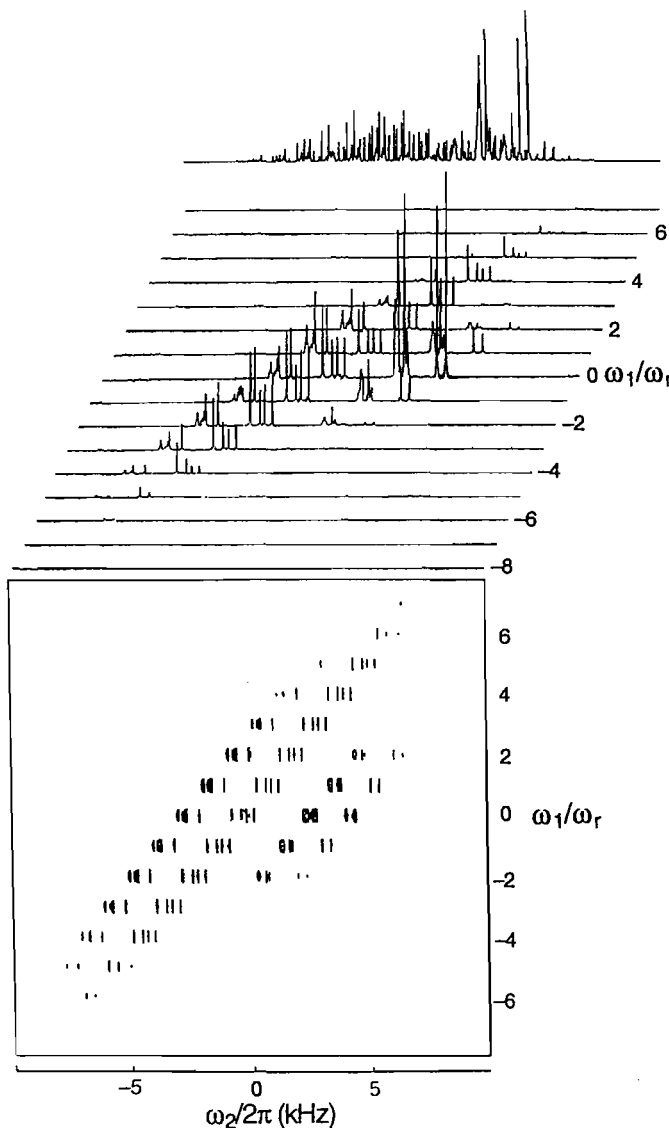
Figure 7.6: ^{13}C 2D PASS spectrum of penniciline-V powder at a spinning frequency 1.030 kHz and static magnetic field corresponding to a carbon-13 precession frequency of 50.3 MHz (adapted from [74]).

slice with pitch Θ, the kth sideband acquires the following phase shift

$$\phi_k = -k\Theta \tag{7.27}$$
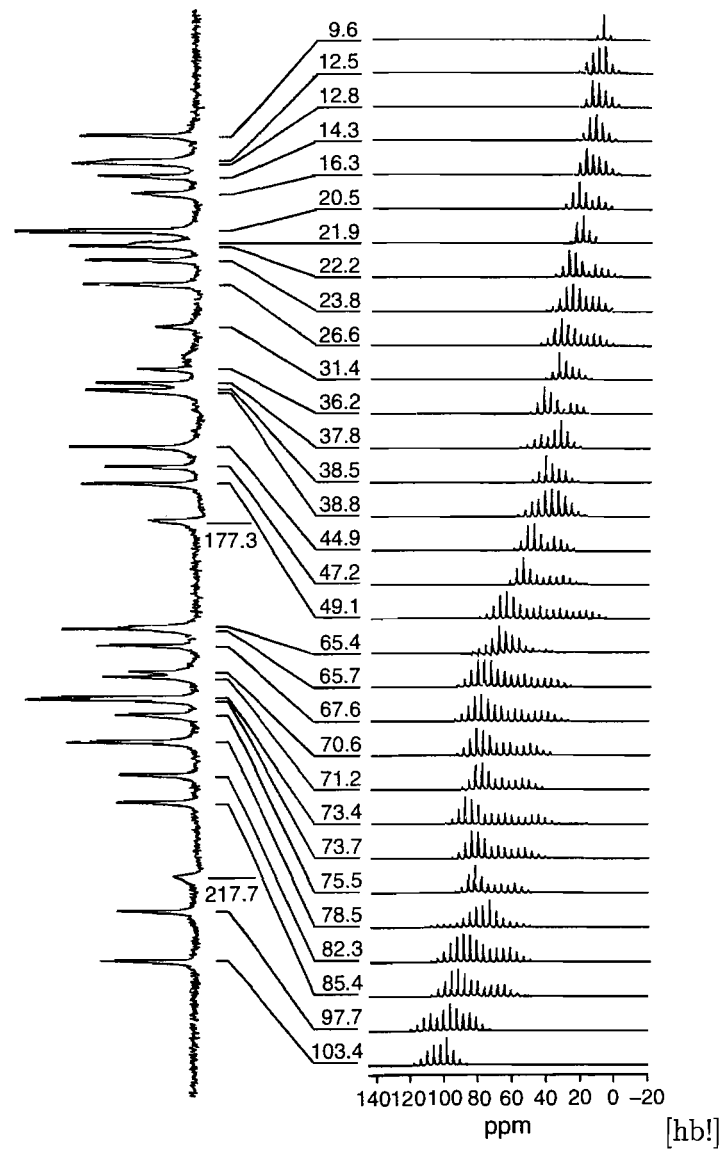
Figure 7.7: ^{13}C FIREMAT spectrum of Erythromycin-A at a spinning frequency of 0.5 kHz and static magnetic field corresponding to 400 MHz in proton frequency (adapted from [68]).

that results in the sidebands being separated by their orders. In the 2D PASS experiment, the pitch Θ varies in a two-dimensional data acquisition scheme (Fig. 7.5).

7.5   The π-Pulse Duration

The TOSS and PASS equations usually neglect the duration of the π-pulses. This assumption is reasonably valid if the pulses are very short compared to the rotation period. However, as the available rotation frequency has increased in magnitude, so has the necessity for faster spinning because of larger spectrometer fields. However, the available RF power has remained limited. Experimentally, at higher $\frac{\tau_p}{\tau_r}$ ratios the spinning sidebands are not ideally suppressed, and the situation deteriorates as this ratio increases. Therefore, it is necessary to take into account the pulse duration in the TOSS and PASS equations in order to improve the sideband suppression or separation.

If the pulse duration is $(2\Delta\theta)$, meaning that the qth pulse starts at time $(\theta_q - \Delta\theta)$ and ends at $(\theta_q + \Delta\theta)$, the TOSS equations (Eq. (7.23)) transform into the following [75]:

$$F' = \sum_{q=1}^{5}(\exp\left(im(\theta_q - \Delta\theta)\right) + \exp\left(im(\theta_q + \Delta\theta)\right))(-1)^q + 1 = 0 \qquad (7.28)$$

The fifth TOSS equation (Eq. 7.24) does not change.

For PASS, the equations change in a similar way:

$$F' = \sum_{q=1}^{5}(\exp\left(im(\theta_q - \Delta\theta)\right) + \exp\left(im(\theta_q + \Delta\theta)\right))(-1)^q + e^{im(\Theta+\theta_T)} = 0 \quad (7.29)$$

with the fifth PASS equation unchanged.

These equations can be either solved numerically for any given pulse duration $2\Delta\theta$, or solved approximately by means of expanding the equations with respect to the pulse duration, and retaining the linear part. As pulse duration relative to the rotor period depends on both the RF power and rotation frequency, the exact solutions

will only be valid for a specific set of these parameters. On the other hand, if the shifts of the pulse timings can be calculated algebraically given $\Delta\theta$, this can be implemented in the pulse program. In this case, the adjustment of the pulse timings will change automatically with RF power and/or rotation frequency.

7.5.1 Approximate Solution of Finite-Pulse TOSS/PASS Equations

Solutions of the TOSS/PASS equations with finite durations of the π-pulses $(\widetilde{\theta_1}, \ldots, \widetilde{\theta_N})$ differ somewhat from those for the original TOSS/PASS solutions $(\bar{\theta}_1, \ldots, \bar{\theta}_5)$. A new parameter ϵ_n can be introduced:

$$\varepsilon_n = \widetilde{\theta_n} - \bar{\theta}_n \tag{7.30}$$

Thus, there are two small parameters - $\Delta\theta$ and ϵ_q - that can be used for expansion. For small $\Delta\theta$, the exponent $e^{im(\theta_q \pm \Delta\theta)}$ can be expanded in a Taylor series. Keeping the terms up to second order in $\Delta\theta$, the approximation yields:

$$e^{im(\theta_q - \Delta\theta)} + e^{im(\theta_q + \Delta\theta)} = e^{im\theta_q}(e^{im(-\Delta\theta)} + e^{im(+\Delta\theta)}) = e^{im\theta_q}(2 - m^2\Delta\theta^2) \tag{7.31}$$

Thus, the function F' in TOSS equations can be approximated for small $\Delta\theta$:

$$F' = \sum_{q=1}^{5}(-1)^q(2 - m^2\Delta\theta^2)e^{im\theta_q} + 1 = \tag{7.32}$$

$$F - \sum_{q=1}^{5} m^2\Delta\theta^2(-1)^q e^{im\theta_q} = F + \delta F$$

As already mentioned above, roots of F' would be found close to those of F:

$$\widetilde{\theta_q} = \bar{\theta}_q + \epsilon_q \tag{7.33}$$

Expanding the function F' around zero values of F, and keeping only the first order terms in ϵ_q, we get:

$$F'(\widetilde{\theta_1}, \ldots) = F'(\bar{\theta}_1, \ldots) + \sum_{q=1}^{5} \frac{\partial F'(\bar{\theta}_1, \ldots)}{\partial\theta_q}\epsilon_q + \ldots \tag{7.34}$$

which can be further simplified to

$$F'(\widetilde{\theta_1}, \ldots) = F(\bar{\theta}_1, \ldots) + \delta F(\bar{\theta}_1, \ldots) + \sum_{q=1}^{5} \frac{\partial F(\bar{\theta}_1, \ldots)}{\partial \theta_q} \epsilon_q + \ldots \tag{7.35}$$

Here, terms with $\partial F'(\bar{\theta}_1, \ldots) \partial \theta_q$ are not included, as they will be of the next order in the expansion, containing $\Delta\theta^2 \epsilon$. Thus the simultaneous equations for ϵ_q can be written down:

$$-\sum_{q=1}^{5}(-1)^q m^2 \Delta\theta^2 e^{im\bar{\theta}_q} + \sum_{q=1}^{5}(-1)^q 2im e^{im\bar{\theta}_q} \epsilon_q = 0 \tag{7.36}$$

allowing calculation of the shift of the pulse positions that is needed to compensate for their non-zero length. From the fact that $\bar{\theta}_q$ are roots of F it follows that:

$$\sum_{q=1}^{5}(-1)^q e^{im\bar{\theta}_q} = \frac{1}{2} \tag{7.37}$$

This simplifies the equations for ϵ_q down to

$$\frac{1}{2}m\Delta\theta^2 + 2i \sum_{q=1}^{5}(-1)^q e^{im\bar{\theta}_q} \epsilon_q = 0 \tag{7.38}$$

or

$$2i \sum_{q=1}^{5}(-1)^q e^{im\bar{\theta}_q} \epsilon_q = -\frac{1}{2}m\Delta\theta^2 \tag{7.39}$$

These are the four equations. The fifth equation is given by the requirement on the total phase acquired during the evolution:

$$\theta_T + 2 \sum_{q=1}^{5}(-1)^q \theta_q = 0 \tag{7.40}$$

As it is satisfied for $\bar{\theta}_q$, the equation for ϵ_q should be reduced to

$$2 \sum_{q=1}^{5}(-1)^q \epsilon_q = 0 \tag{7.41}$$

Table 7.1: Positions of the π-pulses for TOSS-5, given in fractions of a rotation period τ_r.

Pulse number	Pulse position
1	0.2029
2	0.3258
3	0.5000
4	0.6742
5	0.7971

Thus, five equations for five values of ϵ are obtained in the form

$$A\vec{\epsilon} = \vec{b}\Delta\theta^2 \tag{7.42}$$

This means that the shifts of the π-pulses from the positions in an ideal TOSS sequence (with infinitely short pulses) are proportional to the square of the pulse length. The simultaneous linear equations above can be solved *exactly*, to give the proportionality factors.

For the specific case of the symmetric TOSS-5 sequence [76] occupying one rotor period with the π-pulse positions for ideal pulses according to Table 7.1, the system of the five simultaneous equations reduces to only two independent ones. Because of the symmetry of the sequence around its centre $\epsilon_3 = 0$ (the central pulse does not shift), $\epsilon_1 = -\epsilon_5$, $\epsilon_2 = -\epsilon_4$ (pulses shift symmetrically with respect to the centre of the TOSS-5 sequence, with the shift value depending on the π-pulse duration). Substituting the pulse positions in the ideal sequence $\bar{\theta}_1, ..., \bar{\theta}_1$ into the first equations of 7.42 the pulse shifts ϵ_1 and ϵ_2 are found:

$$\epsilon_1 = 0.0404\Delta\theta^2 \tag{7.43}$$
$$\epsilon_2 = 0.021\Delta\theta^2$$

Table 7.2: Positions of the π-pulse centres for TOSS-5, given in fractions of a rotation period τ_r, for ideal TOSS (column 1) and for the sequence adjusted for the finite π-pulse durations, in the case of $2\Delta\theta = 0.1\tau_r$ (columns 2 and 3, respectively).

Pulse number	Ideal TOSS pulse positions	Exact pulse positions	Approximate pulse positions
1	0.2029	0.1984	0.1990
2	0.3258	0.3233	0.3237
3	0.5000	0.5000	0.5000
4	0.6742	0.6767	0.6763
5	0.7971	0.8016	0.8010

7.6 Experimental Results

In *Appendix A*, a part of the pulse program for the symmetrical TOSS-5 sequence, corrected for finite pulse durations, is shown.

Experimental ^{31}P spectra of ammonium hypophosphite ($NH_4H_2PO_2$) are shown in Fig. 7.8. The spectra were acquired at a spinning frequency of 7000 Hz and static magnetic field of 9.4 T. The duration of the π-pulse was 14.2 μs, corresponding to $0.1\tau_r$. For the spinning sideband suppression, the TOSS-5 sequence was used, with values for the ideal TOSS (i.e. with infinitely short pulses) according to Table 7.1, and for the TOSS-5 adjusted according to Table 7.2.

This sample has a large CSA (about 50 ppm) providing spinning sidebands at a relatively high rotation frequency (Fig. 7.8, *b*). Fig. 7.8, *c* and *d*, present ^{31}P spectra of $NH_4H_2PO_2$ acquired by applying CP followed by a TOSS pulse sequence. At the spinning frequency of 7 kHz, the 14 μs-long π-pulse occupyies $0.1\tau_r$. Comparison of *c* and *d* shows the improvement of the sequence performance.

In Fig. 7.9, two ^{31}P TOSS spectra of the ammonium hypophosphite are shown. In both cases, the positions of the π-pulses in the TOSS sequence are adjusted (with respect to the ideal TOSS timings, given in the first column of Table 7.2) for the finite π-pulse duration: in Fig. 7.9, *a*, the exact solutions of the TOSS equations with finite pulse length of 0.1 τ_r were used (given explicitly in the second column of

Table 7.2), and in Fig. 7.9, (b), – the approximate ones, calculated using equation
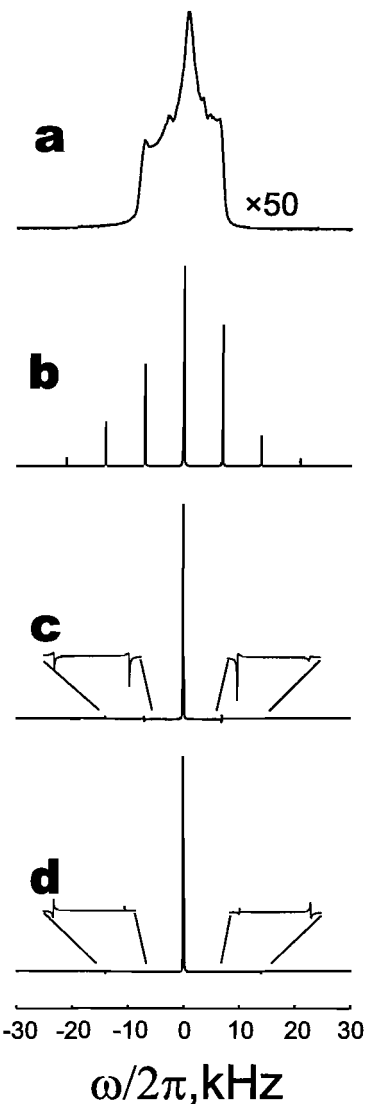
Figure 7.8: ^{31}P spectra of $NH_4H_2PO_2$ (ammonium hypophosphite). a, the static spectrum ($\times 50$). In b, c and d, MAS spectra are shown at the same vertical scale. b, a simple CP spectrum, c, a spectrum where CP is followed by a standard TOSS-5 prior the acquisition, d, a spectrum where the TOSS sequence used is compensated for the final π-pulse duration (that was equal to 14.2 μs, or $0.1\tau_r$). During all MAS experiments the rotation frequency was 7 kHz, the static magnetic field was 9.4 T.

(7.43) (given in the third column of Table 7.2). The performance of both sequences is practically undistinguishable, i.e. the approximation is good enough to use experimentally.
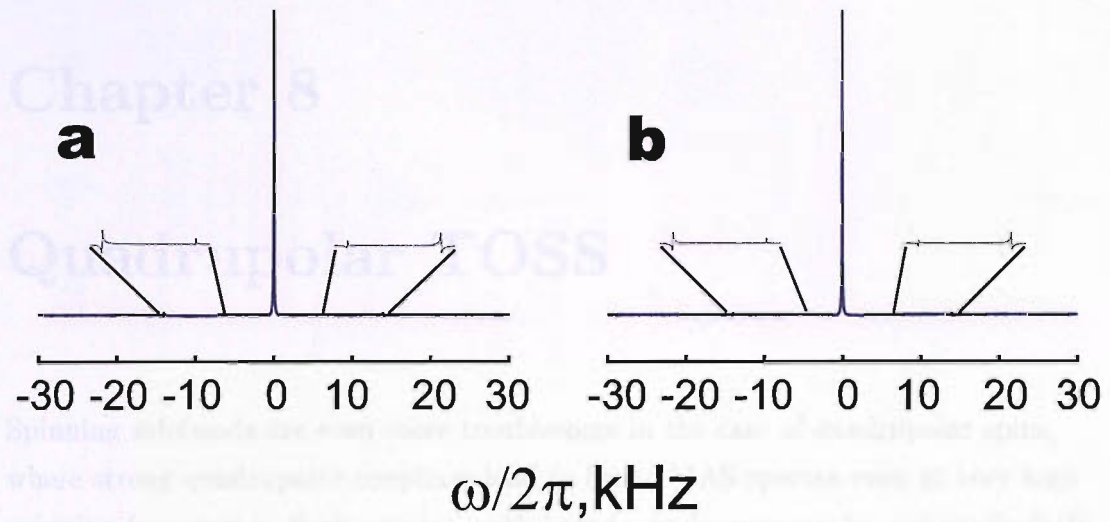

Figure 7.9: ^{31}P TOSS spectra of $NH_4H_2PO_2$ (ammonium hypophosphite). (a) and (b) TOSS pulse sequences that take into account the π-pulse duration exactly and approximately, respectively. The experimental conditions are the same as in Fig. 7.8.

At slower spinning frequencies, there is a smaller difference between the performance of the ideal TOSS sequence and the one that takes the finite π-pulse duration into account.

The 2D PASS experiment can be modified in a similar way, to compensate it for the finite pulse durations. As a PASS experiment cannot be symmetric, five different coefficients ($\epsilon_1, \ldots, \epsilon_5$) have to be calculated for each of the 16 slices.

Chapter 8

Quadrupolar TOSS

Spinning sidebands are even more troublesome in the case of quadrupolar spins, where strong quadrupolar couplings lead to broad MAS spectra even at very high spinning frequencies. Such spectra, with broad, overlapping peaks, are particularly difficult to analyze.

8.1 Sideband Suppression for Half-Integer Quadrupolar Nuclei

Because the quadrupolar frequency ω_Q is modulated by the spinning frequency, ω_r, spinning sidebands occur under MAS. These may overlap, and the information that can be extracted from the powder lineshape (the quadrupolar coupling constant and the asymmetry parameter) is then obscured.

Suppression of the spinning sidebands for quadrupolar nuclei can be achieved by applying a sequence of N π-pulses prior to signal acquisition [70, 77]. The positions $\theta_n = \omega_r t_n$ of the pulses must satisfy the following equations:

$$F = 2\sum_{n=1}^{9} e^{im\theta_n} - 1 = 0 \tag{8.1}$$

$$\theta_T + 2\sum_{n=1}^{9} \theta_n(-1)^n = 0 \tag{8.2}$$
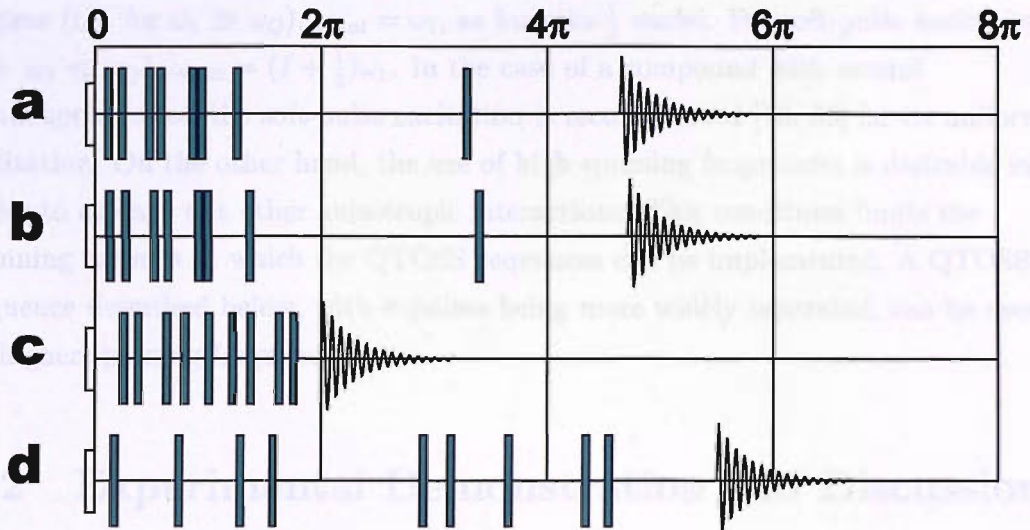
Figure 8.1: Collection of four existing QTOSS pulse sequences (QTOSS pulses are shown in cyan). QTOSS sequences, shown in a and b, have been described in [70] and the one in c – in [77]. The QTOSS sequence shown in d has larger separation between the π-pulses then the other three.

where $m = 1, \ldots, 4$ (in the case of spins-$\frac{1}{2}$, TOSS equations are similar, with $m = 1, 2$). Quadrupolar TOSS (QTOSS) pulse sequences for sideband suppression in quadrupolar samples have been described [70, 77]. The minimal number N of π-pulses that are required in order for the system of nine equations (8.1-8.2) is nine. (In fact, the first two QTOSS pulse sequences [70] consisted of eight π-pulses only, since Eq. (8.2) was ignored). Today, there are three QTOSS pulse sequences (see Fig. 8.1, a-c). The durations of these sequences are 2.32202 τ_r, 2.35294 τ_r and 1 τ_r, respectively, with τ_r being a rotor period.

The first two of these sequences, shown in Fig. 8.1, a and b, can only be used in a limited spinning regime as the minimal distance between the centres of two subsequent π-pulses is very short: 0.03472 and 0.03671 τ_r, respectively. For the sequence shown in Fig. 8.1, c, the minimal distance between the π-pulses is larger: 0.0649 τ_r.

In contrast to spins-$\frac{1}{2}$, the nutation frequency of the quadrupolar spins ω_{nut} depends on the RF field strength applied, $\omega_1 = \frac{1}{2}\gamma_I B_{RF}$. For the hard-pulse excitation

regime (i.e. for $\omega_1 \gg \omega_Q$), $\omega_{nut} = \omega_1$, as for spin-$\frac{1}{2}$ nuclei. For soft-pulse excitation (i.e. $\omega_1 \ll \omega_Q$), $\omega_{nut} = (I + \frac{1}{2})\omega_1$. In the case of a compound with several quadrupolar sites, the soft-pulse excitation is recommended [78, 33] for its uniform excitation. On the other hand, the use of high spinning frequencies is desirable in order to average out other anisotropic interactions. This conditions limits the spinning regimes at which the QTOSS sequences can be implemented. A QTOSS sequence described below, with π-pulses being more widely separated, can be used at higher spinning frequencies.

8.2   Experimental Demonstration and Discussion

Solutions of the equations (8.1,8.2) can be found numerically, for example in FORTRAN. For a fixed τ_T, the pulse positions $\tau_1, \ldots, \tau_9$ are found by the fastest descent method. As the sequence duration τ_T gets incremented and new solutions are found, the minimal distance between the π-pulses is computed. For $T = 2.75\tau_r$, the least distance between the π-pulses is $0.099\tau_r$ and such a sequence will tolerate relatively high spinning frequencies. The pulse positions for QTOSS are shown in the Table 8.1. This QTOSS differs from the published ones [70, 77] by a larger separation of the π-pulses. Therefore the QTOSS described in the Table 8.1 can be used at higher spinning frequencies without the pulses colliding.

^{27}Al NMR of aluminium acetylacetonate, $Al(CH_3COCHCOCH_3)_3$ (see Fig.9.5 in Chapter 9 for structural formula) was used for the experimental demonstration. In Fig. 8.2, a and b, two experimental [27]Al spectra are shown that were acquired at a spinning frequency of 1100 Hz and a static magnetic field of 7.05 T. In a, a MAS spectrum is shown, with many overlapping spinning sidebands. In b, the QTOSS sequence with the positions of the π-pulses as in Table 8.1 was applied before the signal acquisition; all the sidebands are suppressed. In Fig. 8.2 c and d, two spectra simulated in SIMPSON [10] are shown, at conditions that repeat the experimental ones, and with the parameters of the quadrupolar interactions (χ=3 MHz and η=0.0) described in [79] (here, χ is the quadrupolar coupling constant: $\chi = \frac{e^2qQ}{h}$). An example of SIMPSON input file for the quadrupolar TOSS is given in *Appendix B*. The π-pulse duration in the QTOSS pulse sequence was 22 μs.

Table 8.1: Positions of the π-pulses for QTOSS, given in fractions of a rotation period τ_r. QTOSS occupies $2.75\tau_r$.

| Pulse number	Pulse position
1	0.0869
2	0.3719
3	0.6397
4	0.7850
5	1.4532
6	1.5767
7	1.8297
8	2.1694
9	2.2684
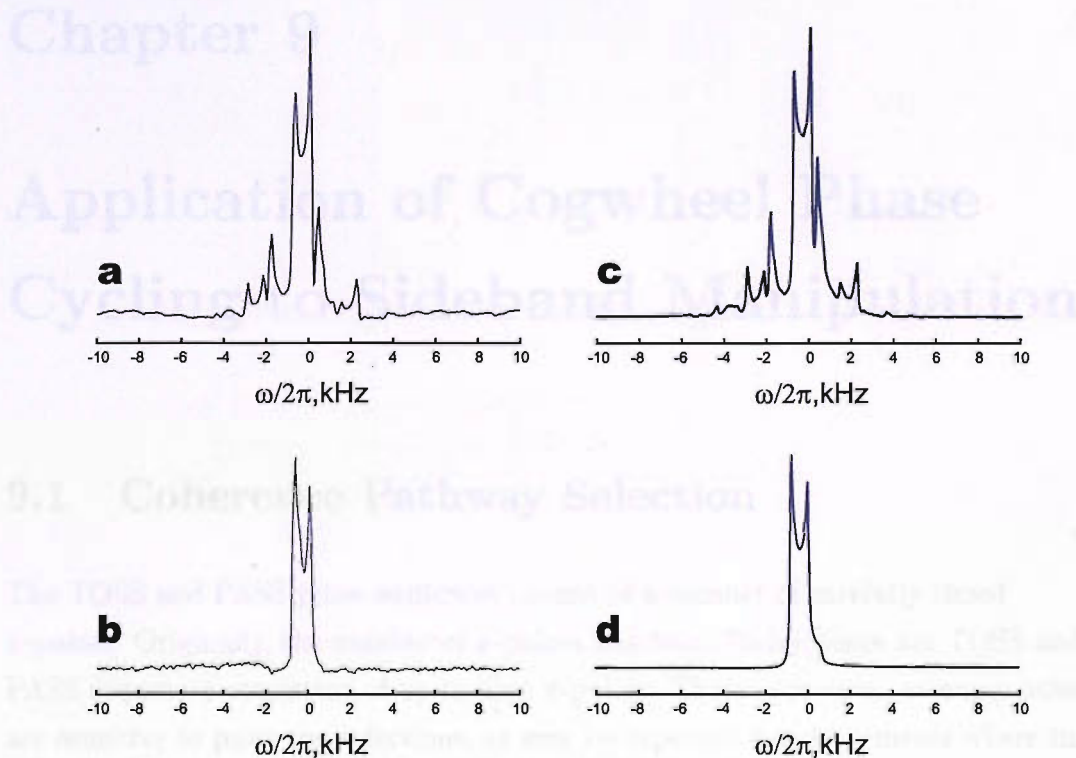
Figure 8.2: a and b, experimental ^{27}Al spectra of aluminium acetylacetonate. In a, the spectrum is acquired after applying a $\frac{\pi}{2}$-pulse, and in b, the QTOSS sequence with the positions of the π-pulses according to the Table 8.1. Both spectra have been obtained at a spinning frequency of 1100 Hz and a static magnetic field of 7.05 T. The π-pulse duration during the QTOSS sequence was 22 μs. c and d present the corresponding SIMPSON-simulated spectra (at the same experimental conditions).

Chapter 9

Application of Cogwheel Phase Cycling to Sideband Manipulation

9.1 Coherence Pathway Selection

The TOSS and PASS pulse sequences consist of a number of carefully timed π-pulses. Originally, the number of π-pulses was four. Today, there are TOSS and PASS sequences consisting of up to nine π-pulses. These sequences, as many others, are sensitive to pulse imperfections, as may be expected for experiments where the phase of the transverse magnetization must be controlled. Imperfect π-pulses lead to coherence transfer between all possible coherence orders in the spin system. This, in turn, leads to imperfect suppression (for TOSS) or separation (in the case of PASS) of the spinning sidebands. This problem is usually dealt with by applying a phase cycle (see *Section* 5.5).

For a system of isolated spins-$\frac{1}{2}$, the only significant coherence orders are $0, \pm1$. In order to select a coherence pathway $\{0 \to +1 \to -1 \to \ldots \to -1\}$ (for odd number of pulses N) or $\{0 \to -1 \to +1 \to \ldots \to -1\}$ (for even N) using the conventional phase cycling procedure, each of the pulses has to be cycled in 3 steps. Therefore, for a sequence of N pulses, the total number of the phase cycle steps is $\mathcal{M} = 3^N$. Popular modifications of TOSS and PASS sequences consist of five π-pulses, therefore a $3^5 = 243$-step phase cycle is traditionally used and every π-pulse is

cycled. It is possible to cut down the number of steps if the phase cycle is applied not to every pulse but only to every second one [80] (see Fig. 9.1) and select the desired CTP with a 75-step phase cycle.
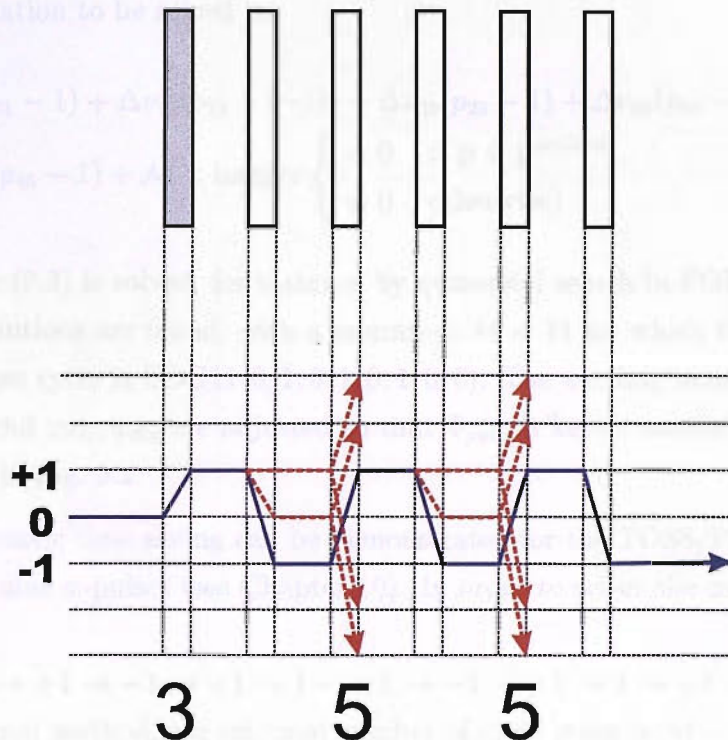

Figure 9.1: Selection of the coherence pathway $\{0 \to +1 \to -1 \to +1 \to -1 \to +1 \to -1\}$ by a 75-step cycle; every other pulse only is cycled. Grey marks a pulse block that initiates the $(+1)$-order coherence. Solid line indicates the desired coherence pathway, dashed lines indicate other coherence pathays that do not survive the phase cycle.

Cogwheel phase cycling can reduce the number of necessary cycle steps even more. For the TOSS/PASS sequence consisting of five π-pulses, the desired change in the coherence order is as follows:

$$\Delta p_0^{desired} = +1 \tag{9.1}$$
$$\Delta p_1^{desired}, \Delta p_3^{desired}, \Delta p_5^{desired} = -2$$
$$\Delta p_2^{desired}, \Delta p_4^{desired} = +2$$

where $\Delta p_0^{desired}$ is the coherence order change caused by the preparation pulse that excites $(+1)$-order (this is usually CP). The coherence orders between the pulses are: $p_{01}^{desired} = p_{23}^{desired} = p_{45}^{desired} = +1$, $p_{12}^{desired} = p_{34}^{desired} = -1$. Therefore, the cogwheel equation to be solved is:

$$\Delta\nu_{01}(p_{01} - 1) + \Delta\nu_{12}(p_{12} - (-1)) + \Delta\nu_{23}(p_{23} - 1) + \Delta\nu_{34}(p_{34} - (-1)) \quad (9.2)$$

$$+\Delta\nu_{45}(p_{45} - 1) + \mathcal{M} \times \text{integer} \begin{cases} = 0 & \text{if } \mathbf{p} \in \mathbf{p}^{desired}) \\ \neq 0 & \text{otherwise}) \end{cases}$$

The equation (9.2) is solved, for instance by numerical search in FORTRAN, and a number of solutions are found, with a minimum $\mathcal{M} = 11$ for which the suitable cogwheel phase cycle is $\text{COG}11(0, 1, 0, 1, 0, 1; 0, 6)$. The winding numbers are found numerically and $\varphi_{rec}, \varphi_{dig}$ are adjusted so that Φ_{path} is kept constant. This solution is illustrated in Fig. 9.2.

Even more drastic time saving can be demonstrated for the TOSS/PASS sequences consisting of nine π-pulses (see Chapter 10). In order to select the coherence pathway
$\mathbf{p}^{desired} = \{0 \rightarrow +1 \rightarrow -1 \rightarrow +1 \rightarrow 1 \rightarrow +1 \rightarrow -1 \rightarrow +1 \rightarrow 1 \rightarrow +1 \rightarrow -1\}$ using the conventional method, the minimal number of cycle steps is $\mathcal{M} = 3^9 = 19683$. Reduced cycle (i.e. with only every second π-pulse being cycled) requires $\mathcal{M} = 3 \cdot 5^4 = 1875$ phase cycle steps. Using the cogwheel phase cycling procedure, it is possible to select the desired phase cycle with 19 steps only.

9.2 Experimental Demonstration

9.2.1 Sideband Suppression for Spins-$\frac{1}{2}$

Experimental ^{1}H-decoupled ^{13}C-spectra of 99% labelled powdered $[1\text{-}^{13}C]$-Glycine are shown in Fig. 9.3. The spectra were obtained at a spinning frequency of 2900 Hz and a static magnetic field of 7.05 T, using the TOSS-5 pulse sequence [76]. In Fig. 9.3, a, CP-MAS sequence is used, and the sidebands are present. In Fig. 9.3, b, c and d, the TOSS-5 sequence has been applied after CP in order to suppress the

spinning sidebands: without the phase cycle, with the conventional phase cycle and with the cogwheel phase cycle, respectively.

In the spectrum in Fig. 9.3, b, the amplitudes of the spinning sidebands are significantly reduced. They are not perfectly suppressed, however, because of the π-pulse imperfections. Fig. 9.3, c and d show spectra with about the same sideband suppression performance. In the case of a conventional phase cycle, a minimum of 75 transients is required, compared to 11 scans for the cogwheel cycle.
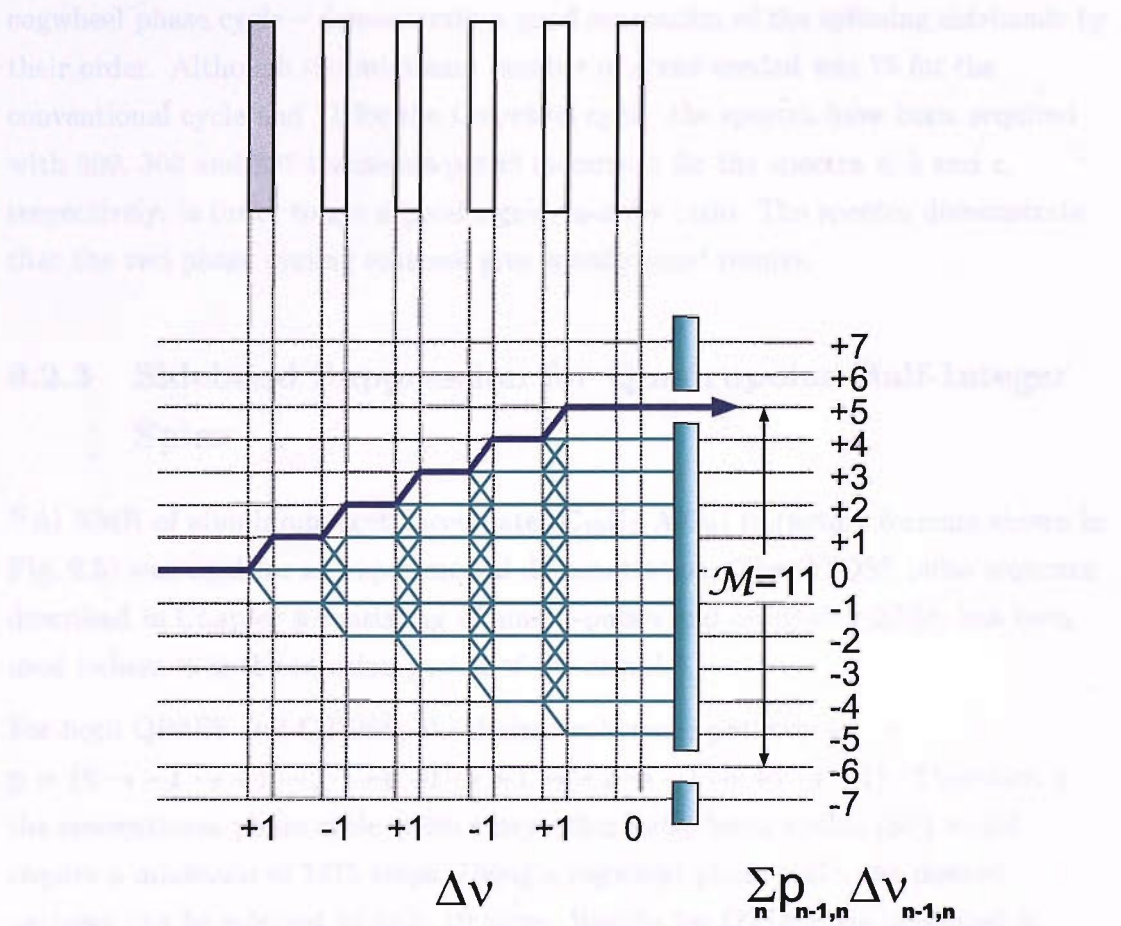

Figure 9.2: Cogwheel diagram for the cogwheel phase cycle COG11(0, 1, 0, 1, 0, 1; 0, 6). The desired coherence pathway $p_{desired} = \{0 \rightarrow +1 \rightarrow -1 \rightarrow +1 \rightarrow 1 \rightarrow +1 \rightarrow -1\}$ is shown as a bold line.

9.2.2 Sideband Separation for Spins-$\frac{1}{2}$

Experimental ^{13}C-spectra of powdered *L*-tyrosine hydrochloride with natural
abundance of ^{13}C are shown in Fig. 9.4. The spectra were obtained using the 2D
PASS pulse sequence [66], at a spinning frequency of 1750 Hz and a static magnetic
field of 7.05 T. The flip-angle of the π-pulses was deliberately misset to 0.78π. In
Fig. 9.4, *a*, where no phase cycle was used, there is imperfect separation of the
spinning sidebands. *b* – with the conventional phase cycle, and *c* – with the
cogwheel phase cycle – demonstrate a good separation of the spinning sidebands by
their order. Although the minimum number of scans needed was 75 for the
conventional cycle and 11 for the Cogwheel cycle, the spectra have been acquired
with 300, 300 and 297 transients per Θ increment for the spectra *a*, *b* and *c*,
respectively, in order to get a good signal-to-noise ratio. The spectra demonstrate
that the two phase cycling schemes give equally good results.

9.2.3 Sideband Suppression for Quadrupolar Half-Integer Spins

^{27}Al NMR of aluminium acetylacetonate ($C_{15}H_{21}AlO_6$) (structure formula shown in
Fig. 9.5) was used for an experimental demonstration. The QTOSS pulse sequence
described in Chapter 8 consisting of nine π-pulses and occupying $2.75\tau_r$ has been
used (where τ_r is the rotation period of the sample).

For both QPASS and QTOSS, the desired coherence pathway is:
$\mathbf{p} = \{0 \to -1 \to +1 \to -1 \to +1 \to -1 \to +1 \to -1 \to +1 \to -1\}$. Therefore, a
the conventional phase cycle (with every other pulse being cycled [80]) would
require a minimum of 1875 steps. Using a cogwheel phase cycle, the desired
pathway can be selected by only 19 steps. Results for QTOSS are presented in
Fig. 9.6. Experiments were performed at a spinning frequency of 1100 Hz and at a
static magnetic field of 7.05 T. In Fig. 9.6, *a*, the [27]Al spectrum shown was acquired
by applying a $\pi/2$-pulse (total number of scans was 1876). The spectra shown in
Fig. 9.6, *b* and *c*, were obtained using the QTOSS sequence, with conventional and
cogwheel phase cycling procedures, respectively. The number of transients was 1875

and 1881. In the case of quadrupolar nuclei, however, the signal-to-noise ratio usually is small, and the number of transients is often determined by the necessity to increase it rather than by the phase cycle.
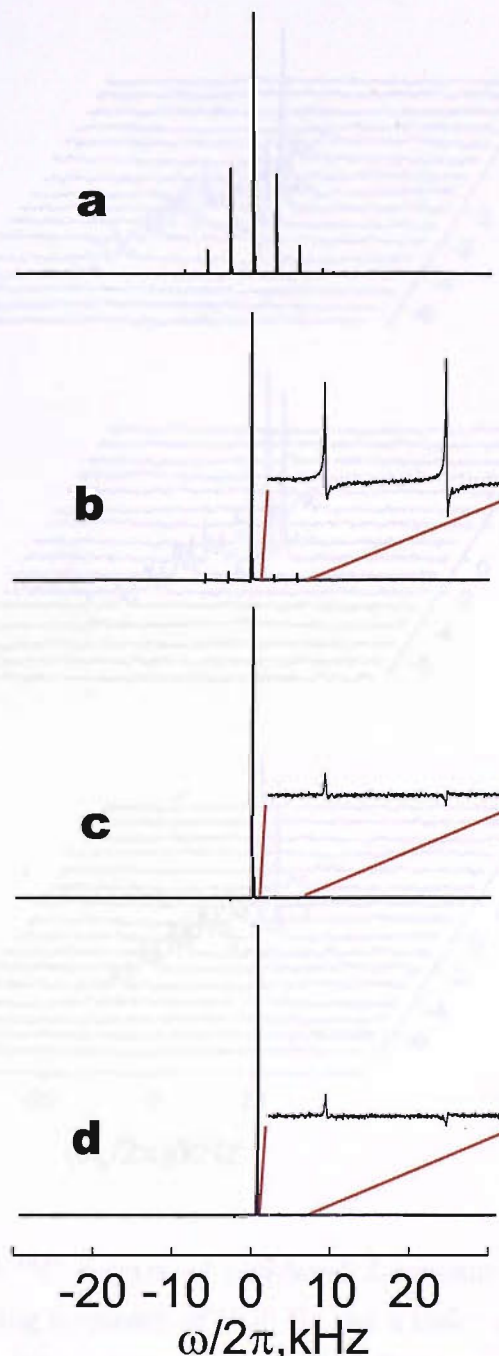
Figure 9.3: ^{13}C spectra of 1-^{13}C-Glycine (99%) at a spinning frequency of 2900 Hz. The static magnetic field was 7.05 T. a, simple CP MAS spectrum (76 transients in total); b, spectrum acquired using the TOSS-5 pulse sequence [76] with no phase cycle applied (76 transients); c, spectrum acquired using the TOSS-5 sequence with the conventional 75-step phase cycle (75 transients); d, spectrum acquired using the TOSS-5 sequence with the cogwheel 11-step phase cycle (sum of 77 transients = 7 repetitions of the 11-step phase cycle). All the spectra are plotted on the same vertical scale; in b, c and d, expanded regions of the spectra are presented.
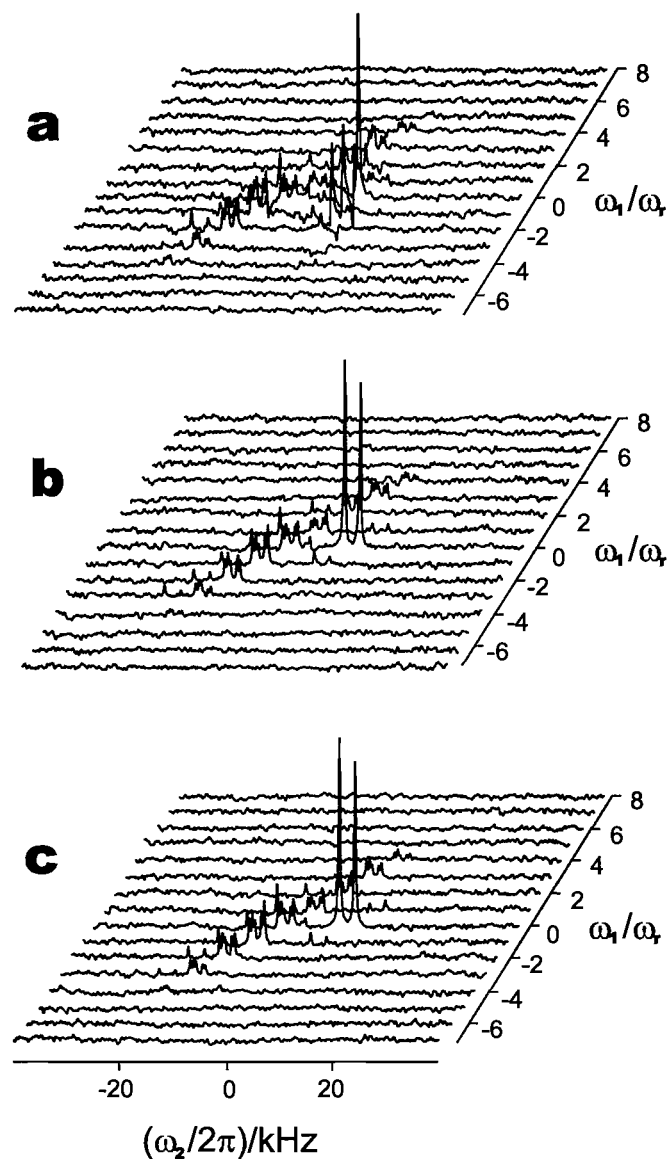
Figure 9.4: 2D PASS ^{13}C spectra of powdered L-tyrosine hydrochloride (natural abundance) at a spinning frequency of 1750 Hz and a static magnetic field of 7.05 T. a, spectrum acquired with no phase cycle applied (300 transients per Θ increment); b, spectrum acquired using the conventional 75-step phase cycle (300 transients per Θ increment, i.e. 4 repetitions of the phase cycle); c, spectrum obtained with the cogwheel 11-step phase cycle (297 transients per pitch Θ increment – 27 repetitions of the 11-step phase cycle). All spectra are plotted on the same vertical scale.
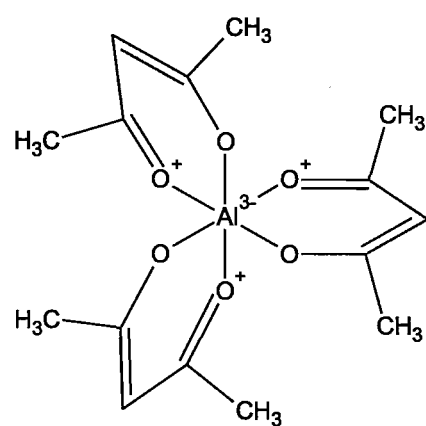
Figure 9.5: Structure of aluminium acetylacetonate a.k.a. aluminium 2,4-pentanedionate ($C_{15}H_{21}AlO_6$).
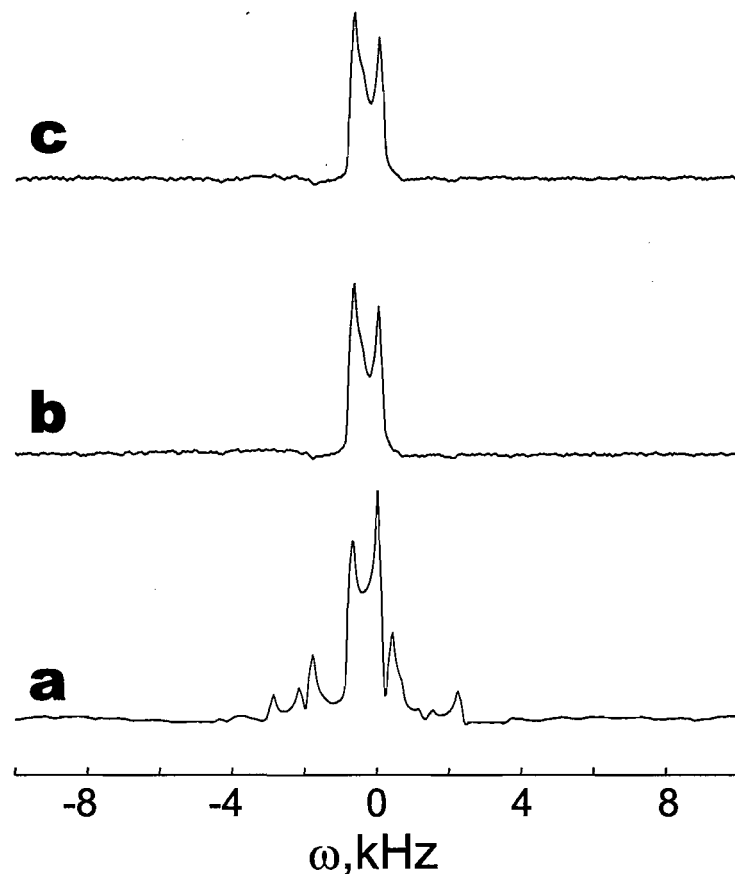
Figure 9.6: ^{27}Al-spectra of aluminium acetylacetonate. a shows spectrum obtained by applying a $\frac{\pi}{2}$-pulse directly followed by acquisition. b and c show spectra obtained by using QTOSS after the $\frac{\pi}{2}$-pulse, with conventional and cogwheel phase cycle, respectively. Spinning frequency was 1100 Hz and static magnetic field was 7.05 T.

Chapter 10

Summary

In this thesis, the following results are presented:

- a new phase cycling method, called multiplex phase cycling, is described. The acquired data can be reused for obtaining signals coming from different coherence pathways. This is done by applying different numerical complex factors to the stored NMR signals. In many cases, the multiplex phase cycling can provide significant saving of experimental time. Situations exist when it is problematic to select desired coherence pathways using conventional phase cycling methods but easy using the multiplex method.

- an improvement to the TOSS and PASS sequences is proposed. Taking the finite π-pulse duration into account in the TOSS and PASS equations leads to a shift in the pulse positions. Experimental TOSS spectra are shown where the sequence with shifted π-pulses demonstrates a better performance compared to the original one,

- application of the cogwheel phase cycling method is demonstrated for sideband suppression and separation sequences, both for spin-$\frac{1}{2}$ and quadrupolar nuclei.

- a new QTOSS pulse sequence for sideband suppression in the spectra of half-integer quadrupolar nuclei is proposed and experimental results are shown. This sequence of five π-pulses occupies 2.75 rotor periods. Because the time intervals between the π-pulses in this sequence is larger than in

previously described QTOSS sequences, it can be used at higher rotation frequencies.

Appendix A

Pulse Program for TOSS Accounting for Pulse Duration

Below, a part of a pulse program for the symmetrical TOSS-5 sequence [76], that is compensated for finite π-pulse duration, is presented. Approximate solutions of the TOSS equations were used for adjusting the π-pulse positions.

In the pulse program, apart from the standard notations used in the *Spinsight* pulse programs – $pw180X$ for the π-pulse duration on the ^{31}P channel, tMX for the mixing time and ad for the acquisition delay – the following notations are used: $e1$ and $e2$ stand for the ε_1 and ε_2 parameters, δ_θ for the π-pulse duration expressed in fractions of a rotor period (denoted as TM), and $TMa, TM2, TM3, TM4, TM5, TM6$ correspond to the six free evolution periods.

```
62 TM = (1.0/(1000.0*speed));
63
64 delta_theta = (pw180X/TM/2.0)*2.0*Pi;
65 e1 = 0.0404*delta_theta*delta_theta;
66 e2 = 0.0211*delta_theta*delta_theta;
67
68 TMa = (((0.2029 - e1) * TM) - (pw180X/2.0) - tMX);
69 TM2 = (((((0.32578 - e2) - (0.2029 - e1))* TM) - pw180X - tMX);
70 TM3 = (((0.5 - (0.32578 - e2)) * TM) - pw180X - tMX);
```

```
71 TM4 = (((0.5 - (0.32578 - e2)) * TM) - pw180X - tMX);
72 TM5 = ((((0.32578 - e2) - (0.2029 - e1))* TM) - pw180X - tMX);
73 TM6 = (((0.2029 - e1)* TM) - (pw180X/2.0) - ad);
```

Appendix B

SIMPSON Input File for Simulation of QTOSS Experiment

Below, a SIMPSON input file for simulation of the ^{27}Al QTOSS spectra of aluminium acetylacetonate is shown. The parameters of the quadrupolar interaction used here were taken from [79].

```
spinsys {
  channels 27Al
  nuclei 27Al
  quadrupole 1 2 3.0e6 0.0 0 0 0
}

par {
  spin_rate        1100
  gamma_angles     10
  sw               20000
  crystal_file     zcw232
  np               2048
  start_operator   I1z
  detect_operator  I1c
  method           direct
```

```
    proton_frequency 300.0e6
    verbose           1101
}

proc pulseq {} {
  global par

  maxdt .5

  set tdwell [expr 1.0e6/$par(sw)]



set theta1  [expr 0.0869e6/$par(spin_rate) - 11.0]
set theta2  [expr 0.2850e6/$par(spin_rate) - 22.0]
set theta3  [expr 0.2678e6/$par(spin_rate) - 22.0]
set theta4  [expr 0.1453e6/$par(spin_rate) - 22.0]
set theta5  [expr 0.6682e6/$par(spin_rate) - 22.0]
set theta6  [expr 0.1235e6/$par(spin_rate) - 22.0]
set theta7  [expr 0.2530e6/$par(spin_rate) - 22.0]
set theta8  [expr 0.3397e6/$par(spin_rate) - 22.0]
set theta9  [expr 0.0990e6/$par(spin_rate) - 22.0]
set theta10 [expr 0.4816e6/$par(spin_rate) - 11.0]

pulseid 5 50000 0

delay $theta1
pulse 22.0 7575.7576 0

delay $theta2
pulse 22.0 7575.7576 0

delay $theta3
pulse 22.0 7575.7576 0
```

```
delay $theta4
pulse 22.0 7575.7576 0

delay $theta5
pulse 22.0 7575.7576 0

delay $theta6
pulse 22.0 7575.7576 0

delay $theta7
pulse 22.0 7575.7576 0

delay $theta8
pulse 22.0 7575.7576 0

delay $theta9
pulse 22.0 7575.7576 0

delay $theta10

  acq
  for {set i 1} {$i < $par(np)} {incr i} {
  delay $tdwell
  acq
    }

}


proc main {} {
  global par tsw
```

```
    set f [fsimpson]
    fsave $f $par(name).fid
    fzerofill $f 4096
    faddlb $f 100 0
    fft $f
    fsave $f $par(name).spe
    funload $f
}
```

Bibliography

[1] E. M. Purcell, H. C. Torrey, and R. V. Pound. Resonance Absorption by Nuclear Magnetic Moments in a Solid. *Physical Review*, 69:37–38, January 1946.

[2] F. Bloch, W. W. Hansen, and M. Packard. Nuclear Induction. *Physical Review*, 69:127–127, February 1946.

[3] R. R. Ernst. Nuclear-Magnetic-Resonance Fourier-Transform Spectroscopy (Nobel Lecture). *Angew. Chem. Int. Edit.*, 31:805–823, 1992.

[4] A. Bax and N. Tjandra. High-Resolution Heteronuclear NMR of Human Ubiquitin in an Aqueous Liquid Crystalline Medium. *J. Biomol. NMR*, 10:289–292, 1997.

[5] N. Müller and P. K. Madhu. Current Developments in Solid State NMR Spectroscopy. *Monatshefte für Chemie, Int. Ed.*, 133:V–VI, 2002.

[6] I. J. Lowe. Free Induction Decay of Rotating Solids. *Phys. Rev. Lett.*, 2:285–287, 1959.

[7] E. R. Andrew, A. Bradbury, and R. G. Eades. Removal of Dipolar Broadening of Nuclear Magnetic Resonance Spectra of Solids by Speciment Rotation. *Nature*, 183:1802–1803, 1959.

[8] G. Bodenhausen, H. Kogler, and R. R. Ernst. Selection of Coherence-Transfer Pathways in NMR Pulse Experiments. *J. Magn. Res.*, 58:370–388, 1984.

[9] A. D. Bain. Coherence Levels and Coherence Pathways in NMR – a Simple Way to Disign Phase Cycling Procedures. *J. Magn. Res.*, 56:418–427, 1984.

[10] M. Bak, J. T. Rasmussen, and N. C. Nielsen. SIMPSON: a General Simulation Program for Solid-State NMR Spectroscopy. *J. Magn. Res.*, 147:296–330, 2000.

[11] M. H. Levitt. *Spin Dynamics. Basics of Nuclear Magnetic Resonance.* Wiley, Chichester, 2001.

[12] M. Ernst. *Phase Sensitive Detection in 1D- and 2D-NMR. NMR Instrumentation Seminar.* Berkeley, March 17, 1995.

[13] D. Marion and K. Wüthrich. Application of Phase Sensitive Two-dimentional Correlation Spectroscopy (COSY) for Measurements of ^{1}H-^{1}H Spin-Spin Coupling-Constants in Proteins. *Biochem. Biophys. Res. Co.*, 113:967–974, 1983.

[14] A. G. Redfield and R. K. Gupta. Fourier-Transform NMR Spectrometer for Use with H_2O Solutions. *J. Chem. Phys.*, 54:1418–1419, 1971.

[15] D. J. States, R. A. Haberkorn, and D. J. Ruben. A Two-dimensional Nuclear Overhauser Experiment with Pure Absorption Phase in 4 quadrants. *J. Magn. Res.*, 48:286–292, 1982.

[16] D. Marion, M. Ikura, R. Tschudin, and A. Bax. Improved Solvent Suppression in One-Dimensional and Two-Dimensional NMR Spectra By Convolution of Time-Domain data. *J. Magn. Res.*, 85:393–399, 1989.

[17] M. J. Duer. *Solid State NMR Spectroscopy: Principles and Applications.* Blackwell Science, Oxford, 2002.

[18] J. J. Sakurai and S. F. Tuan. *Modern Quantum Mechanics.* Benjamin/Cummings, Menlo Park, California, 1985.

[19] S. A. Smith, W. E. Palke, and J. T. Gerig. The Hamiltonians of NMR, Part I. *Conc. Magn. Reson.*, 4:107–144, 1992.

[20] S. A. Smith, W. E. Palke, and J. T. Gerig. The Hamiltonians of NMR, Part II. *Conc. Magn. Reson.*, 4:181–204, 1992.

[21] M. E. Rose. *Elementary Theory of Angular Momentum.* Wiley, New York, 1957.

[22] M. H. Levitt, D. P. Raleigh, F. Creuzet, and R. G. Griffin. Theory and Simulations of Homonuclear Spin Pair Systems in Rotating Solids. *J. Chem. Phys.*, 92:6347–6364, 1990.

[23] K. Schmidt-Rohr and W. Spiess. *Multidimentional Solid-State NMR and Polymers*. Academic Press, San Diego, 1994.

[24] D. A. Varshalovich, A. N. Moskalev, and V. K. Khersonskii. *Quantum Theory of Angular Momentum*. World Scientific, Singapore, 1988.

[25] M. Mehring. *Principles of High Resolution NMR in Solids*. Springer-Verlag, Berlin, 1983.

[26] J. Cavanagh, W. Fairbrother, A. G. Palmer, and N. Skelton. *Protein NMR Spectroscopy: Principles and Practice*. Academic Press, San Diego, 1995.

[27] K. Schmidt-Rohr, J. Clauss, and H. W. Spiess. Heterogeneous Polymer Materials by 2-Dimensional Wideline-Separation NMR-spectroscopy. *Macromolecules*, 25:3273–3277, 1992.

[28] L. Duma, W. C. Lai, M. Carravetta, L. Emsley, S. P. Brown, and M. H. Levitt. Principles of Spin-Echo Modulation by J-couplings in Magic-Angle-Spinning Solid-State NMR. *Chem. Phys. Chem.*, 5:815–833, 2004.

[29] S. P. Brown, M. Perez-Torralba, D. Sanz, R. M. Claramunt, and L. Emsley. The Direct Detection of a Hydrogen Bond in the Solid State by NMR Through the Observation of a Hydrogen-Bond Mediated ^{15}N-^{15}N J Coupling. *J. Am. Chem. Soc.*, 124:1152–1153, 2002.

[30] A. G. Vega. Quadrupolar nuclei in solids. In D. M. Grant and R. K. Harris, editors, *Encyclopedia of Nuclear Magnetic Resonance, Vol.6*, pages 3869–3889. Wiley, Chichester, 1996.

[31] P. P. Man. Quadrupole Coupling in Nuclear Magnetic Resonance, General. In R. A. Meyers, editor, *Encyclopedia of Analytical Chemistry*, pages 12224–12265. Wiley & Sons,, 2000.

[32] T. M. Clark and P. J. Grandinetti. Dependence of Bridging Oxygen O-17 Quadrupolar Coupling Parameters on Si-O Distance and Si-O-Si Angle. *J. Phys. - Condens. Mat.*, 15:S2387–S2395, 2003.

[33] A. Goldbourt and P. K. Madhu. Multiple-Quantum Magic-Angle Spinning: High-Resolution Solid State NMR Spectroscopy of Half-Integer Quadrupolar Nuclei. *Monatshefte für Chemie, Int. Ed.*, 133:1497–1534, 2002.

[34] A. Samoson, E. Lippmaa, and A. Pines. High-Resolution Solid-State NMR Averaging of 2nd-order Effects by Means of a Double-Rotor. *Mol. Phys.*, 65:1013–1018, 1988.

[35] A. Llor and J. Virlet. Towards High-Resolution NMR of More Nuclei in Solids – Sample Spinning with Time-Dependent Spinner Axis Angle. *Chem. Phys. Lett.*, 152:248–253, 1988.

[36] B. F. Chmelka, K. T. Müller, A. Pines, J. Stebbins, Y. Wu, and J. W. Zwanziger. O-17 NMR in Solids by Dynamic-Angle Spinning and Double Rotation. *Nature*, 339:42–44, 1989.

[37] A. Pines, M. G. Gibby, and J. S. Waugh. Proton-Enhanced NMR of Dilute Spins in Solids. *J. Chem. Phys.*, 59:569–590, 1973.

[38] S. R. Hartmann and E. L. Hahn. Nuclear Double Resonance in the Rotating Frame. *Phys. Rev.*, 128:2042–2053, 1962.

[39] O. B. Peersen, X. Wu, I. Kustanovich, and S. O. Smith. How Do Serine Proteases Really Work? *J. Magn. Res., Ser. A*, 104:334–337, 1993.

[40] G. Metz, X. Wu, , and S. O. Smith. Ramped-Amplitude Cross Polarization in Magic-Angle-Spinning NMR. *J. Magn. Res., Ser. A*, 110:219–227, 1994.

[41] S. Hediger, B. H. Meier, N. D. Kurur, G. Bodenhausen, and R. R. Ernst. NMR Cross Polarization by Adiabatic Passage Through the Hartmann-Hahn Condition (APHH). *Chem. Phys. Lett.*, 223:283–288, 1994.

[42] A. E. Bennett, C. M. Rienstra, M. Auger, K. V. Lakshmi, and R. G. Griffin. Heteronuclear Decoupling in Rotating Solids. *J. Chem. Phys.*, 103:6951–6958, 1995.

[43] P. Tekely, P. Palmas, and D. Canet. Effect of Proton Spin Exchange on the Residual ^{13}C MAS NMR Linewidths. Phase-Modulated Irradiation for Efficient Heteronuclear Decoupling in Rapidly Rotating Solids. *J. Magn. Res., Ser. A,* 107:129–133, 1994.

[44] A. Detken, E. H. Hardy, M. Ernst, and B .H. Meier. Simple and Efficient Decoupling in Magic-Angle Spinning Solid-State NMR: the XiX Scheme. *Chem. Phys. Lett.,* 356:298–304, 2002.

[45] N. C. Nielsen, F. Creuzet, R. G. Griffin, and M. H. Levitt. Enhanced Double-Quantum Nuclear Magnetic Resonance in Spinning Solids at Rotational Resonance. *J. Chem. Phys.,* 96:5668–5677, 1991.

[46] N. C. Nielsen, H. Bildsøe, H. J. Jakobsen, and M. H. Levitt. Double-Quantum Homonuclear Rotary Resonance: Efficient Dipolar Recovery in Magic-Angle Spinning Nuclear magnetic resonance. *J. Chem. Phys.,* 101:1805–1812, 1994.

[47] T. Gullion and J. Schaefer. Rotational-Echo Double-Resonance NMR. *J. Magn. Res.,* 81:196–200, 1989.

[48] A. E. Bennett, J. H. Ok, and R. G. Griffin. Chemical Shift Correlation Spectroscopy in Rotating Solids: Radio Frequency-Driven Dipolar Recoupling and Longitudinal Exchange. *J. Chem. Phys.,* 96:8624–8627, 1992.

[49] M. Carravetta, M. Eden, X. Zhao, A. Brinkmann, and M. H. Levitt. Symmetry Principles for the Design of Radiofrequency Pulse Sequences in the Nuclear Magnetic Resonance of Rotating Solids. *Chem. Phys. Lett.,* 321:205–215, 2000.

[50] M. Eden and M. H. Levitt. Pulse Sequence Symmetries in the NMR of Spinning Solids. Application to Heteronuclear Decoupling. *J. Chem. Phys.,* 111:1511–1519, 2000.

[51] A. Brinkmann, M. Eden, and M. H. Levitt. Synchronous Helical Pulse Sequences in Magic-angle Spinning Nuclear Magnetic Resonance: Double Quantum Recoupling of Multiple-Spin Systems. *J. Chem. Phys.,* 112:8539–8554, 2000.

[52] Y. K. Lee, N. D. Kurur, M. Helme, O. G. Johannessen, N. C. Nielsen, and M. H. Levitt. Efficient Dipolar Recoupling in the NMR of Rotating Solids. A Sevenfold

Symmetric Radiofrequency Pulse Sequence. *Chem. Phys. Lett.*, 242:304–309, 1995.

[53] M. H. Levitt, P. K. Madhu, and C. E. Hughes. Cogwheel Phase Cycling. *J. Magn. Res.*, 155:300–306, 2002.

[54] J. Keeler, R. T. Clowes, A. L. Davis, and E. D. Laue. Pulsed-field gradients: Theory and practice. In *Methods in Enzymology, Vol.239*, pages 145–207. Academic Press, San Diego, 1994.

[55] L. Mitschang, D. Grindrod H. Ponstingl, and H. Oschkinat. Geometrical Representation of Coherence Transfer Selection by Pulsed-Field Gradients in High-Resolution Nuclear Magnetic Resonance. *J. Chem. Phys.*, 102:3089–3098, 1995.

[56] F. S. Debouregas and J. S. Waugh. ANTIOPE, a Program for Computer Experiments on Spin Dynamics. *J. Magn. Res.*, 96:280–289, 1992.

[57] S. A. Smith, T. O. Levante, B. H. Meier, and R. R. Ernst. Computer Simulations in Magnetic Resonance – an Object-Oriented Programming Approach. *J. Magn. Res., Ser. A*, 106:75–105, 1994.

[58] J. Skibsted, N. C. Nielsen, H. Bildsøe, and H. J. Jakobsen. Satellite Transitions in MAS NMR Spectra of Quadrupolar Nuclei. *J. Magn. Res.*, 106:88–117, 1991.

[59] H. Bildsøe. *STARS User Guide. Spectrum Analysis in Rotating Solids.* Varian Associates Inc., Palo Alto, 1996.

[60] Zh. Gan and H.-T. Kwak. Enhancing MQMAS Sensitivity Using Signals from Multiple Coherence Transfer Pathways. *J. Magn. Res.*, 168:346–351, 2004.

[61] W. T. Dixon. Spinning-sideband-free and spinning-sideband-only NMR spectra in spinning samples. *J. Chem. Phys.*, 77:1800–1809, 1982.

[62] J. Hong and G. S. Harbison. Magic-Angle Spinning Sideband Elimination by Temporary Interruption of the Chemical Shift. *J. Magn. Res., Ser. A*, 105:128–136, 1993.

[63] T. J. Bonagamba and H. Panepucci. Variable-Low-Speed Magic-Angle-Spinning – a Simple Method to Suppress Spinning Side-Bands. *J. Magn. Res., Ser. A*, 103:103–104, 1993.

[64] T. J. Bonagamba, H. Panepucci, and E. A. Vidoto. Apparatus and Method for Side-Band Suppression by Variable Low-Speed Magic-Angle-Spinning Nuclear Magnetic Resonance Experiments. *Rev. Sci. Instrum.*, 66:3994–3995, 1995.

[65] P. K. Madhu, R. Pratima, and A. Kumar. Suppression of Sidebands by Variable Speed Magic-Angle Sample Spinning in Solid State NMR. *Chem. Phys. Lett.*, 256:87–89, 1996.

[66] O. N. Antzutkin, S. C. Shekar, and M. H. Levitt. 2-Dimensional Side-Band Separation in Magic-Angle-Spinning NMR. *J. Magn. Res., Ser. A*, 115:7–19, 1995.

[67] D. W. Alderman, G. McGeorge, J. Z. Hu, R. J. Pugmire, and D. M. Grant. A Sensitive, High Resolution Magic Angle Turning Experiment for Measuring Chemical Shift Tensor Principal Values. *Mol. Phys.*, 95:1113–1126, 1998.

[68] D. M. Grant. Five π Pulse Magic-Angle Turning Spectra of Solids. In D. M. Grant and R. K. Harris, editors, *Encyclopedia of Nuclear Magnetic Resonance, Vol. 9, Advances in NMR*, pages 73–90. Wiley, 2002.

[69] A. C. Kolbert and R. G. Griffin. Two-dimensional Resolution of Isotropic and Anisotropic Chemical Shifts in Magic Angle Spinning NMR. *Chem. Phys. Lett.*, 166:87–91, 1990.

[70] W. T. Dixon. Pulse Sequence for Spinning Sideband Suppression of Quadrupolar Nuclei. *J. Magn. Res.*, 164:332–333, 1985.

[71] S. J. Lang. Analytical Expressions for TOSS Sequences. *J. Magn. Res., Ser. A*, 104:345–346, 1993.

[72] D. P. Raleigh, E. T. Olejniczak, and R. G. Griffin. Multiple-Pulse NMR in Inhomogeneously Broadened Rotating Solids: Theory of Sideband Suppression Experiments. *J. Chem. Phys.*, 89:1333–1350, 1988.

[73] N. C. Nielsen, H. Bildsøe, and H. J. Jakobsen. TOSS in High-Speed MAS NMR. *J. Magn. Res.*, 80:149, 1988.

[74] O. N. Antzutkin. Sideband Manipulation in Magic-Angle-Spinning Nuclear Magnetic Resonance. *Prog. in NMR*, 35:203–266, 1999.

[75] N. Ivchenko and M. H. Levitt. TOSS and PASS Pulse Sequences Compensated for Finite π-pulse Duration. *In draft*, 2004.

[76] Z. Song, O. N. Antzutkin, X. Feng, and M. H. Levitt. Side-Band Suppression in Magic-Angle-Spinning NMR by a Sequence of 5 pi Pulses. *Solid State Nucl. Magn. Reson.*, 2:143–146, 1993.

[77] O. N. Antzutkin, Z. Song, X. Feng, and M. H. Levitt. Suppression of Side-Band in Magic-Angle-Spinning Nuclear-Magnetic-Resonance – General Principles and Analytical Solutions. *J. Chem. Phys.*, 100:130–140, 1994.

[78] D. Massiot, V. Montouillout, F. Fayon, P. Florian, and C. Bessada. Order-Resolved Sideband Separation in Magic Angle Spinning NMR of Half Integer Quadrupolar Nuclei. *Chem. Phys. Lett.*, 272:295–300, 1997.

[79] Y. Millot and P. P. Man. Procedures for Labeling the High-Resolution Axis of Two-dimensional MQ-MAS NMR Spectra of Half-Integer Quadrupole Spins. *Solid State Nucl. Magn. Reson.*, 21:21–43, 2002.

[80] N. Ivchenko, C. E. Hughes, and M. H. Levitt. Application of Cogwheel Phase Cycling to Sideband Manipulation Experiments in Solid-State NMR. *J. Magn. Res.*, 164:286–293, 2003.